Earthquake Risk Assessment of Reinforced Concrete Bridges in Washington State Using Pushover Analysis

Abigail B. Christman

A thesis
submitted in partial fulfillment of the
requirements for the degree of

Master of Science in Civil Engineering

University of Washington

2017

Committee:

Paolo Calvi

Jeffrey Berman

Marc Eberhard

Program Authorized to Offer Degree:

Civil and Environmental Engineering

University of Washington

Abstract

Earthquake Risk Assessment of Reinforced Concrete Bridges in Washington State Using Pushover Analysis

Abigail B. Christman

Chair of the Supervisory Committee:

Dr. Paolo Calvi

Civil and Environmental Engineering

The average age of reinforced concrete bridges in the state of Washington is 48 years, encompassing more than 100 years of design and construction techniques, which reflect evolving views on seismic risk and mitigation. As such, there is great uncertainty as to the actual seismic resistance of existing bridges. Having a simple and accurate process for assessing the seismic vulnerability of a bridge can help identify vulnerable design details and address them, either through retrofit or replacement.

Using pushover analysis to determine the seismic capacity of structures can give an idea of the overall vulnerability of the structure while decreasing the computational power needed to perform analyses as compared to nonlinear time history (NLTH) analysis. Using the finite element program RUAUMOKO-2D, models of existing WSDOT bridges were created and pushover analyses were run. By defining damage states of interest and determining the associated displacement profiles, peak ground accelerations (PGAs) of seismic events were then correlated to the damage states. By combining fragility curves encompassing the probabilistic distribution of the PGA at which a damage state might occur with site hazard

risks, Risk Indices were calculated for all bridges considered. The bridges were ranked in order to contextualize the Risk Index values. The results of the assessment process were then verified by comparing them to the results of NLTH analysis.

TABLE OF CONTENTS

Page

LIST OF FIGURES

ACKNOWLEDGMENTS

I want to thank Dr. Paolo Calvi for his guidance and advice in completing this project.

I would also like to thank my friends for their willingness to share their brilliance with me (in small words when necessary).

DEDICATION

This thesis is dedicated to my family. You may not always understand my work, but your support and encouragement were instrumental in completing it.

And to all the people who post pictures of dogs on the internet. You're the real heroes.

Chapter 1

INTRODUCTION

1.1 Motivation

Evolving understanding of both the seismic risk faced in the Puget Sound region and the response of the built environment to earthquakes has highlighted the need to determine the seismic vulnerability of existing structures. To that end, Washington State Department of Transportation (WSDOT) has undertaken a program to analyze, prioritize, and retrofit or replace, as necessary, its bridge stock [60].

There are a number of ways of assessing the structural response of a bridge. The most simplistic methods rely on a number of simplifications and assumptions, and therefore may be somewhat unrealistic. More complex methods yield more realistic results, but they take a nontrivial amount of skill to conduct, and are often computationally intensive [22]. The ability to perform a simple analysis that yields realistic results is key to simplifying the process of analyzing bridges for seismic vulnerability.

Traditionally, seismic design has dealt with a single performance objective or loading target – the design earthquake. However, it can also be instructive to predict behavior of a bridge under earthquakes that are not the design earthquake. By identifying specific Damage States (DSs) of interest for a particular structure and determining the intensity of ground shaking associated with the attainment of those DSs, expectations for performance can be more comprehensively defined. This philosophy can be applied to both design of new construction

and assessment of existing structures. Additionally, identifying not only the capacity of a structure but also how that capacity interacts with the hazards present at the site can further illuminate the need for retrofit or replacement.

1.2 Response

In order to make analysis of the seismic vulnerability of existing structures as straightforward as possible, an analysis method has been put forward by Cardone et al ([14], [15], [16]) to allow for computationally efficient nonlinear static analysis of bridge models, which is meant to predict, with high accuracy, the dynamic response of the structure.

This method involves identifying structural displacements associated with DSs of interest, building a straightforward bridge model, performing a pushover analysis on the model, and using the forces and displacements at attainment of the DSs to predict the Peak Ground Accelerations (PGAs) at which the DSs will be reached. Fragility curves, which represent the probabilistic distribution of the actual attainment of the DSs based on the single PGA value calculated, can then be constructed. Finally, the fragility curves can be combined with the hazard curve describing the seismic risk at the site in order to calculate a Risk Index that can quantify the vulnerability, and be used to rank bridges against one another in order to quantify prioritization of vulnerable structures.

The goal of this project is to explore and verify Cardone's analysis procedure for motion in the transverse direction, using extremely simple numerical models. Ultimately it is anticipated that this will lead to the development of a software package that will be able to implement this analysis method. This software could be utilized by WSDOT and other DOTs to move forward with prioritization efforts efficiently and logically.

1.3 Layout

The following chapters make up this report:

Chapter 2: Background Chapter 2 examines the evolving understanding of seismic hazard faced in the Puget Sound region, typical damage suffered by bridges during earthquakes, widely used seismic analysis techniques, and describes the approach taken to analyze the seismic vulnerability of RC structures in this project.

Chapter 3: Modeling and Sample Selection Chapter 3 gives an overview of the element types used to build the structural models, outlines the process used to select study bridges, and describes the bridges chosen for study.

Chapter 4: Analysis Methodology Chapter 4 outlines the determination of DSs for different element types, construction of equivalent linear SDOF systems, the selection of ground motions for use in NLTH verification, creation of damped spectra, error calculation, and the calculations required to create the fragility curves and Risk Index.

Chapter 5: Results Chapter 5 presents the results of the analysis of the study bridges. The accuracy of predictions, as well as fragility curves and Risk Indices are laid out for each bridge. Vulnerability rankings are given, in order to contextualize the results of the individual bridges.

Chapter 6: Conclusion Chapter 6 presents an overview of the accuracy of the assessment method, explores limitations of the work, and outlines future work for this project.

Chapter 2

BACKGROUND

2.1 Seismic Hazard

2.1.1 Geological Background

Earthquakes result from the shifting of the Earth's crust. Generally, they occur at or near plate boundaries, as is the case on the West Coast of the United States, though intraplate fault zones such as the New Madrid fault in southeastern Missouri can also produce significant shaking [52]. No predictions can be made about the exact location, time, or magnitude of future earthquakes, but by studying fault geometry and soil deposits, geologists can estimate approximate frequency of their occurance [6], as well as estimate the maximum earthquake possible in a given location [58].

Techtonic plate boundaries fall into three broad categories, distinguished by how the plates move relative to each other [57].

i. Divergent boundaries, at which plates are moving away from each other. The Mid-Atlantic Ridge is an example of a divergent boundary.

ii. Convergence boundaries, at which plates are moving towards each other. The Cascadia Subduction Zone is an example of a convergence boundary [59].

iii. Transform boundaries, at which plates primarily move parallel to each other. The San Andreas fault is an example of a transform boundary [49].

The US Geological Survey (USGS) monitors seismic activity across the United States and around the world as part of the Global Seismographic Network, a network of over 150 seismometers in 80 countries. Additionally, academic groups, such as the Pacific Northwest Seismic Network in Washington and Oregon, maintain denser regional networks of seismometers [24].

2.1.2 Puget Sound Seismic Hazard

Though the best-known fault in the United States is the San Andreas fault, California hardly has a monopoly on seismic activity. Washington State also has a complex earthquake history.

An intricate network of faults, shown in Figure 2.1, is responsible for this risk. Though damaging earthquakes occurred in 1949 ($M_w \approx 6.8$), 1965 ($M_w \approx 6.5$), and 2001 ($M_w \approx 6.8$) in western Washington, many existing faults were unknown to scientists until a few decades ago. Paleoseismology, the study of earthquakes prior to the written record [1], as well as the development of LiDAR technology, has been instrumental in identifying fault locations and prehistoric earthquakes, which could help scientists identify future hazards [26]. One fault identified in such a way is the Seattle fault, whose location directly beneath the city poses significant risk, with a capability of producing a $M_w \approx 7.0$ earthquake, despite its relative inactivity in the last 1000 years [37]. Another fault whose true capabilities were only identified in the last 30 years is the Cascadia Subduction Zone, which has produced seven strong ($M_w \approx 9.0$) earthquakes in the last 3,500 years, most recently around 1700 [7].

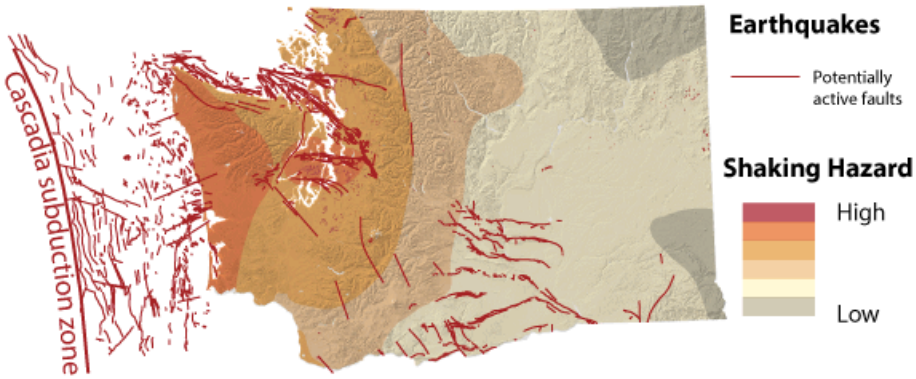

Figure 2.1: Map of Faults in Washington State, including qualitative indication of earthquake hazard [62].

In all, three general types of earthquakes pose a threat to the Puget Sound region, with different potentials for intensity of shaking and damage:

i. Megathrust events at the interface of the subducting Juan de Fuca plate and the overlying North American plate. Such events have the potential to release vast amounts of energy ($M_w \approx 9.0$) over huge distances ($\approx$1000 km).

ii. Events within the subducting Juan de Fuca plate. Such events are capable of producing earthquakes of magnitude $M_w \approx 7.0$ at approximate epicentral depth of 30-70 km. These events have a return period of 30-50 years, with the most recent event being the Nisqually earthquake of 2001 [42].

iii. Shallow crustal events in the North American plate. Such events are capable of producing earthquakes of magnitude $M_w \approx 7.5$ at epicentral depths of less than 35 km. Many faults capable of producing such events exist in the Puget Sound region, some of which are located directly beneath urban areas [41].

In comparison to other seismic regions, Washington is relatively quiet. A particularly striking description notes that similar seismic regions "produce major earthquakes occasionally and

minor ones all the time: magnitude 5.0, magnitude 4.0, magnitude why are the neighbors moving their sofa at midnight," and furthermore, "you can spend a lifetime in many parts of the Northwest – several, in fact, if you had them to spend – and not feel so much as a quiver" [50].

The relative lack of major seismic activity in the region has historically led to an attitude of complacency. This attitude has not only been held by general population but also within the engineering community, meaning that structures designed during previous design eras may have unknown or inadequate seismic capacity.

2.1.3 Bridges at Risk

In the aftermath of an earthquake, it is vital that emergency services can reach people in need. Beyond immediate emergency response, returning to pre-earthquake levels of travel and shipping in a timely fashion is key to economic recovery of stricken regions. Therefore, the road and bridge system in an at-risk region must be robust enough to sustain expected shaking with little to no damage [9]. Although the extent of damage seen can vary from earthquake to earthquake, and even bridge to bridge, patterns of types of damage emerge when performing reconnaissance. Types of damage generally fall into the following categories: substructure, superstructure, soil-structure interaction, and nonstructural. Brief descriptions of these types of damage follow, focusing on reinforced concrete bridge elements, as that was the focus of this project.

Superstructure Damage

Unseating Unseating occurs when bridge spans are displaced from their position atop the substructure. Some older bridges have very short bearing seat lengths, which makes unseating far more likely. Unseating can involve girders displacing from their bearings and coming to rest on the pier cap, or can result in the complete collapse of a span, both of which are demonstrated in Figure 2.2 [19].

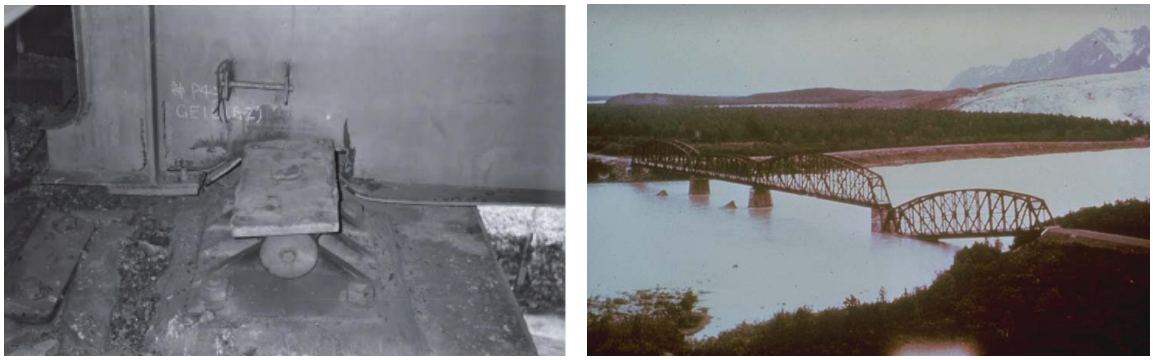

(a) (b)

Figure 2.2: Unseating failures (a) of Pier 42 of Route 3 from the 1995 Kobe earthquake [19], and (b) of the "Million Dollar Bridge" over the Copper River outside of Cordova, Alaska was unseated during the 1964 Alaskan Earthquake [54]

Expansion Joints Expansion joints are designed to allow for limited relative motion between superstructure segments due to temperature fluctuations, creep, shrinkage, and traffic-induced motion. However, earthquakes can cause sudden closing or opening of expansion joints, which may cause crushing or span discontinuities, respectively. Figure 2.3 illustrates excessive opening at an expansion joint. In extreme cases, opening at an expansion joint can result in unseating, as described above [10].

Figure 2.3: Differential movement between adjacent deck sections at an expansion joint led to a span discontinuity at pier 97 of the Hanshin Expressway in Japan after the 1995 Kobe Earthquake [55].

Substructure Damage

Piers As primary components of the gravity and lateral system of bridges, piers are subjected to intense forces during earthquakes. Damage to piers depends largely on bridge design. Short, stout piers are more susceptible to shear failure, as shown in Figure 2.4. Specific design details, such as insufficient reinforcement lap length or inadequate transverse reinforcement, can lead to premature failure. Figure 2.5 shows failure resulting from inadequate transverse reinforcement [36]. Even well confined, ductile columns might experience spalling of unconfined outer layers of concrete, such as in Figure 2.6 [10].

Figure 2.4: The flared piers of the Mission-Gothic underpass experienced shear failure during the 1994 Northridge Earthquake, likely after yielding of the longitudinal reinforcement reduced the pier's shear capacity [5].

Figure 2.5: Inadequate confinement in the I-10 La Cienega-Venice overpass led to buckling of longitudinal reinforcement and crushing to core concrete during the 1994 Northridge earthquake [18].

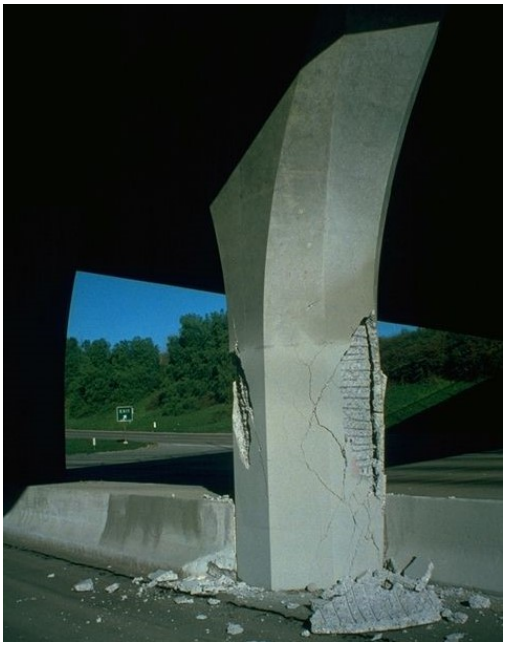

Figure 2.6: Unconfined concrete on the Ruffner Ave bridge spalled off during the 1994 Northridge earthquake [31].

Abutments Abutment behavior is determined not only by the design of the structural components, but also by the interaction with soil surrounding the abutment (see below). Elements of abutments may include bearings (see below), wing walls, back walls, and foundation elements. Abutments often include elements such as shear keys, which aid in transferring motion from the superstructure to foundation elements, and can act as structural fuses whose failure controls damage to other elements of the structure [35].

Bearings Bearings are designed to transfer forces and allow differential motion between superstructure and substructure elements [30]. There are a number of common types of bearings, and the types of damage that can be expected varies by type. Two types of bearings relevant to this project are elastomeric bearings and steel roller bearings. Failure of elastomeric bearings depends on their configuration and loading. Elastomeric bearings that are bolted to the bridge elements they connect go through material failure at high strains.

Elastomeric bearings that are not bolted may slide, as shown in Figure 2.7, or the edges of the elastomer may begin to pull away from the adjacent elements, making slippage easier. Damage at steel roller bearings include pull-out or shearing of anchor bolts and crushing of adjacent concrete. Failure of bearings can contribute to unseating of spans [10].

Figure 2.7: An unbolted elastomeric bearing supporting the Bridge Street bridge outside Christchurch experienced a sliding failure during the 2010 New Zealand earthquake [11].

Soil-Structure Interaction

Piers, Abutments, and Approach Spans Soil surrounding bridge elements can settle or liquefy if it is not competent or if shaking is particularly strong. The shifting of material around these elements can lead to excessive deformation in the structure itself [19]. Figure 2.8 illustrates the damage possible from lateral spreading around bridge foundations.

Figure 2.8: Lateral spreading around the foundations of a railroad bridge in Costa Rica during the 1991 Limon earthquake caused significant displacement of the structure [64].

Non-Structural Damage

Non-Structural Elements Nonstructural elements include railings, barriers, signage, and utility conduits. Damage to these elements does not affect the structural integrity of the bridge, but secondary damage or injury could occur as a result of their failure. Examples include impact damage from falling overhead signs, risk of electrocution of passersby by severed electrical wires, and damaged barriers failing to prevent roadway departures [10].

2.2 Mitigating Risk

2.2.1 Seismic Design Evolution

In many ways, the history of seismic design of bridges in the United States is the history of major earthquakes in California. The first mention of earthquake loading in a standard specification was in 1940, seven years after the Long Beach earthquake, when the California

State Highways Department[1] recommended that bridge designers should determine seismic demand, though gave no specific guidance. Until the 1970s, The Standard Specifications for State Highway Bridges, released periodically by the American Association of State Highway Officials (AASHO[2]), simply included the instruction to increase the allowable stress in structural elements by 25% when designing for earthquake and other loading in combination [56].

After the 1971 San Fernando earthquake, in which seven bridges suffered catastrophic damage and approximately 60 more suffered moderate to severe damage [44], seismic design philosophy underwent a drastic change in not only California, but throughout the United States. Caltrans immediately doubled the seismic demand required for new design, and began to develop more robust methods of determining demand.

In 1974, Caltrans used geologic information to create seismic risk maps to more accurately determine local demand requirements. The 1975 AASHTO interim specifications similarly incorporated a risk map to determine demand, expanding the map to cover the entire country. Caltrans and the Federal Highway Administration (FHWA) funded extensive research during this time, which culminated in the publication of the 1983 AASHTO Guide Specifications for Seismic Design of Highway Bridges. The Guide Specifications were incorporated into the 1989 Standard Specifications [56]. During the 1989 Loma Prieta and 1994 Northridge earthquakes, bridges designed after the changes to code performed fairly well, confirming the decision to update design standards [36]. In the ensuing years, updates have been made to the risk maps based on new information, ensuring that design reflects current understanding.

2.2.2 Retrofits

While new bridges, designed using specifications that consider current understanding of risk, have known seismic capacity, the seismic capacity of older bridges may need to be investi-

[1]Forerunner of the California Department of Transportation (Caltrans)

[2]Forerunner of the American Association of State Highway and Transportation Officials (AASHTO)

gated. In some cases, capacity may prove unsatisfactory for desired performance. In such cases, retrofitting or replacing the structure may be necessary. In seismically active areas, retrofit efforts can be seen as a race against time since the timing of the next earthquake is unknown, so upgrades must be made quickly and effectively.

Often, major retrofit efforts are undertaken by state Departments of Transportation (DOTs) in reaction to earthquakes, because vulnerable details are often revealed in such events. In California, moderate retrofitting efforts were undertaken after the San Fernando earthquake, but major effort was not expended until the Loma Prieta earthquake. Though retrofitted bridges largely performed as expected, dramatic failures such as the Cypress Viaduct prompted renewed interest in retrofitting efforts. The retrofitting program initiated after the Loma Prieta earthquake was not complete by the 1994 Northridge earthquake, but those structures that had already been retrofitted performed as expected [13].

In Washington State, retrofitting efforts began in 1991, though the impetus for beginning the process was not a damaging earthquake in the Puget Sound. The implementation of a seismic retrofit program by the WSDOT was in fact a proactive, rather than reactive, measure, after the national codification of the new seismic design standards introduced in the 1980s [8]. Bridges with design details known to be vulnerable were prioritized for retrofit in the early phases of work. In order to impose further order on the remaining bridges, WSDOT identified a network of so-called "Seismic Lifeline Routes" essential to recovery of the Puget Sound region in the event of a major earthquake, shown in Figure 2.9. Current retrofit efforts are concentrated on bridges on the Seismic Lifeline Routes, with 85 Lifeline bridges awaiting retrofit as of June 2015 [60].

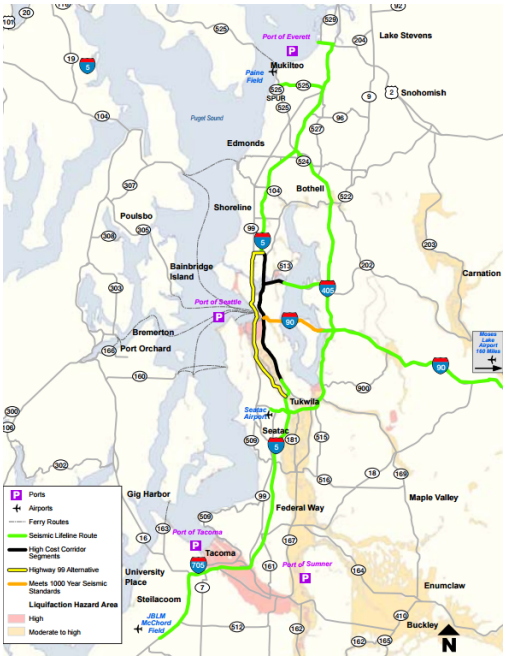

Figure 2.9: Map of Seismic Lifeline Routes as identified by WSDOT for retrofit priority [60].

2.2.3 Analysis

A number of methods exist to analyze structures for seismic soundness. Methods generally can be categorized as either linear elastic or nonlinear, and either static or dynamic. Additionally, either forces or the displacements in the structure can be used to assess performance. Current design and assessment methods use either target response spectra or ground motion time histories as the basis for structural demands.

Linear Static Common methods of linear static analysis and linear dynamic analysis (described below) are based on the equal displacement principle, which states that the ductility of a system after yielding is such that the displacement at failure is the same as that of a linear elastic system with a stiffness equal to the initial stiffness of the actual system. Therefore, the strength of the equivalent linear elastic system can be determined, and reduced by a reduction factor, R, in order to approximate the nonlinear system. This concept is illustrated in Figure 2.10.

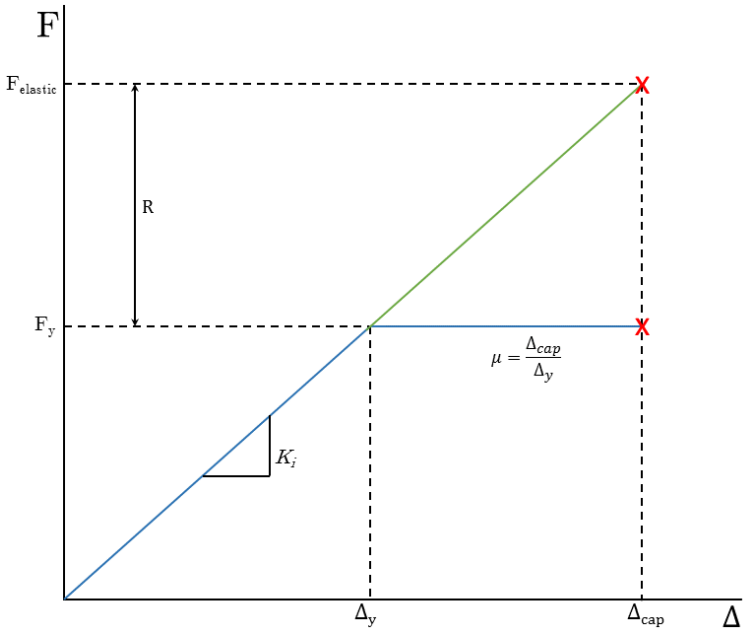

Figure 2.10: Illustration of the equal displacement principle, including definitions of ductility (μ) and reduction factor (R) (adapted from FHWA [22]).

Linear static analyses can focus on a single mode of vibration of the structure, or consider multiple modes. A target response spectrum is used to determine loading.

Linear static methods are relatively simple, but do have drawbacks. Due to the simplifying assumptions required, they work best for relatively typical bridges, with little skew, few spans, regular geometry, and few elements (such as elastomeric bearings) that could display highly nonlinear behavior. Additionally, the assumptions inherent in using R factors may yield somewhat unreliable results.

Linear Dynamic Linear dynamic analyses, like linear static analysis, rely on the equal displacement principle and the use of R factors. However, time histories are supplied as the load, which is more realistic than a statically applied load. Numerical methods are used to determine the structural response at each time step of the analysis.

Linear dynamic analyses are useful for a wider range of structures than linear static analysis.

However, due to the possibility of extreme loading during earthquakes, which can result in highly nonlinear behavior in an actual structure, linear dynamic analysis is still limited.

Nonlinear Static Nonlinear static (pushover) analysis incorporates a non-linear model, which allows for realistic response, but utilizes a quasi-static ramp load to assess capacity and a target response spectrum to determine demand. The use of a quasi-static ramp loading makes pushover analysis computationally efficient, and does not rely on curating a suite of ground motions for analysis.

Pushover analyses are primarily utilized for fairly typical structures, but can be used for non-typical structures as well. A drawback of this is the need to determine a realistic loading pattern on the structure in order to capture the effects of the multiple modes present in a structure. Antoniou and Pinho have proposed a method of determining loading patterns that is adaptive to the state of a structure at a given step, which shows promise in mitigating this drawback [4]. Dynamic effects are not captured by pushover analyses, which may limit the accuracy.

Nonlinear Dynamic Nonlinear dynamic (or nonlinear time history, NLTH) analysis is the most rigorous analysis method. Since both the model and loading are as realistic as possible, the responses calculated are considered the most accurate of the discussed analysis methods.

NLTH analyses can be performed on a wide range of structural geometries. However, models can be very sensitive to small changes, meaning that slight inaccuracies in assigning properties can render the results of analysis unreliable. In order for NLTH analyses to be representative, a suite of ground motions must be run, since earthquakes have wide-ranging and unpredictable characteristics. Additionally, complex bridge models can take large amounts of time and computational power to assess [22].

Force-Based and Displacement-Based Analysis For most of the history of codified design, analysis has been based on forces experienced by structural members. However, a more intuitive way to think about response to earthquake loading is displacement. The forces experienced by structural members are due to the displacement caused by shaking, rather than the force-based assumption of displacements being caused by applied forces. With the popularization of Performance Based Design, which emphasizes attaining a defined state of damage at a defined earthquake intensity, it has become clear that displacements are a more useful measure of performance [29].

2.3 This Project

2.3.1 Project Approach

This project seeks to use pushover analyses to predict the earthquake intensity - measured by PGA - at which different levels of damage are reached. The process, discussed in detail in Chapters 3 and 4, consists of five basic steps:

1. Create simple models using bridge properties extracted from design and as-built plans
2. Identify damage states (DSs) of interest and calculate the displacements at which damage states will be reached
3. Run a pushover and extract component responses at each DS
4. Determine the PGA required to reach each DS based on approximating an equivalent linear elastic SDOF system
5. Perform NLTH analyses using ground motions scaled to match the predicted PGA in order to assess the accuracy of the prediction

Once PGAs have been correlated to DSs, vulnerability of the bridge can be quantified. Quantifying risk consists of two steps:

1. Create fragility curves to determine the probabilistic distribution of PGAs that result in reaching the DSs

2. Take the convolution integral of the fragility curve with a location-specific hazard curve to quantify the vulnerability of the structure

2.3.2 Software Used

Sectional Analysis

Values for moment-curvature behavior of plastic hinge regions in columns was extracted from the MATLAB-based software package CUMBIA [38]. The material models used were the Mander model [32] for confined and unconfined concrete, and the Raynor model [48] for steel.

Running Pushover and NLTH Analyses

Models were built and analyzed using the nonlinear structural analysis program RUAUMOKO-2D [17]. Chapter 3 describes the built-in element types used to create the models.

Vulnerability Assessment

Microsoft Excel was utilized to determine the equivalent damped SDOF systems for each examined DS. The programming language Python was used in order to write a number of post-processing scripts. A Python script was created and implemented to determine the predicted PGA corresponding to the DS. Additional Python scripts were created and implemented to construct the DS fragility curves and calculate the corresponding risk indices from the convolution of the fragility and site hazard.

Chapter 3

MODELING AND SAMPLE SELECTION

3.1 Models

One of the goals in this project was to create simple, computationally efficient models for analysis. In order to do so, some assumptions were made. The most notable of these is the assumption of perfect rigidity of bridge decks. In most cases where decks are not extremely long and narrow or somehow geometrically complex, this is a reasonable assumption [46]. Study bridges were selected with this constraint in mind. An additional assumption made was one of perfect symmetry in the structure. This is a reasonable assumption given the geometries of the study bridges.

Damping was implemented in RUAUMOKO-2D with user-specified modal damping parameters [17]. Based on analysis of damping modelling by Smyrou, et al [51], it was determined that assigning a damping ratio of 5% to all but the first mode, with mode 1 having a lower damping ratio in order to limit damping after yielding, was appropriate. Based on lower limits to first mode damping implemented by Pennucci [43], a damping ratio of 1% was assigned to the first mode.

Elements required for models, as well as the properties for those elements, were determined based on information from design and as-built drawings, as well as contemporaneous design guides.

3.1.1 Piers

Piers were modeled as single one-component Giberson beam elements, which were imbued with characteristics reflecting the behavior of all columns making up the pier. The Giberson beam consists of a central elastic section, with rotational springs at one or both ends, as seen in Figure 3.1. This element type has been shown to be both accurate and computationally efficient to model concrete beam and column elements [34].

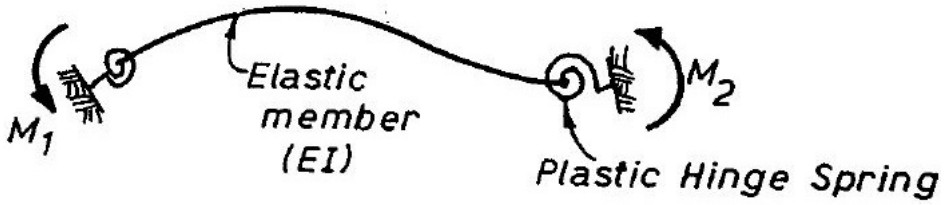

Figure 3.1: The one-component Giberson beam was used to model column elements [25].

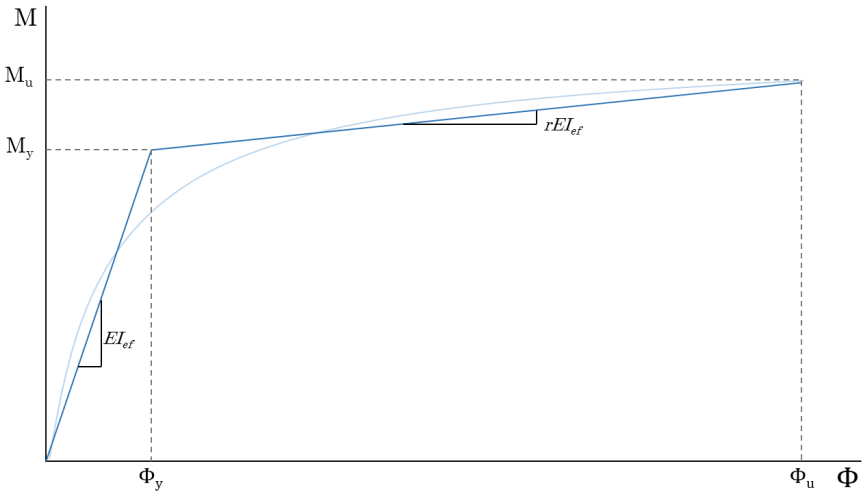

Figure 3.2: The monotonic behavior of the plastic hinge regions, shown in light blue, was approximated by CUMBIA as bilnear, whose behavior is demonstrated in dark blue.

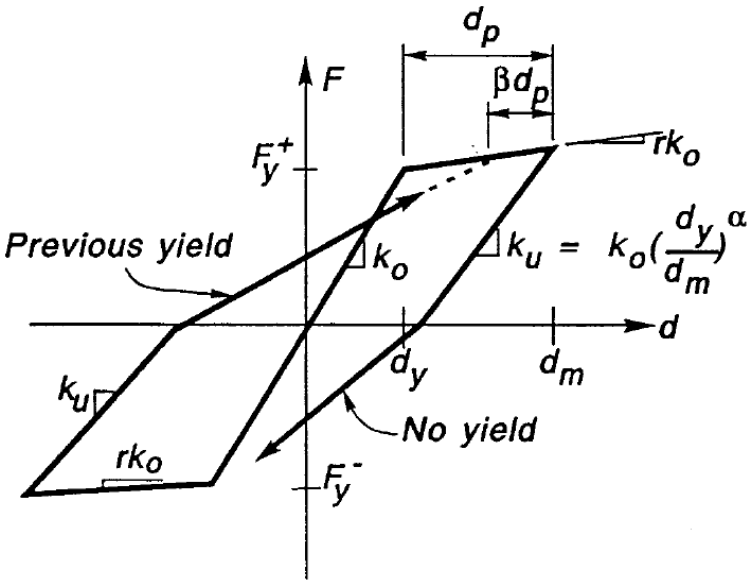

Figure 3.3: The modified Takeda curve as implemented in RUAUMOKO-2D [40] was used to model the cyclic behavior of plastic hinges [17].

The monotonic moment-curvature behavior of the rotational springs was determined using the Matlab-based sectional analysis tool CUMBIA and simplified a bilinear, as shown in Figure 3.2. Cyclic behavior of the rotational springs was modeled in RUAUMOKO-2D using the modified Takeda hysteresis curve, with parameters of $\alpha = 0.5$, $\beta = 0.0$, and a reloading stiffness of 1.0, with unloading as described by Emori and Schnobrich [20], as shown in Figure 3.3. Plastic hinge lengths, used to determine the position of the plastic hinge springs, were calculated using Equation 3.1 [15].

$$L_p = 0.08L + 0.022 f_y d_{bl} \tag{3.1}$$

where L is the clear height of the pier, f_y is the yield strength of longitudinal rebar, and d_{bl} is the diameter of a longitudinal bar.

Shear behavior of beam-column elements is not captured by RUAUMOKO-2D, so shear strength values were calculated independent of model creation. Total shear capacity of piers was found by summing the various components of shear strength in columns, as shown in Equation 3.2. Equations 3.3, 3.4, and 3.5 were used to calculate the strength contributions

from the concrete, reinforcing steel, and axial load respectively, for each pier. Steel jackets, which are retrofitted to columns in order to increase their shear capacity, were added to the columns of Bridge 2, and Equation 3.6 is used to calculated the added strength from the jackets [47].

$$V_n = V_c + V_s + V_p \quad (+V_{sj}) \tag{3.2}$$

$$V_c = kA_e\sqrt{f'_c} \quad \text{(psi)} \tag{3.3}$$

where k is a factor that depends on ductility of the column, A_e is the effective shear area, taken to be $0.8A_g$, and f'_c is the compressive strength of the concrete.

$$V_s = \frac{\pi}{2}\frac{A_{sh}f_{yh}D'}{s}\cot 30^\circ \quad \text{(circular cross sections)} \tag{3.4a}$$

$$V_s = \frac{A_{sh}f_{yh}D'}{s}\cot 30^\circ \quad \text{(rectangular cross sections)} \tag{3.4b}$$

where A_{sh}, f_{yh}, and s are the cross-sectional area, yield strength, and spacing of spiral or hoop reinforcement, respectively, and D' is the center-to-center transverse reinforcement diameter, as illustrated in Figure 3.4.

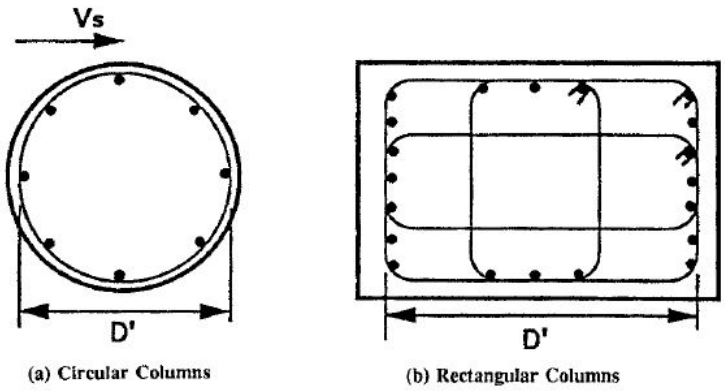

Figure 3.4: Illustration of center-to-center transverse reinforcement diameter, D' [47].

$$V_p = P\tan(\gamma) = P\frac{D-a}{H} \tag{3.5}$$

where Figure 3.5 illustrates the definitions of D, γ and H, and a is the depth of the compression region in the critical section.

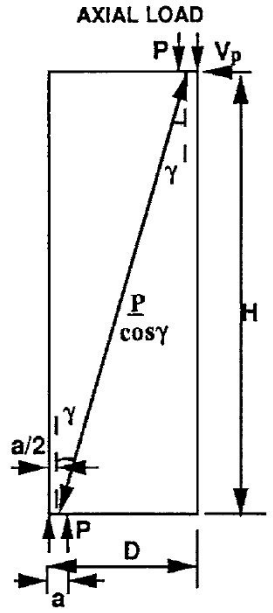

Figure 3.5: Illustration of dimensions used to determine the contribution of axial loading to the shear strength of columns [47].

$$V_{sj} = \frac{\pi}{2} \frac{t_j^2 f_{yj} (D_j - t_j)}{t_j} \cot 30^\circ \tag{3.6}$$

where

t_j = thickness of the steel jacket
f_{yj} = yield stress of the steel jacket
D_j = outer diameter of the steel jacket

3.1.2 Wingwalls and Shear Keys

Wingwalls at seat-type abutments and shear keys were modeled as nonlinear displacement springs. The damage mode was assumed to be shear at the interface between the wall or key and the structural element to which it is attached. This was modeled using a nonlinear spring with essentially rigid-perfectly plastic behavior. The shear force at which yield occurs was calculated using the AASHTO shear-friction interface strength calculation, Equation 3.7 [2].

$$\begin{aligned} V_{fr} &= cA_{cv} + \mu(A_{vf}f_y + P_c) \\ &\leq K_1 f'_c A_{cv} \\ &\leq K_2 A_{cv} \end{aligned} \tag{3.7}$$

where

A_{cv}	=	area of concrete engaged in interface shear transfer (in^2)
A_{vf}	=	area of shear reinforcement crossing the shear plane (in^2)
f_y	=	yield stress of shear reinforcement (ksi)
c	=	cohesion factor (ksi)
μ	=	friction factor
P_c	=	permanent compressive load (kip)
K_1	=	fraction of concrete strength available to resist interface shear
K_2	=	limiting interface shear resistance

and Table 3.1 defines values used for c, μ, K_1, K_2 [2].

Table 3.1: Factors for Shear-Friction Interface Calculation

Shear Interface Factors	c	μ	K_1	K_2
Normal-weight concrete placed monolithically	0.40	1.4	0.25	1.5
Concrete placed against a clean concrete surface not intentionally roughened	0.075	0.6	0.2	0.8

3.1.3 Bearings

Laminated elastomeric bearings and steel roller bearings are each present in some study bridges. Bolted elastomeric bearings were modeled as linear elastic springs, with failure achieved at a shear strain of $\gamma = 300\%$. Unbolted elastomeric bearings and steel roller bearings were modeled as non-linear displacement springs with elastic perfectly plastic behavior, as illustrated in Figure 3.6.

Elastomeric bearing initial stiffness was calculated using Equation 3.8 [46]. The point at which plastic behavior begins depends on the damage mode (as discussed in Chapter 4).

$$K_v = \frac{GA}{h_{rt}} \tag{3.8}$$

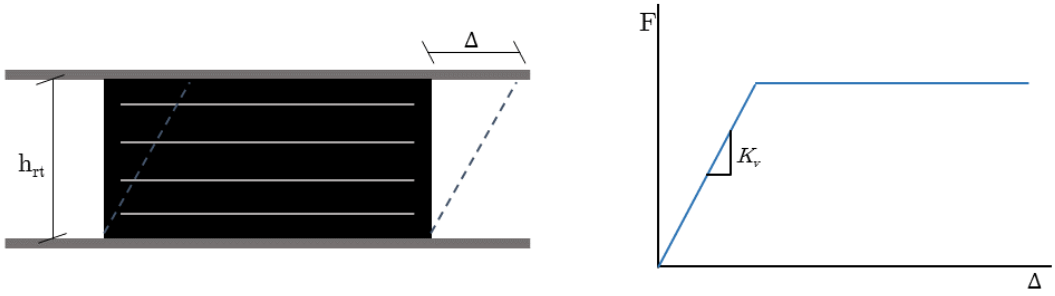

Figure 3.6: Illustration of elastomeric bearing model.

Steel roller bearings are designed to allow differential movement between elements in the longitudinal direction, but are not explicitly intended to contribute to transverse behavior of the structure. Therefore, it was assumed that the behavior of the roller bearings depended solely on the pintles that anchor them to the structural components they connect, and in the event the anchorage fails, the friction between the roller and bearing surfaces. The initial stiffness of the bearings was calibrated to account for both the strength of the pintles and the resistance to friction. The point at which the pintles shear is given by Equation 3.9.

$$P_u = f_u A_{pin} \tag{3.9}$$

3.1.4 Superstructure

Superstructure elements were assumed to behave rigidly, and therefore, when superstructure elements was required for a model, were represented by rigid elements. The dead load of the superstructure was calculated, and appropriately proportioned and applied as gravity loads to the pier elements. In the event that the longitudinal steel of columns extended into the superstructure, it was assumed that the connection was perfectly fixed.

3.1.5 Foundations

Soil-structure interaction is important to the performance of bridges during earthquakes. However, the focus of this project was on purely structural behavior of bridges, so only basic soil modeling was undertaken. It was assumed that pile- and mat- founded piers and

pile-founded abutments were fully fixed at the elevation of the pile cap or mat, regardless of whether the pile cap or mat was buried in soil. This assumption accounts for loss of support if soil subsides, but does not account for possible additional loading that may occur due to soil shifting. Spill-through abutments, which essentially consist of a pier buried in embankments [63], were treated like pile-founded piers, assuming that the soil in which the columns were buried was inadequately compacted.

For monolithic abutments without piles, resistance and strength of the soil mass was calculated. Elastic-perfectly plastic behavior was modeled, with sliding occurring after the failure of the soil mass. Equation 3.10 gives the pre-failure stiffness [28], and Equation 3.11 gives the strength of the soil mass [46].

$$K_s = \frac{E_s}{I(1-\nu)^2} \tag{3.10}$$

where I is a shape factor based on the dimensions of the soil mass resisting movement [28].

$$F_{soil} = 7.7bd \text{ (kips)} \tag{3.11}$$

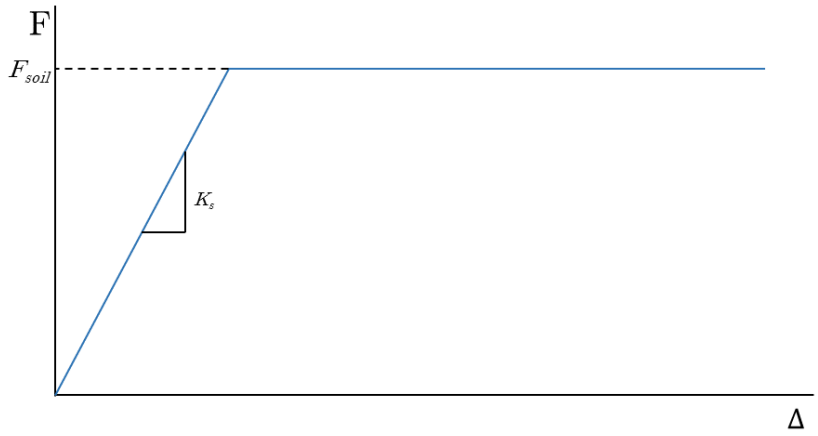

Figure 3.7: Modeled force-displacement behavior of the soil mass supporting monolithic abutments.

3.2 Bridge Selection

Though wide–scale evaluation of structures is one of the goals for the future of this project, this phase required a limited sample set of bridges to study. Study bridges are located in Washington State and were selected using the National Bridge Inventory (NBI) database.

3.2.1 NBI Database

The NBI was created in 1992 by the Federal Highway Administration (FHWA) to keep track of the bridge stock of the United States. State and local DOTs report the results of regular inspections to the FHWA, which then compiles the information into a comprehensive database. The NBI includes information such as location data, design and construction details, and the adequacy of the structure in a number of categories. Major systems of bridges are rated on a scale from "Failed" (a rating of zero) to "Excellent" (a rating of nine) [21].

The FHWA releases updates to the NBI on a yearly basis, and makes the database available to the public. The wide range of structures included, as well as the wealth of data available about each one, make the NBI an invaluable resource for identifying trends present in the bridge network.

3.2.2 WSDOT Bridge Stock

Though the techniques for analysis explored in this project are applicable to bridges throughout the country, the focus of this project is bridges owned by WSDOT. Selecting a single owner ensures that the standards to which inspections were conducted and maintenance was performed is as uniform as possible across the sample set.

According to the NBI, there are 8,158 bridges in Washington State. This number includes structures that carry rail, pedestrian, and automobile traffic. Approximately 7,300 carry automobiles, and of those, 3,100 are owned by WSDOT (the remainder are owned by local DOTs, federal agencies such as the National Park Service or military entities, or private owners) [61]. As can be seen in Figure 3.8, approximately 38% of WSDOT-owned bridges are reinforced concrete (RC). The widespread use of RC in Washington makes studying its performance necessary to assessing the overall resilience of the WSDOT bridge system.

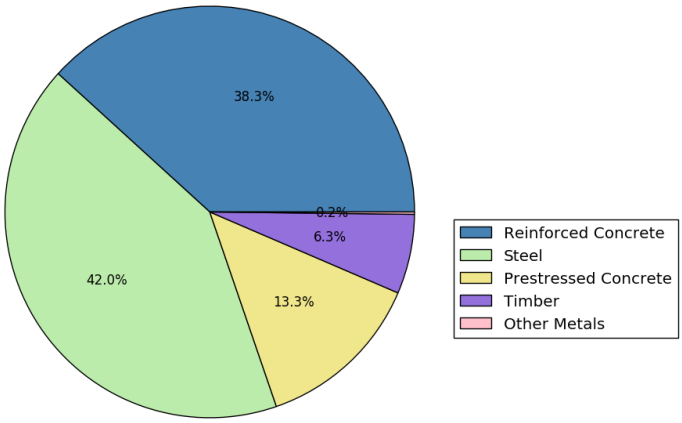

Figure 3.8: Breakdown of WSDOT's bridge stock (excluding culverts) by primary structural material.

The age range of bridges owned by WSDOT spans more than 100 years. As discussed in Chapter 2, a great deal of progress has been made in seismic design during that time. Though age of a structure is not the ultimate indicator of seismic resilience, it is a useful factor to examine. As can be seen in Figure 3.9, a large share of WSDOT's RC bridges were designed not only prior to the 1971 San Fernando earthquake, which precipitated major changes to national seismic design philosophy, but also prior to the two most recent local earthquakes. Therefore, a high number of bridges still in use today have inadequate or possibly unknown seismic capacity, and thus need examination.

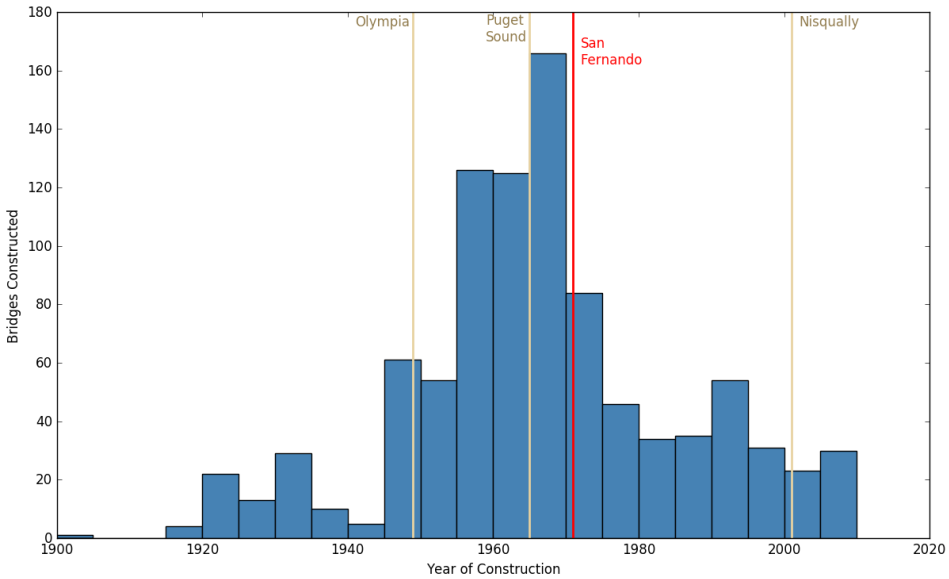

Figure 3.9: Year of construction of WSDOT's currently in-use RC bridges, with major earthquakes in the Washington State indicated in gold, and the 1971 San Fernando earthquake shown in red [23].

By examining the overall character of WSDOT's bridge stock, parameters can be determined that allow for selection of a small number of bridges that represent wider trends of the total inventory.

3.2.3 Study Bridge Parameters

Criteria used to select study bridges are outlined below:

Location Washington has regions of varied predicted seismic risk. The western portion of the state has the highest seismic risk, as quantified by the PGA with a 2% risk of exceedence in 50 years, as shown in Figure 3.10 [53]. This region also encompasses most of the areas of high population density in the state [39], further increasing the need for a resilient bridge network in the area. Study bridges were selected from within the western region of the state.

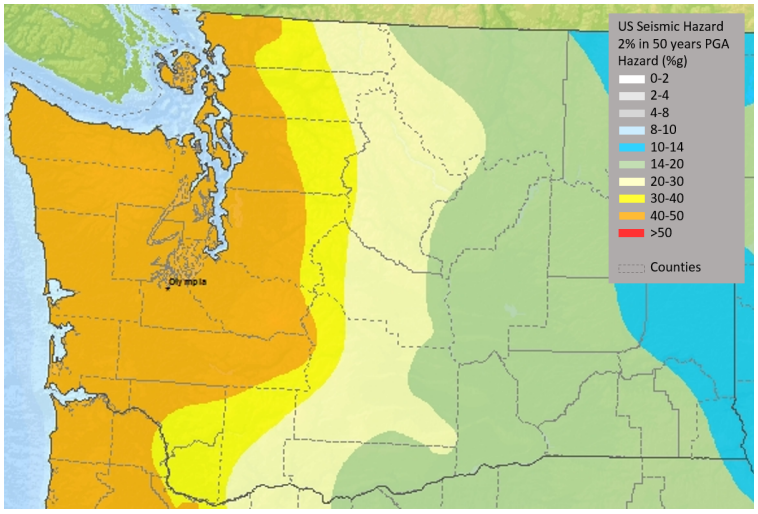

Figure 3.10: Predicted 2% chance of exceedence in 50 year PGAs for Washington State [53].

Geometry Geometry encompasses a number of properties in a bridge, but three were singled out as selection criteria for this project: skew, number of spans, and curvature. Though some structures include severe skew, large numbers of spans, or complex curvature, those structures are often designed in such a way to overcome site-specific obstacles. When possible, bridges tend to be relatively square, have only a handful of spans, and have centerlines that follow a straight (or nearly straight) line, to make design and construction as straightforward as possible. Therefore, the study bridges were selected to have a skew of 15°or less, fewer than 10 spans, and very little or no curvature along the centerline.

Condition Because condition of the structures was not explicitly accounted for in analysis, the bridges selected were screened to ensure none were considered to be in "Poor" (a rating of four) or worse in the categories of Deck, Superstructure, Substructure, and Overall Condition.

Variety Since the goal was to select somewhat typical structures to study, selecting for a certain amount of variety in design and construction allowed for a wide section of WSDOT's

bridge stock to be represented. Bridges were selected that were built during a range of design eras, since WSDOT's bridge stock covers a large span of time. Other sources of variety among selected bridges included structure length, clear height of piers, configuration of piers, and the number of spans in the structure.

3.3 Selected Bridges

Using the criteria outlined above, the following bridges were selected for study:

I-405 over May Creek Bridge 1, which is shown in Figure 3.11, was constructed in 1958. The superstructure consists of a deck slab with integral, haunched concrete girders, and is continuous over the piers. Piers consist of two rectangular, mat-founded columns, whose longitudinal rebar ties into the superstructure across a construction joint. The abutments are spill-through type abutments. Figure 3.12 shows the process of idealizing and modeling Bridge 1.

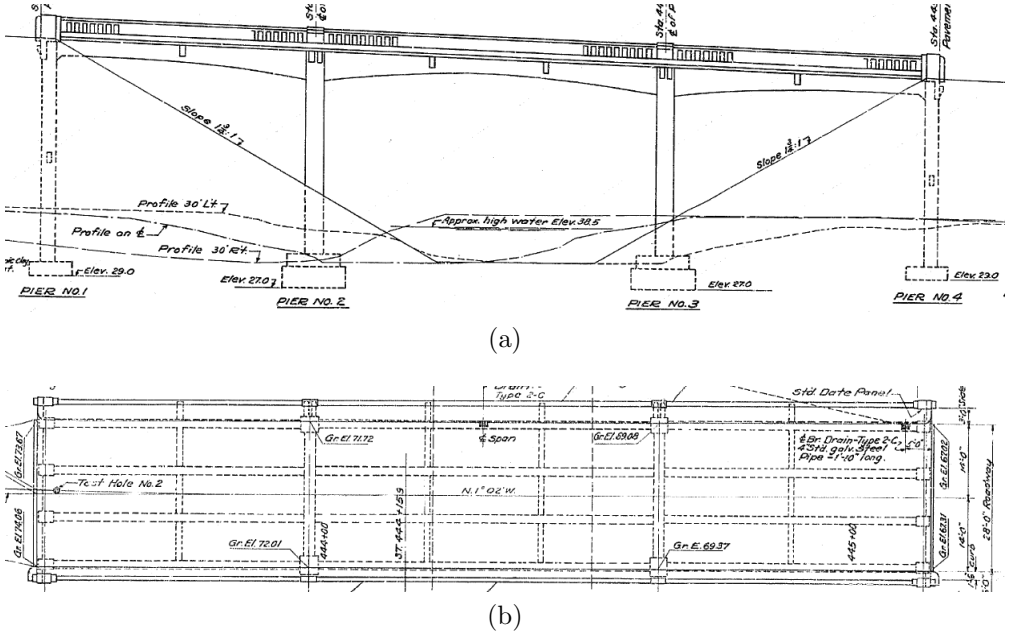

(a)

(b)

Figure 3.11: Bridge 1 in (a) elevation and (b) plan view

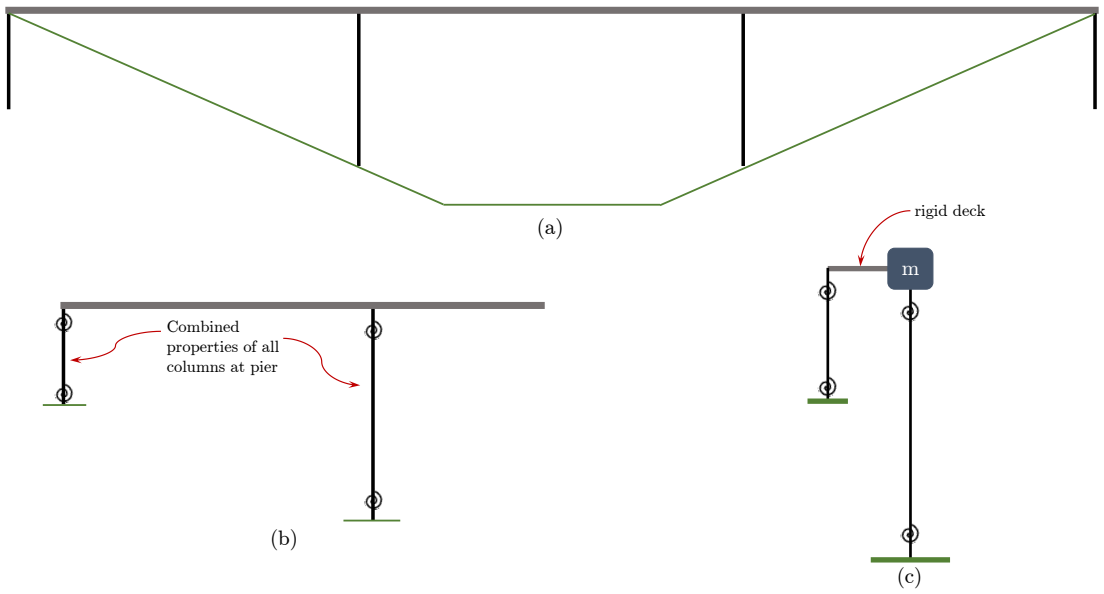

Figure 3.12: (a) idealization of Bridge 1, (b) reduction to essential sections, and (c) model

The specific values used to model the elements for Bridge 1 are laid out in Table 3.2.

Table 3.2: Model Properties of Bridge 1

(a) Pier 1 Sectional Properties

Property	Value	units
H	5.49	m
L_p	0.7978	m
EI_{eff}	953080	kN-m^2
M_y	4972	kN-m
Φ_y	0.00833	m^{-1}
M_u	4648	kN-m
Φ_u	0.0505	m^{-1}

(b) Pier 2 Sectional Properties

Property	Value	units
H	10.675	m
L_p	1.212	m
EI_{eff}	2144430	kN-m^2
M_y	6086	kN-m
Φ_y	0.00462	m^{-1}
M_u	5910	kN-m
Φ_u	0.0248	m^{-1}

(c) Loading

Property	Value	units
Deck	2933	kN

I-5 Reversible Express Lanes over James and Cherry Streets Bridge 2, which is shown in Figure 3.13, was constructed in 1975. Nine spans comprise three deck units.

The superstructure is a concrete box girder, which is continuous over circular, single column, pile-founded piers. The longitudinal rebar in the columns extends into the box girder across a construction joint. Seismic retrofits completed in 2001 added steel jackets to the piers to increase shear capacity, and were included in the model. At the seat abutment, four elastomeric bearings support the superstructure. In the name of simplicity, only the center unit, Unit 2, was modeled. Figure 3.14 shows the process of idealizing and modeling Bridge 2.

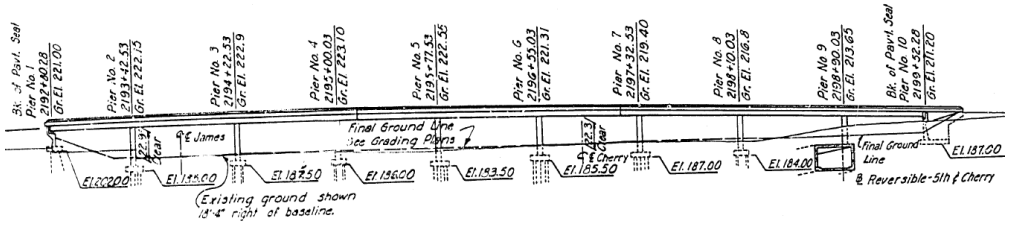

(a)

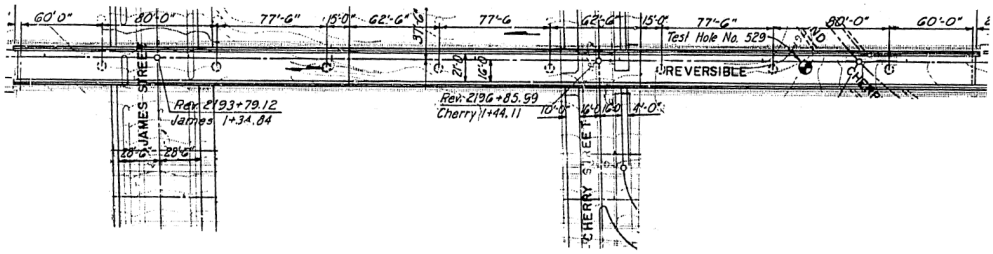

(b)

Figure 3.13: Bridge 2 in (a) elevation and (b) plan view

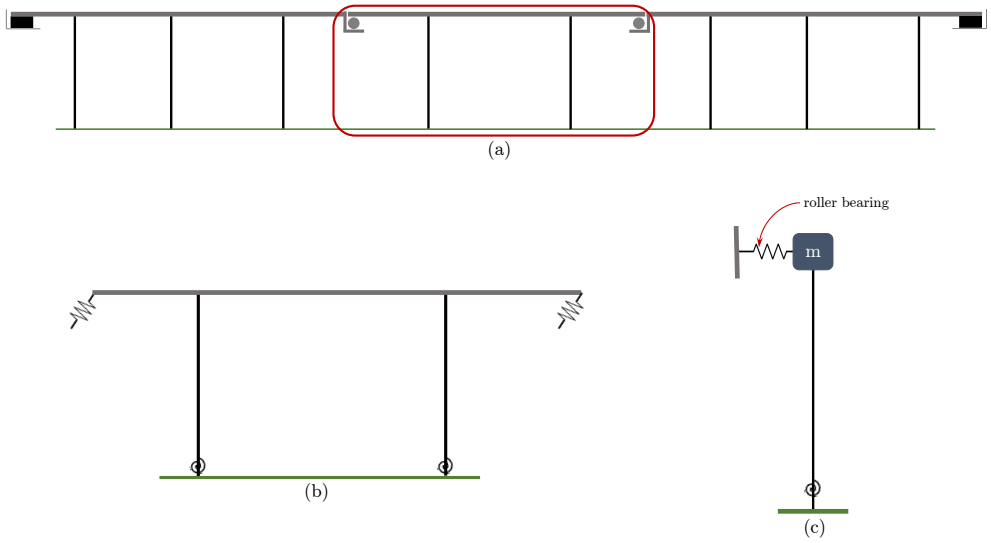

Figure 3.14: (a) idealization of Bridge 2, (b) isolation and idealization of Unit 2, and (c) model

The specific values used to model the elements for Bridge 2 are laid out in Table 3.3.

Table 3.3: Model Properties of Bridge 1

(a) Pier Sectional Properties

Property	Value	units
H	8.01	m
L_p	1.06	m
EI_{eff}	2611211.6	kN-m^2
M_y	11467	kN-m
Φ_y	0.00440	m^{-1}
M_u	12102	kN-m
Φ_u	0.0283	m^{-1}

(b) Roller Bearing Properties

Property	Value	units
K_z	26570	kN/m
F_y	5463	kN

(c) Loading

Property	Value	units
Deck	5513	kN

SR 522 over Elliot Road Bridge 3, which is shown in Figure 3.15, was constructed in 1961. The bridge has three spans, and the superstructure is a slab deck, which is continuous over the piers. Piers consist of two mat-founded columns joined by a pier cap that is integral

to the deck. The longitudinal rebar in the columns extends into the slab across a construction joint. The deck-abutment connection, which was modeled as a pin connection, is illustrated in Figure 3.16. The abutments are spill-through type abutments. Figure 3.17 shows the process of idealizing and modeling Bridge 1.

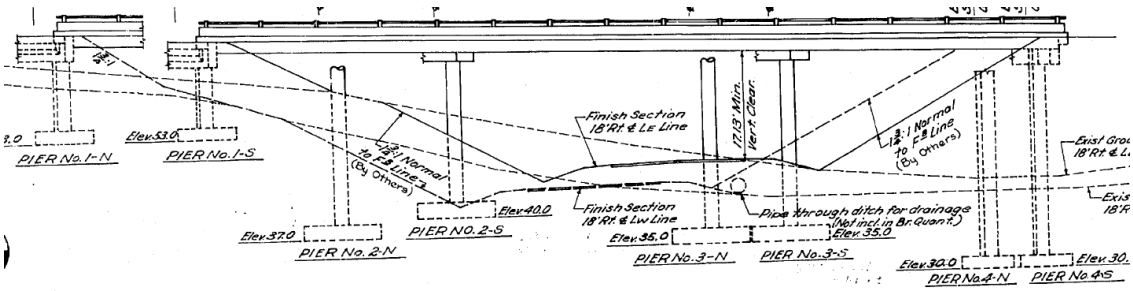

(a)

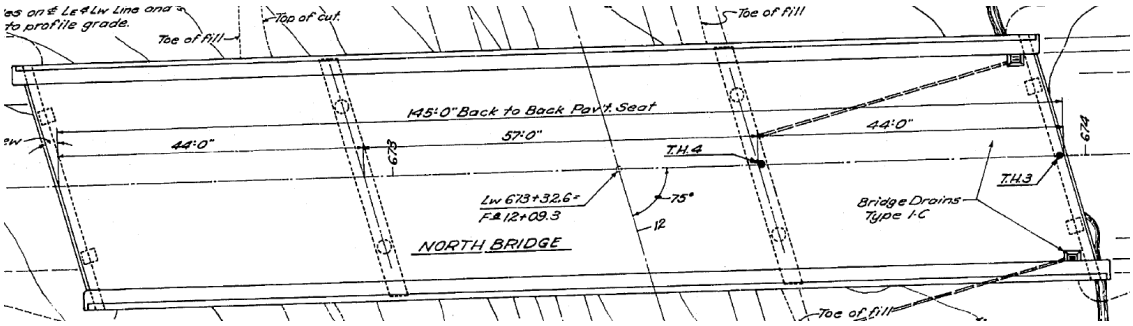

(b)

Figure 3.15: Bridge 3 in (a) elevation and (b) plan view

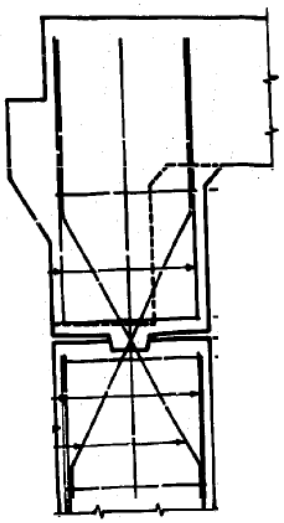

Figure 3.16: A pin connection is created between the superstructure and substructure of Bridge 3 by arranging the rebar such that all bars cross between the abutment and superstructure in the same plane.

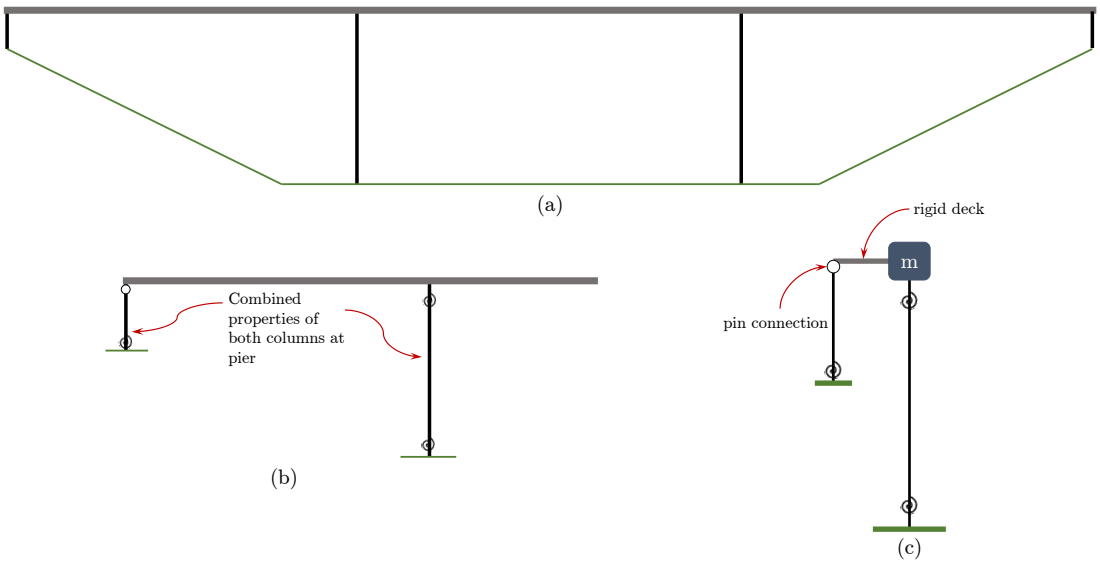

Figure 3.17: (a) idealization of Bridge 3, (b) reduction to essential sections, and (c) model

The specific values used to model the elements for Bridge 3 are laid out in Table 3.4.

Table 3.4: Model Properties of Bridge 3

(a) Pier 1 Sectional Properties

Property	Value	units
H	4	m
L_p	0.71	m
EI_{eff}	282880	kN-m^2
M_y	2272	kN-m
Φ_y	0.00800	m^{-1}
M_u	2530	kN-m
Φ_u	0.184	m^{-1}

(b) Pier 2 Sectional Properties

Property	Value	units
H	9	m
L_p	1.0810	m
EI_{eff}	304640	kN-m^2
M_y	3304	kN-m
Φ_y	0.0107	m^{-1}
M_u	3452	kN-m
Φ_u	0.0561	m^{-1}

(c) Loading

Property	Value	units
Deck	1963	kN

I-405 over SR 524 Bridge 4, which is shown in Figure 3.18, was constructed in 1968. The bridge consists of three spans, and the superstructure is a box girder, which is continuous over the piers. Piers consist of two mat-founded circular columns, and the longitudinal rebar extends into the superstructure across a construction joint. The superstructure rests on five unbolted elastomeric bearings at the seat-type abutments. Figure 3.19 shows the process of idealizing and modeling Bridge 1.

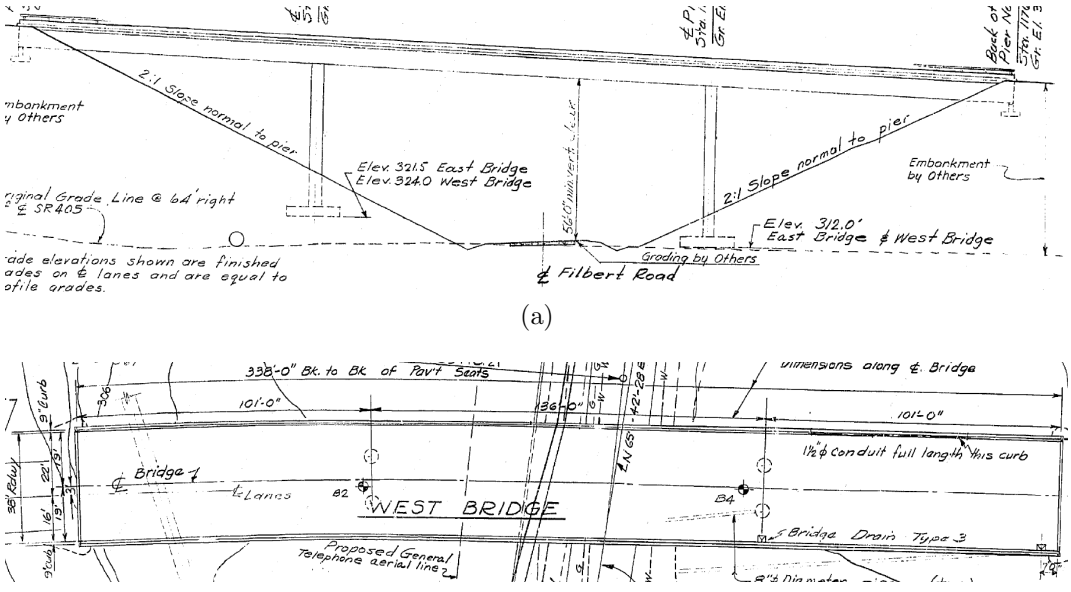

Figure 3.18: Bridge 4 in (a) elevation and (b) plan view

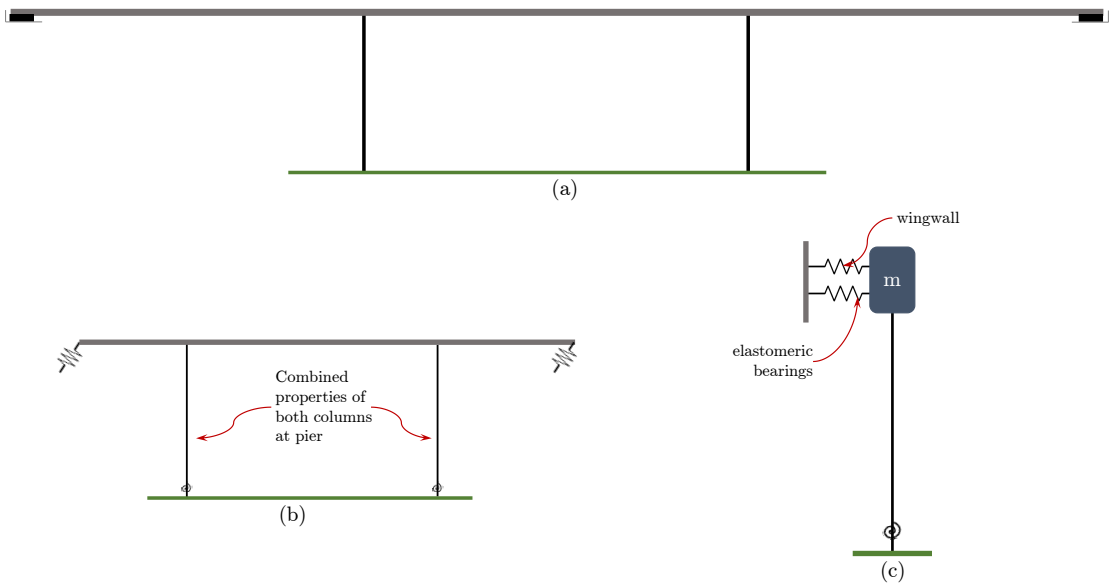

Figure 3.19: (a) idealization of Bridge 4, (b) reduction to essential sections, and (c) model

The specific values used to model the elements for Bridge 4 are laid out in Table 3.5.

Table 3.5: Model Properties of Bridge 4

(a) Pier Sectional Properties

Property	Value	units
H	15.0	m
L_p	1.58	m
EI_{eff}	248075	kN-m^2
M_y	6256	kN-m
Φ_y	0.00404	m^{-1}
M_u	6814	kN-m
Φ_u	0.0384	m^{-1}

(b) Abutment Wingwall Properties

Property	Value	units
V_n	1673	kN

(c) Elastomeric Bearing Properties

Property	Value	units
K_z	15467	kN/m
F_y	2103	kN

(d) Loading

Property	Value	units
Deck	5513	kN

SR 202 over Kimball Creek Bridge 5, which is shown in Figure 3.20, was constructed in 1924. The superstructure, which is continuous over the two piers, consists of a deck slab with integral girders. Each pier consists of four rectangular columns that all tie into a single pile cap, and whose longitudinal steel extends into the girders across a construction joint. The abutments are spill-through type abutments. Figure 3.21 shows the process of idealizing and modeling Bridge 5.

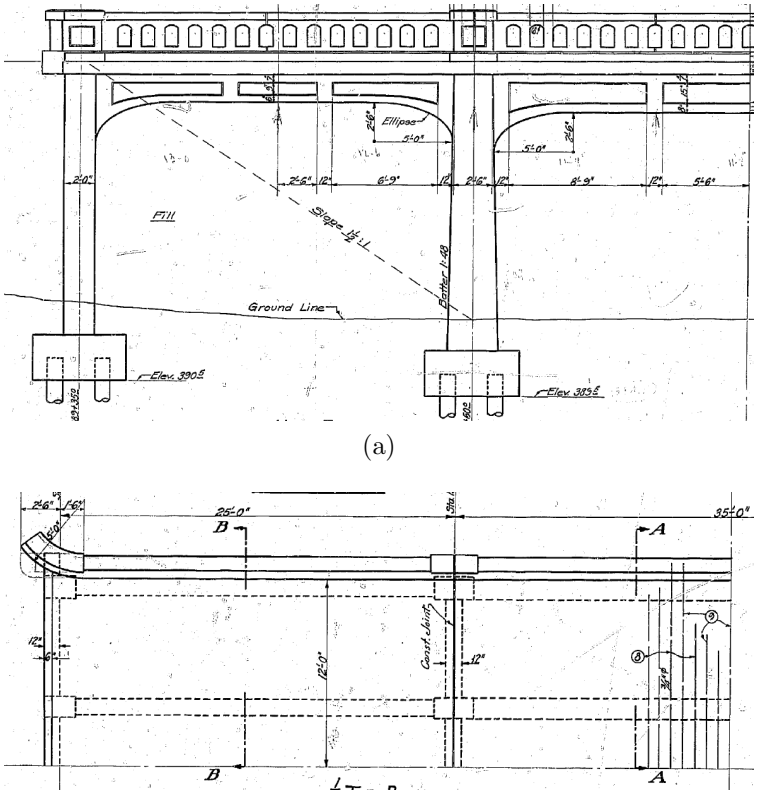

(a)

(b)

Figure 3.20: Bridge 5 in (a) half elevation and (b) quarter plan view

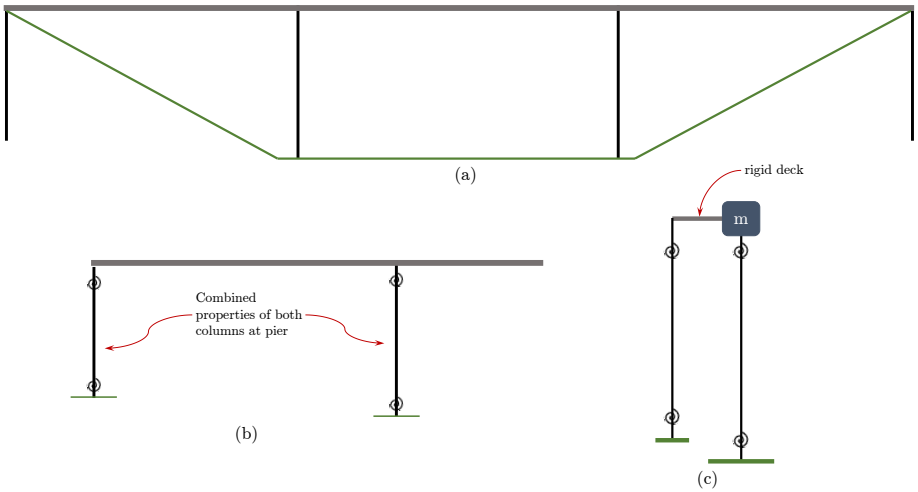

Figure 3.21: (a) idealization of Bridge 5, (b) reduction to essential sections, and (c) model

The specific values used to model the elements for Bridge 5 are laid out in Table 3.6.

Table 3.6: Model Properties of Bridge 5

(a) Pier 1 Sectional Properties

Property	Value	units
H	4.3	m
L_p	0.505	m
EI_{eff}	70065	kN-m^2
M_y	479.2	kN-m
Φ_y	0.00683	m^{-1}
M_u	529.6	kN-m
Φ_u	0.313	m^{-1}

(b) Pier 2 Sectional Properties

Property	Value	units
H	4.8	m
L_p	0.546	m
EI_{eff}	55903	kN-m^2
M_y	384.6	kN-m
Φ_y	0.00682	m^{-1}
M_u	468.8	kN-m
Φ_u	0.3087	m^{-1}

(c) Loading

Property	Value	units
Deck	1232	kN

I-90 over SR 202 Bridge 6, shown in Figure 3.22, was constructed in 1975. The bridge has three spans. The superstructure is a haunched concrete box girder, and the substructure consists of two tapered columns at each pier, and pile-founded seat abutments. The superstructure rests on unbolted elastomeric bearings (one on each column and six at each abutment). Figure 3.23 shows the process of idealizing and modeling Bridge 6.

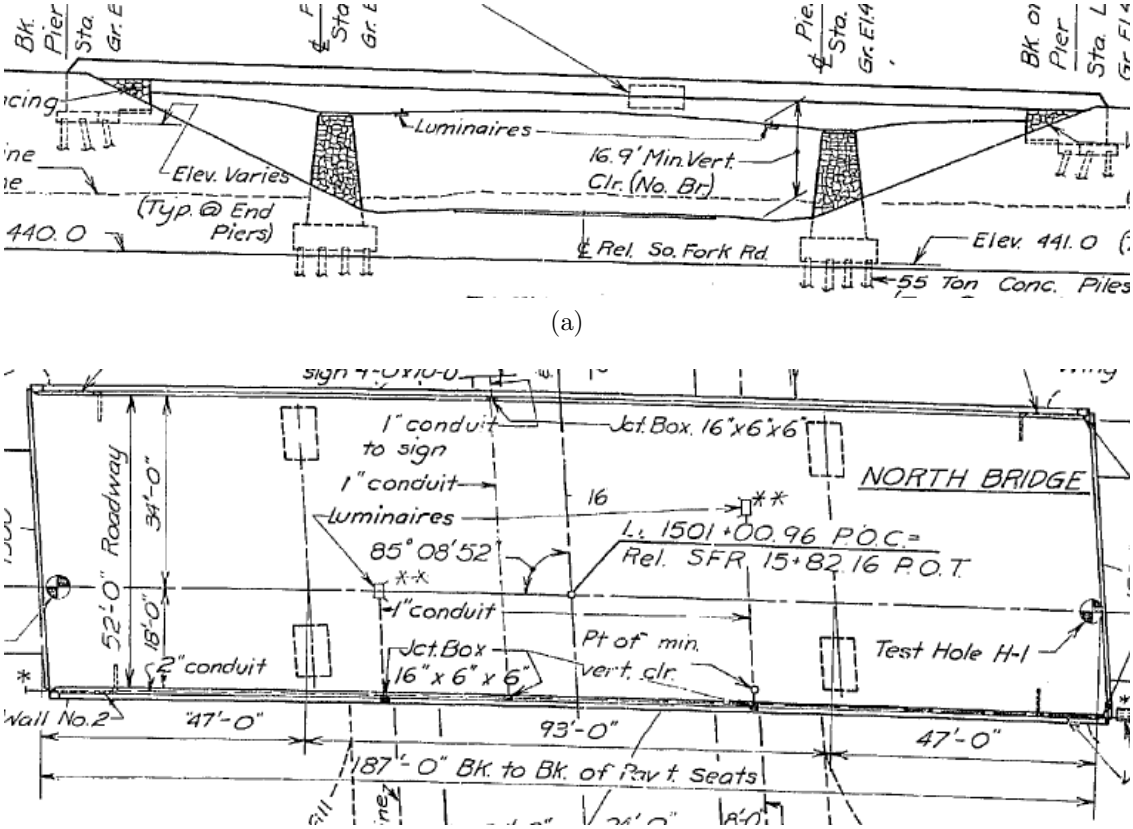

Figure 3.22: Bridge 6 in (a) elevation and (b) plan view

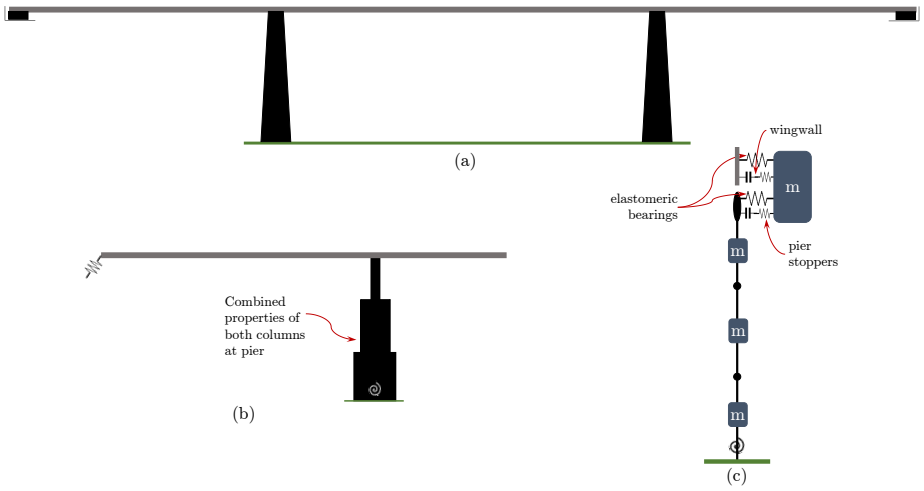

Figure 3.23: (a) idealization of Bridge 6, (b) reduction to essential sections, and (c) model

The specific values used to model the elements for Bridge 6 are laid out in Table 3.7. Due to the relatively large mass of the piers, their mass was included in the model, and applied along the height of the column.

Table 3.7: Model Properties of Bridge 6

(a) Pier 1 Sectional Properties

Property	Value	units
H	4.3	m
L_p	0.88	m
EI_{eff}	37436518 24742113 19496437	kN-m^2
M_y	72608	kN-m
Φ_y	0.00104	m^{-1}
M_u	94574	kN-m
Φ_u	0.0142	m^{-1}

(b) Pier Bearing Properties

Property	Value	units
K_z	11656753	kN/m
F_y	1013.5	kN

(c) Abutment Bearing Properties

Property	Value	units
K_z	552623	kN/m
F_y	80	kN

(d) Pier Stopper Properties

Property	Value	units
K_z	6420768	kN/m
F_{fr}	1233	kN

(e) Abutment Wingwall Properties

Property	Value	units
K_z	10015425	kN/m
F_{fr}	1930	kN

(f) Loading

Property	Value	units
Lower	986	kN
Middle	448	kN
Upper	345	kN
Deck	5067	kN

US 101 over Perry Creek Bridge 7, which is shown in Figure 3.24, was constructed in 1957. The box girder superstructure is continuous over the two piers, which are laid out such that the end spans are much shorter than the center span. At each pier, eleven pile-bents, which are columnar structural members that serve as both bent and pile at a pier, support the superstructure, whose longitudinal rebar ties into the superstructure across a construction joint. The abutments consists solely of a diaphragm section embedded in the embankment. Figure 3.25 shows the process of idealizing and modeling Bridge 7.

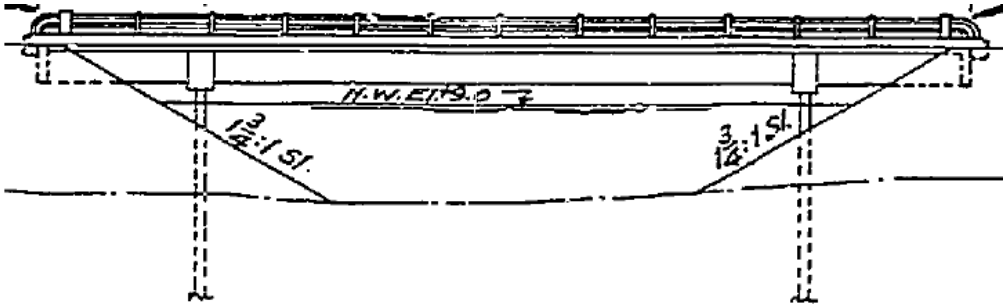

(a)

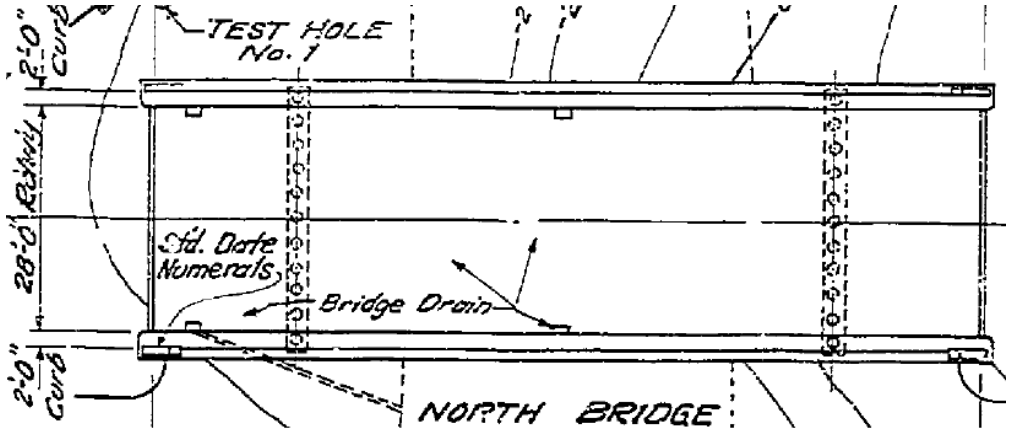

(b)

Figure 3.24: Bridge 7 in (a) elevation and (b) plan view

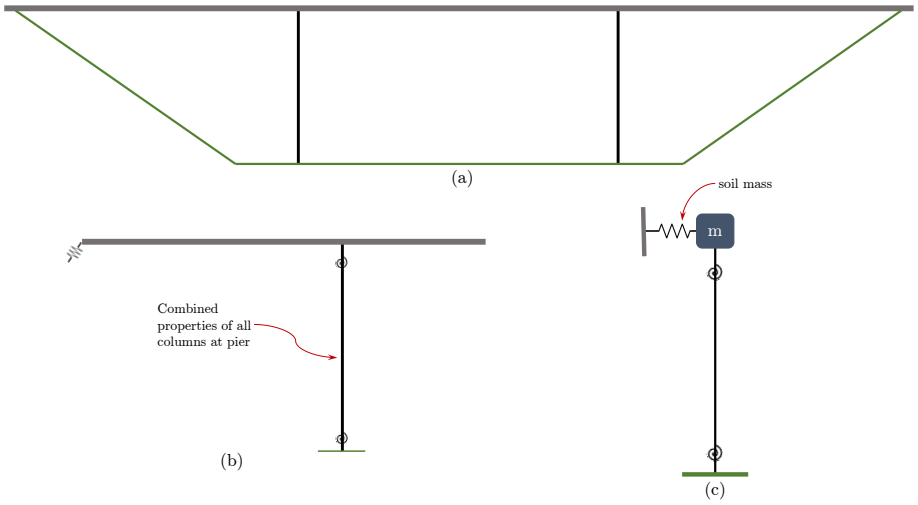

Figure 3.25: (a) idealization of Bridge 7, (b) reduction to essential sections, and (c) model

The specific values used to model the elements for Bridge 7 are laid out in Table 3.8

Table 3.8: Model Properties of Bridge 7

(a) Pier Sectional Properties

Property	Value	units
H	15.0	m
L_p	1.58	m
EI_{eff}	248075	kN-m^2
M_y	6256	kN-m
Φ_y	0.00404	m^{-1}
M_u	6814	kN-m
Φ_u	0.0384	m^{-1}

(b) Soil Mass Properties

Property	Value	units
K_s	33483	kN/m
F_{soil}	342.5	kN

(c) Loading

Property	Value	units
Deck	2074	kN

Chapter 4

ANALYSIS PROCEDURE

4.1 Damage States

In order to define coherent Performance Levels, it is convenient to group DSs of different structural systems into broadly defined categories based on the extent of damage experienced. For this project, four Performance Levels (PLs) were defined as follows, based on the work of Cardone, et al [15]:

PL1 Minor damage. Easily repaired, requiring little to no downtime before reopening.

PL2 Moderate damage. Widespread damage has occurred, but there is still a comfortable margin against collapse, and repair is both physically and economically feasible.

PL3 Severe Damage. There is some remaining margin against collapse. The damage that has occurred would technically be repairable, but replacement of the structure would likely be more economical.

PL4 Collapse Prevention. Global collapse has not occurred, but aftershocks or other additional loading may trigger global collapse. PL4 should be avoided when determining design objectives.

Table 4.1 outlines the parameters used to define DSs corresponding to the four PLs for different structural elements [15].

Table 4.1: Damage States of Structural Elements Corresponding to Performance Level

Element	Failure Mode	PL1	PL2	PL3	PL4
Piers	Flexure Shear	d_y –	$d_y + \frac{(d_u - d_y)}{2}$ d_{cr}	$d_y + \frac{2(d_u - d_y)}{3}$ d_{sh}	d_u $1.1d_{sh}$
Wingwalls and Shear Keys	Shear-Friction	d_{gap}	–	V_{fr}	–
Unbolted Elastomeric Bearings	Friction Rollover	d_{fr} $\frac{d_{pad}}{3}$	$d_{fr} + \frac{d_{pad} - d_{fr}}{3}$ $\frac{d_{pad}}{2}$	d_{pad} d_{pad}	d_{uns} d_{uns}
Bolted Elastomeric Bearings	Material Failure	$d_{\gamma=150\%}$	$d_{\gamma=200\%}$	$d_{\gamma=300\%}$	d_{uns}
Steel Roller Bearings		–	V_{pin}	V_{fr}	–

The displacements are calculated as follows:

4.1.1 Piers

For flexural displacements, Equations 4.1 and 4.2 are used to calculate the displacement at yielding of the rebar and ultimate failure of the piers [15].

$$d_y = \phi_y \frac{(L + C_f L_{sp})^2}{3} \tag{4.1}$$

$$d_u = d_y + (\phi_u - \phi_y) L_p C_f (L - \frac{L_p}{2}) \tag{4.2}$$

The equation governing displacement of the tip of a cantilever subjected to a point load (equal to the total base shear, V_b) at the free end, Equation 4.3, was used to determine the displacement corresponding to shear damage modes.

$$d_v = \frac{V_b L^3}{3EI} \tag{4.3}$$

4.1.2 Wingwalls and Shear Keys

In the event of a gap between a wingwall or shear key and the element resisting its movement, the displacement required to close that gap is d_{gap}. Because of the rigid behavior of the element after gap closure up to shear-friction interface failure, the DS for PL3 is assessed

in terms of force, rather than displacement. The calculation to determine V_{fr} is given in Chapter 3.

4.1.3 Bearings

Bolted elastomeric bearings undergo material failure at a shear strain (γ) of approximately 300%, and displacements based on γ are calculated using Equation 4.4. Unbolted elastomeric bearings are prone to connection failures, such as rollover, when the edges of the bearing begin to rotate away from the bearing surface, or sliding, when shear forces overcome the force of friction between the bearing and adjacent structural elements, which is $F_{fr} = P\mu$. d_{pad} is equal to the dimension of the bearing in the direction of motion. d_{uns} refers to the displacement at which unseating of the superstructure occurs, which in the case of pier bearings, was taken to be a displacement equal to the dimension of the pier in the direction of motion.

$$d_i = t_r \gamma_i \tag{4.4}$$

4.2 Construction of Equivalent SDOF Systems

After the determination of DSs for a bridge, an equivalent damped linear elastic single degree of freedom (SDOF) system for each DS had to be described. The motivation for this is that the spectra used in the prediction of PGAs associated with the DSs were associated with elastic SDOF systems. The bridge models were not elastic SDOF systems, so in order for the spectra to be scaled appropriately, determining an equivalent system was necessary for each DS. After an equivalent linear elastic SDOF system was determined, the PGAs associated with each DS could be calculated accordingly.

All equations in this section, with the exception of Equation 4.10, are taken from the work of Cardone, et al ([14],[15],[16]).

The equivalent displacement, mass, stiffness, and period at each DS was calculated for the

system using Equations 4.5, 4.6, 4.7, and 4.8. m_i and Δ_i refer to the mass and displacement of nodes in the models with masses assigned to them at the DS.

$$\Delta_e = \frac{\sum(m_i \Delta_i^2)}{\sum(m_i \Delta_i)} \tag{4.5}$$

$$m_e = \frac{\sum(m_i \Delta_i)}{\Delta_e} \tag{4.6}$$

$$k_e = \frac{V_b}{\Delta_e} \tag{4.7}$$

$$T_e = 2\pi\sqrt{\frac{m_e}{k_e}} \tag{4.8}$$

In order to calculate the damped elastic response spectrum appropriate for the equivalent SDOF system, the damping ratio of the equivalent SDOF was calculated using Equation 4.9, which incorporates the damping contributions of the different structural systems.

$$\xi_e = \frac{\sum_i^{nb} \xi_{b,i} F_{b,i} \Delta_{b,i} + \sum_i^{np} \xi_{p,j} F_{p,j} \Delta_{p,j}}{\sum_i^{nb} F_{b,i} \Delta_{b,i} + \sum_i^{np} F_{p,j} \Delta_{p,j}} \tag{4.9}$$

where $\xi_{b,i}$, $F_{b,i}$, and $\Delta_{b,i}$ refer to the damping ratio, internal force, and displacement of bearing element i, and $\xi_{p,j}$, $F_{p,j}$, and $\Delta_{p,j}$ the damping ratio, force, and displacement of pier j. nb is the total number of bearings, and np is the total number of piers in the structure.

The damping ratio for bearings was calculated using the Jacobsen approach [27], as shown in Equation 4.10.

$$\xi_{b,i} = \frac{E_{visc} + E_{hyst} + E_{fr}}{2\pi F \Delta} \tag{4.10}$$

The damping ratio for piers was taken to be 5% prior to yield of the longitudinal rebar, and Equation 4.11 was used to calculate post-yield damping.

$$\xi_{p,j} = 0.05 + \frac{1}{\pi}\left(1 - \frac{1-r}{\sqrt{\mu}} - r\mu\right) \tag{4.11}$$

4.3 Ground Motion Selection

In order to gauge the accuracy of predictions based on pushover analysis, a suitable suite of test ground motions was selected for comparison. AASHTO requires at least seven time histories be run if the average result from a suite of time histories is to be used to represent the response of a bridge [2]. For this project, 20 ground motions were selected, and the average response was used.

4.3.1 Determining Parameters

The USGS provides a suite of earthquake hazard tools to the public. These tools include location-specific hazard assessments for any location in the country. The Seismic Design Maps provide users with a target spectrum, which can then be incorporated into seismic design of a structure. The Hazard Deaggregation Tool breaks down the distribution of ground motions contributing to the site hazard, indicating the expected epicentral distance and magnitude. Since shaking due to a nearby (<10 km epicentral distance) earthquake can have distinct characteristics from those farther afield, it is important to consider distance to potential epicenters when selecting ground motions.

After comparing the target spectra and deaggregations of all the study bridges, it was determined that they were similar enough that a single location could be used to establish the site hazard for all bridge locations. The geographic center of the locations of the study bridges was chosen for this purpose. The target spectrum and deaggregation information for that location were used in selecting appropriate ground motions.

4.3.2 PEER Database

The Pacific Earthquake Engineering Research Center (PEER) maintains a database of ground motion recordings from hundreds of shallow crustal earthquakes from around the world known as NGA-West2. Altogether in the collection there are over 21,000 time histories from

earthquakes ranging in magnitude from M_w=3.0 to M_w=7.9 at epicentral distances of 0.05 to 1,533 km.

Users can filter ground motions to match the characteristics of expected earthquakes at a location. Filters include moment magnitude, epicentral distance, and earthquake type. By matching the suite of ground motion time histories used to analyze the structure to the anticipated shaking at the location, more realistic results can be obtained from NLTH [3].

4.3.3 Scaling to Match Predictions

Although PEER allows users to download time history files that have been scaled to match a requested target spectrum, raw ground motions were obtained for this project. Because the target spectrum assumes 5% damping of structures, which may not be the case once elements have begun to exhibit nonlinear behavior, the target spectrum does not necessarily reflect the final scaling necessary to achieve selected damage states. Such scaling, which is described in detail in Section 4.3.5, was therefore performed on the raw time histories for ease of calculation. Two different scaling methods, described in Section 4.3.5, were employed, in order to determine if one was superior in producing appropriate spectra.

4.3.4 Selected Ground Motions

Table 4.2 gives information about the ground motion time histories chosen for use in the NLTH analyses. Due to the decision to work with initially unscaled ground motions, comparing the target spectrum for the geographic center of the bridges to the average unscaled spectrum reveals a mismatch. However, by using data from an actual DS (in the example in Figure 4.1, the yielding of Pier 1 in Bridge 1), scaled spectra are produced that more closely resemble the smoothed spectrum.

Table 4.2: Ground motion time histories chosen for NLTH analyses

GM ID	PEER RSN	EQ Name	Year	M_w	Station	PGA (g)
GM1	31	Parkfield	1966	6.0	Cholame-Shandon Array #8	0.24752
GM2	36	Borrego Mountain	1968	6.5	El Centro Array #9	0.16241
GM3	70	San Fernando	1971	6.61	Lake Hughes #1	0.15143
GM4	72				Lake Hughes #4	0.19777
GM5	88				San Felita Dam	0.15488
GM6	125	Friuli, Italy	1976	6.5	Tolmezzo	0.35524
GM7	162	Imperial Valley	1979	6.53	Calexico Fire Station	0.27699
GM8	164				Cerro Prieto	0.16829
GM9	167				Compuertas	0.18664
GM10	169				Delta	0.23569
GM11	176				El Centro Array #13	0.11796
GM12	186				Niland Fire Station	0.10965
GM13	265	Victoria, Mexico	1980	6.33	Cerra Prieto	0.64538
GM14	266				Chihuahua	0.15098
GM15	268				SAHOP Casa Flores	0.10094
GM16	288	Irpinia, Italy	1980	6.9	Brienza	0.21946
GM17	289				Calitri	0.12642
GM18	291				Rionero In Vulture	0.09583
GM19	322	Coalinga	1983	6.36	Cantua Creek School	0.22533
GM20	326				Parkfield-Cholame 2WA	0.10971

4.3.5 Damped Spectra Generation

Once the damping ratio of the equivalent SDOF system is calculated for a DS, an appropriately damped response spectrum could be produced in order to determine the PGA predicted for the DS. For each DS, two different methods of producing appropriately scaled PGA values were compared. Both methods begin by calculating the equivalent spectral acceleration by rearranging $F = ma$ to yield $S_e = V_b/m$, which is then converted into units of g for convenience.

The first scaling method, described by Cardone ([14], [15], [16]), calculates a damping reduction factor (η) in order to determine the scaling of a 5% damped target spectrum to match

the SDOF equvilent damping. The calculation of the damping factor used in this project, which is shown in Equation 4.12, comes from Eurocode 8 [12]. The damping factor is limited to a values greater than 0.5, which corresponds to a ξ_e value of 26% [16].

$$\eta = \sqrt{\frac{7}{2+\xi_e}} \geq 0.5 \tag{4.12}$$

The reduced ground spectral acceleration (S_{a1}) is then calculated using the spectral acceleration (S_{T5}) of a structure with period T_e, and the ground acceleration from the 5% damped spectrum (S_{a5}), as shown in Equation 4.13 [16]

$$S_{a1} = \frac{S_{T5}}{S_{a5}}\eta \tag{4.13}$$

The second, unsmoothed scaling method, tested in this project, uses the response spectrum produced by averaging the spectra of the 20 selected ground motions. This scaling method was tested in order to determine if increased accuracy could be attained by using the spectra from real ground motions, rather than the smoothed target spectrum generated for a site. The equivalent damping, ξ_e, of the system is used in creating the spectra produced from the raw ground motion time histories. Inherently, no limit is placed on the damping for which scaling can be done. However, to compare the two scaling methods, in cases where bridges had $\xi_e \geq 25\%$, both limited and non-limited spectra were produced for comparison. S_{a1} is then calculated using Equation 4.14 (adapted from Cardone, et al [16]).

$$S_{a1} = \frac{S_{T\xi}}{S_{a5}} \tag{4.14}$$

Both scaling methods use the same equations to determine the predicted PGA and resulting scale factor needed to be applied during NLTH analysis. The predicted PGA is calculated using Equation 4.15, and the scale factor is calculated by dividing the predicted PGA by the PGA of the average of the unscaled ground motion time histories [15].

$$PGA_{DS} = \frac{S_e}{S_{a1}} \tag{4.15}$$

Figure 4.1 shows the scaled spectrum generated for DS2 for Bridge 1, for which $T_e = 0.368$s,

S_e = 0.809g, and ξ = 5%. The blue spectrum shows the suite-average spectrum scaled according to Cardone's method, and the purple spectrum used the unsmoothed method.

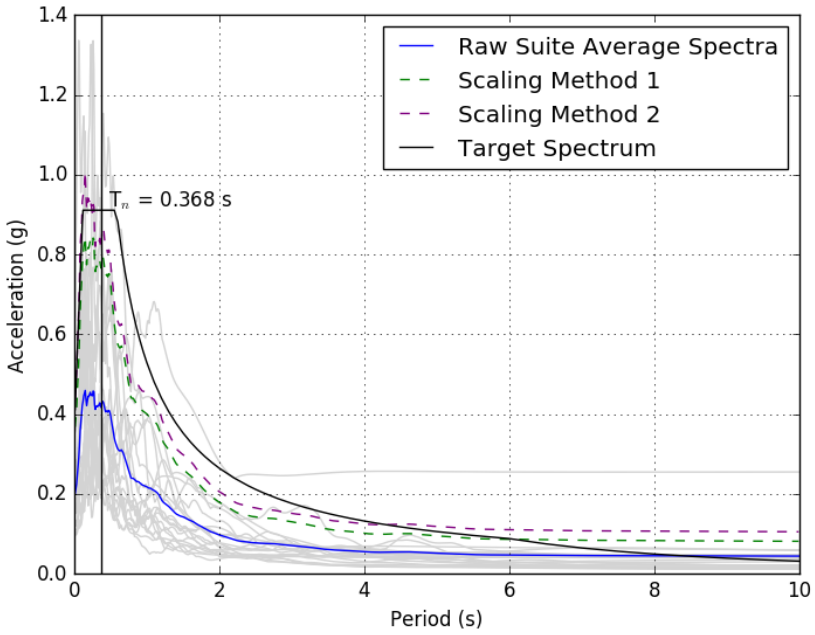

Figure 4.1: Using values calculated for Bridge 1, the raw ground motions were scaled using two different scaling methods to match the 5% damped spectrum.

4.4 Error Calculation

In order to compare the results of the pushover to those seen in the scaled NLTH analyses, it was important to quantify the degree of error. Cardone presents an error index that is calculated based on comparison between displacements seen in the pushover and the average result of all NLTH analyses [15]. Equation 4.16 shows this, where i refers to the DS number.

$$err_i = \frac{d_{i,push}}{\text{ave}(d_{i,NLTH})} \tag{4.16}$$

A perfect PGA prediction would yield an err_i value of 1.0. Error values of greater than 1.0 indicate that a lower displacement was reached during the NLTH analysis than predicted. This indicates that the predicted PGA at which that DS would be reached is higher than predicted. Error values less than 1.0 indicate that the PGA at which the DS would be reached is lower than predicted. Therefore, err_i values greater than 1.0 are preferred, as it

denotes a conservative prediction.

In categorizing the accuracy of predictions, error values between 0.75 and 1.25 were considered "Satisfactory," values between 0.5 and 0.75 and between 1.25 and 2.0 were considered "Moderate," and values less than 0.5 or greater than 2.0 were considered "Poor."

4.5 Capturing Uncertainty

Though a single value of PGA precipitating a DS can be calculated by using the above procedure, reporting a single PGA value fails to capture the uncertainty inherent in the assumed capacity and the demand. Uncertainty of capacity accounts for unknowns in the structure itself. Material properties such as strength of concrete and steel are specified and producers work to ensure compliance, however, assuming a single exact value for strength is not realistic. Additionally, imperfections can be introduced during the construction process. In order to quantify that uncertainty, fragility curves showing the probability a given PGA will result in reaching a given DS were constructed.

Compounding structural uncertainty is the uncertainty of the seismic hazard, discussed in Chapter 2. To account for this, a site hazard curve can be constructed to show the probability that a ground shaking of a given intensity will be exceeded at a particular site in a year.

By combining the structural uncertainty with the seismic hazard uncertainty, a Risk Index, R, can be calculated for each DS, which captures in a single value the vulnerability of a bridge to reaching that DS.

Unless specified otherwise, the information and equations in this section are drawn from the work of Porter ([45]).

4.5.1 Fragility Curves

Assuming that both capacity and demand are random variables with normal or lognormal distribution, the Central Limit Theorem states that the composite probability has a log-

normal distribution. Equation 4.17 defines the cumulative distribution function (CDF) of a lognormally distributed random variable.

$$P\left[X \leq x\right] = \Phi\left(\frac{\ln(x/\theta)}{\beta}\right) \tag{4.17}$$

where

X	=	excitation during a given earthquake (PGA)
x	=	a defined level of exchitation (PGA)
Φ	=	standard normal cumulative distribution function)
θ	=	median value of the random variable
β	=	lognormal standard deviation of the variable

Therefore, only the median (θ_d) and the lognormal standard deviation (β_d) of the capacity of the structure to damage level d are needed to define the cumulative distribution function for the corresponding DS. The PGA value calculated using the procedure outlined above is taken to be θ_d, and it has been determined elsewhere ([33]) that an appropriate value for β_d is 0.6. Rewriting Equation 4.17 to reflect these yields the equation for vulnerability of the structure, V_{struct}:

$$\begin{aligned} V_{struct} &= P\left[D \geq DS | X = x\right] \\ &= \Phi\left(\frac{\ln(x/\theta_d)}{\beta_d}\right) \\ &= \Phi\left(\frac{\ln(x/PGA_{DS})}{0.6}\right) \end{aligned} \tag{4.18}$$

where D is defined as the level of damage reached during a given earthquake.

By calculating $P\left[D \leq d | X = x\right]$ for a range of values of x, a fragility curve can be constructed for a DS.

4.5.2 Hazard Curves

The uncertainty of site-specific demand can be quantified using the law of total probability. This allows for the calculation of the total probability of an event which depends on a number of events, each of which has a known probability of occurrence, of occurring. By

accounting for variables such as site soil conditions, distance from possible epicenters, and likely magnitudes of threatening earthquakes, the probability of exceedance of a given PGA can be estimated for a site in a given time frame. Equation 4.19 is an example of an exceedance frequency equation.

$$G(h) = \sum_{e=1}^{n_e} \sum_{a=1}^{n_A} \sum_{f=1}^{n_f(e)} \sum_{m} \sum_{o=1}^{n_o(f,m)} P\left[H > h | m, r, v, a\right] \cdot G\left(m, f, o | E = e\right) \cdot P\left[A = a\right] \cdot P\left[E = e\right] \tag{4.19}$$

where

$P[H > h\|m, r, v, a]$	=	the probability that more intense ground shaking than level h occurs, given an earthquake of magnitude m, site-to-source distance r, soil conditions v, while using ground motion prediction equation a
$G\left(m, f, o\|E = e\right)$	=	the frequency with which fault f ruptures at point o to produce an earthquake of magnitude m
$P[A = a]$	=	the probability that ground motion equation a accurately reflects reality of the shaking
$P[E = e]$	=	the probability that and earthquake with characteristics e occurs

The suite of USGS Hazard Tools includes the ability to produce hazard curves for locations throughout the United States. As with the site target spectrum used to select the suite of ground motions, the hazard curve used for the convolution integral was based on the geographic center of the sample bridges.

4.5.3 Vulnerability

A Risk Index, R, can be calculated by combining the fragility of the structure and hazard of the site. This is achieved by performing a convolution integral on the two curves, as in Equation 4.20 [16].

$$R = \int V_{struct} \cdot G(h) \;\; \mathrm{d}PGA \tag{4.20}$$

Chapter 5

RESULTS

5.1 Presentation of Results

Once DS PGAs were predicted using the scaling methods discussed in Chapter 4, NLTH analyses were run using appropriately scaled ground motions to determine the accuracy of the predictions. For bridges that had no DSs with equivalent SDOF damping ratios that exceeded 26%, the results of the unsmoothed scaling with limited damping are not reported, since they do not differ from the standard unsmoothed scaling. Graphs of pier displaced shapes were produced to visualize the spread of NLTH results, as well as qualitatively compare results. Error indices, as discussed in Chapter 4, were calculated for each DS.

The displacement plots for Bridge 1 are presented in full, as an example. All displacement plots for Bridges 2-7 can be found in Appendix A.

Fragility and risk curves for all bridges are presented here. Though the primary objective of this phase was to verify the prediction methods, risk rankings for all bridges, broken down by PL, are included at the end of the chapter.

5.2 Bridge 1

The DSs under consideration for Bridge 1 concerned the flexure and shear of the spill-through abutment (referred to as Pier 1), as well as flexure and shear of the free-standing pier (Pier 2). A total of seven DSs were achieved over the course of the pushover analysis, as outlined in Table 5.1.

Equivalent damping never exceeded $\xi_e = 26\%$, therefore there was no need to limit the damping factor used to scale the ground motions.

Table 5.1: Performance Levels and Damage States for Bridge 1

Performance Level	DS			Deck Displacement (m)	PGA (g)	
					Unsmoothed	Cardone
PL 1	1	d_y	Pier 1 Top	0.0273	0.388	0.366
	2	d_y	Pier 2 Top	0.0547	0.755	0.725
	3	d_y	Pier 1 Base	0.0628	0.858	0.812
	5	d_y	Pier 2 Base	0.121	1.306	1.095
PL 2	4	$d_{cr,v}$	Pier 1	0.107	1.214	1.010
PL 3	6	d_{vu}	Pier 1	0.162	1.452	1.285
PL 4	7	$1.1d_{vu}$	Pier 1	0.177	1.543	1.481

As can be seen in Table 5.2, for DSs 1 through 3, Cardone's scaling method produced displacements closer to those from the pushover analysis. At DSs 4 through 7, the unsmoothed scaling method proved more accurate. However, the predictions by both scaling methods were generally "Satisfactory."

Figures 5.1 – 5.7 show the displaced shapes of Pier 2 for each DS for the pushover and all NLTH analyses.

Table 5.2: Error indices for Bridge 1

Damage States	Unsmoothed	Cardone
DS 1	0.784	**0.831**
DS 2	0.831	**0.835**
DS 3	0.834	**0.874**
DS 4	**0.910**	1.175
DS 5	**0.936**	1.198
DS 6	**1.080**	1.276
DS 7	**1.091**	1.157

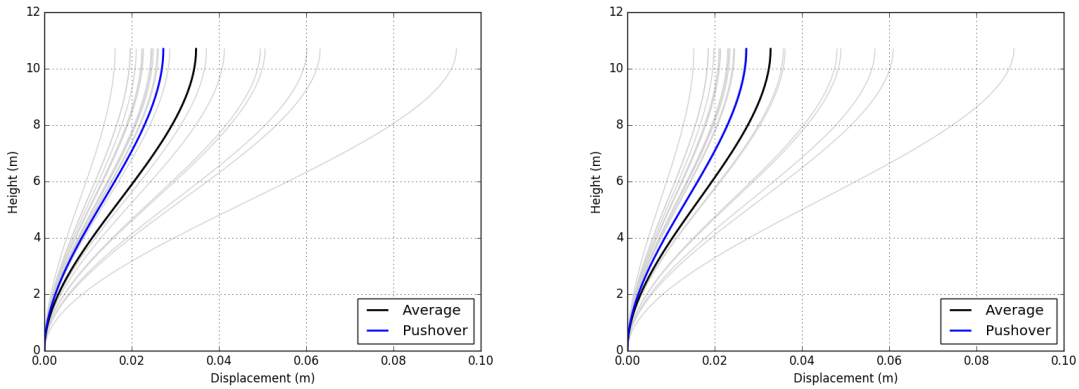

(a) (b)

Figure 5.1: Comparison of results for DS 1, scaling according to (a) the unsmoothed scaling method, and (b) Cardone's scaling method.

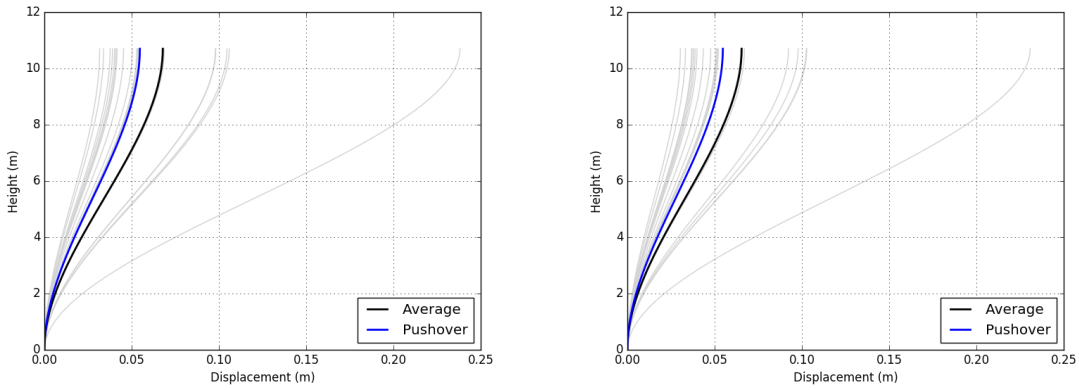

(a) (b)

Figure 5.2: Comparison of results for DS 2, scaling according to (a) the unsmoothed scaling method, and (b) Cardone's scaling method.

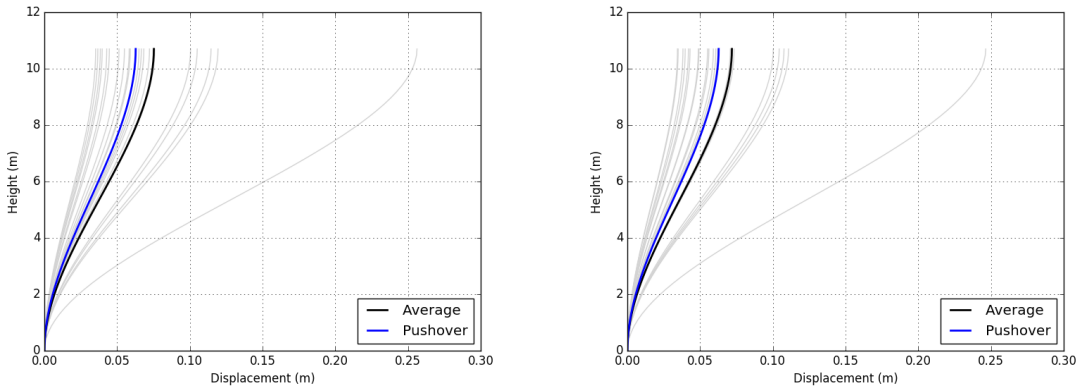

(a) (b)

Figure 5.3: Comparison of results for DS 3, scaling according to (a) the unsmoothed scaling method, and (b) Cardone's scaling method.

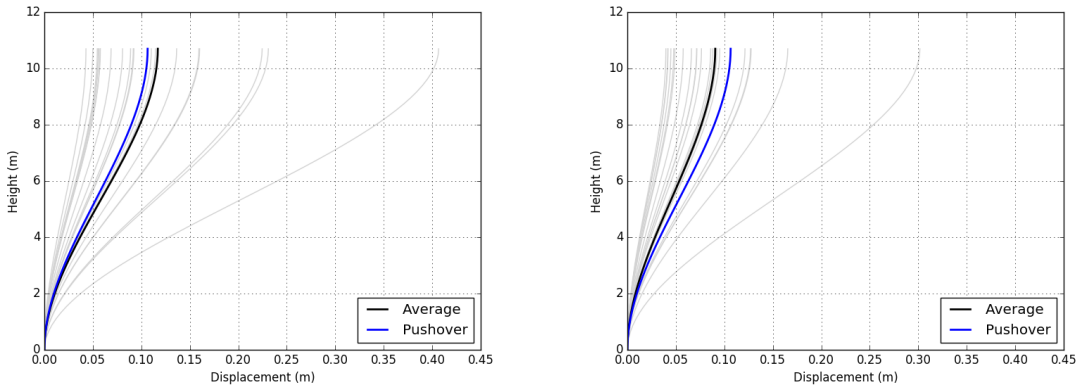

(a) (b)

Figure 5.4: Comparison of results for DS 4, scaling according to (a) the unsmoothed scaling method, and (b) Cardone's scaling method.

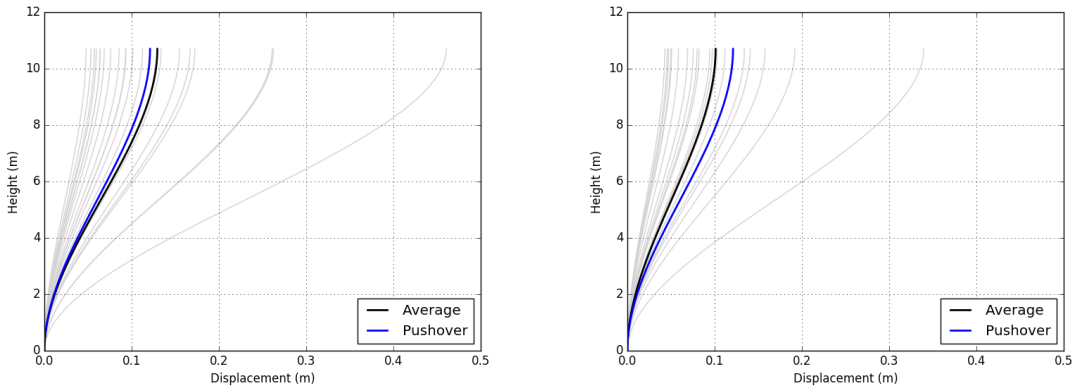

(a) (b)

Figure 5.5: Comparison of results for DS 5, scaling according to (a) the unsmoothed scaling method, and (b) Cardone's scaling method.

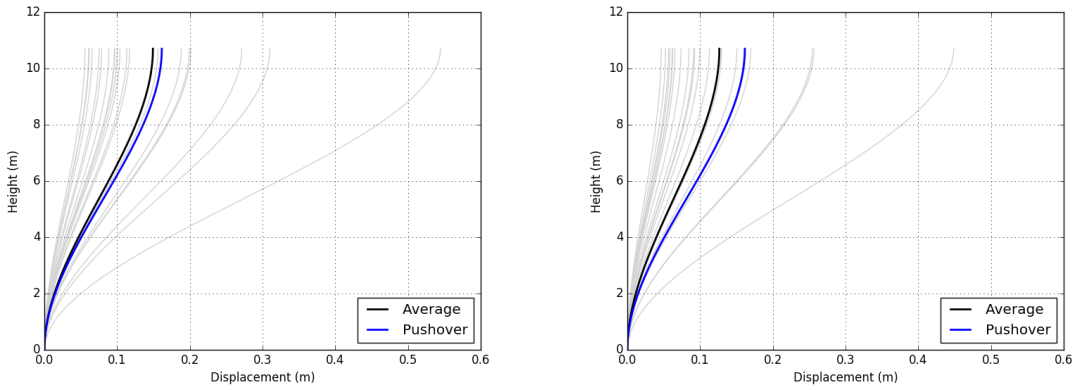

(a) (b)

Figure 5.6: Comparison of results for DS 6, scaling according to (a) the unsmoothed scaling method, and (b) Cardone's scaling method.

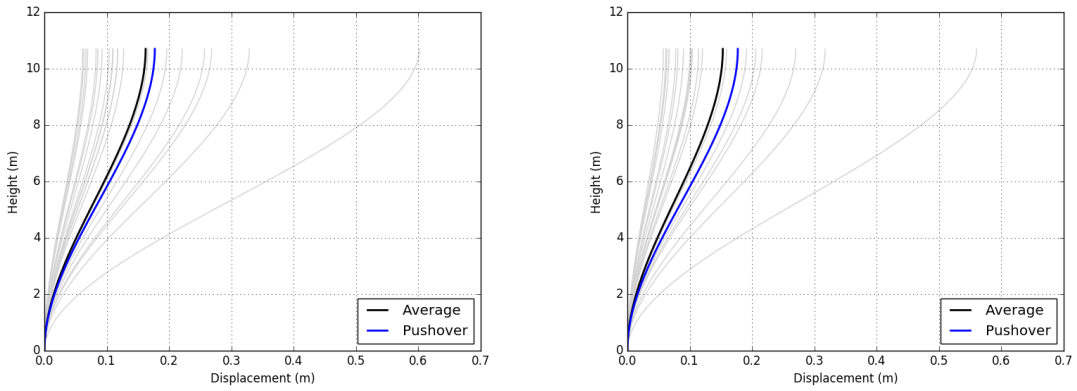

(a) (b)

Figure 5.7: Comparison of results for DS 7, scaling according to (a) the unsmoothed scaling method, and (b) Cardone's scaling method.

Figure 5.8 presents the fragility curves constructed for Bridge 1, with the two sets of curves representing the two scaling methods. As Cardone's scaling method generally predicted lower PGAs than the unsmoothed scaling method, it follows that the probability of achieving a given DS at a PGA is higher.

Figure 5.9 presents the results of the convolution integral of the fragility curves in Figure 5.8 and the site hazard curve. Cardone's scaling method yielded higher risk indices due to its prediction of achieving DSs at lower PGAs.

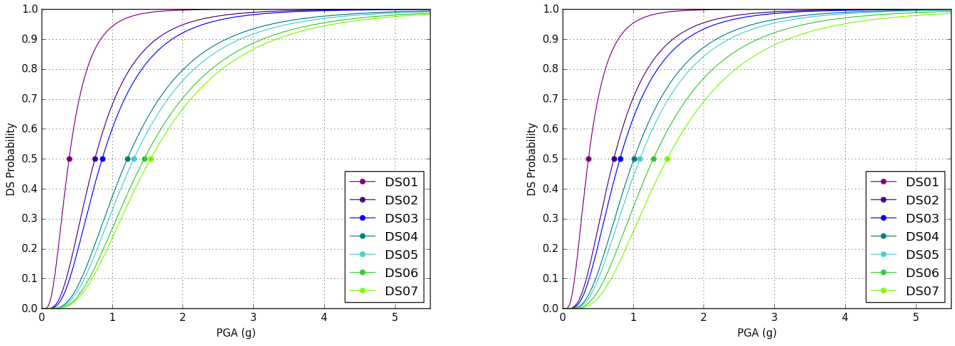

(a) (b)

Figure 5.8: Comparison of fragility curves constructed for Bridge 1, scaling according to (a) the unsmoothed scaling method, and the (b) Cardone's scaling method.

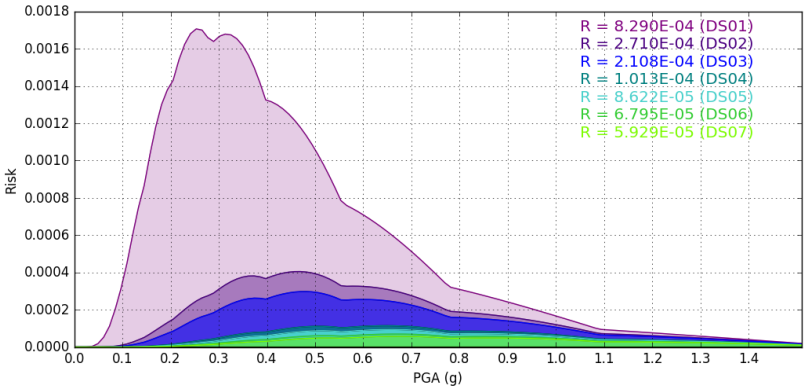

(a)

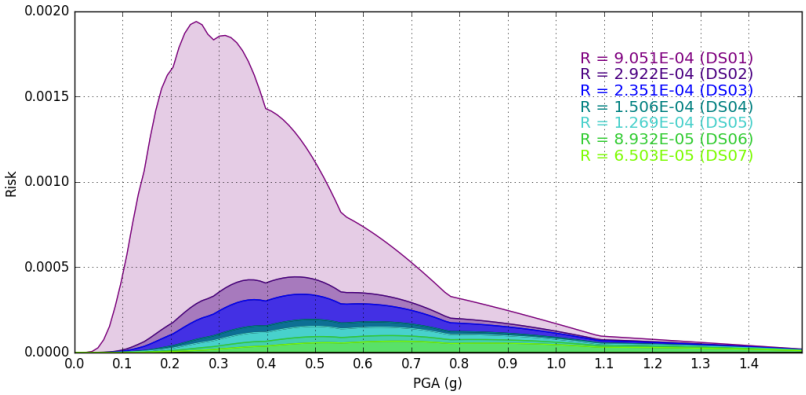

(b)

Figure 5.9: Comparison of risk curves constructed for Bridge 1, scaling according to (a) the unsmoothed scaling method, and the (b) Cardone's scaling method.

5.3 Bridge 2

For Bridge 2, the DSs of interest were associated with the shear and flexural behavior of the pier, as well as behavior of the steel roller bearings between Unit 2 and the other deck Units. A total of five DSs were achieved over the course of the pushover analysis, as outlined in Table 5.3.

Equivalent damping never exceeded $\xi_e = 26\%$, therefore there was no need to limit the equivalent damping used to scale the ground motions.

No DSs in PL4 were reached before instability occurred in the model during the pushover. This may be due to the large displacements possible after friction is overcome at the steel rollers causing instability.

Table 5.3: Performance Levels and Damage States for Bridge 2

Performance Level	DS			Deck Displacement (m)	PGA (g)	
					Unsmoothed	Cardone
PL 1	2	d_y	Pier	0.0956	0.478	0.416
PL 2	1	V_{pin}	Steel Roller	0.0652	0.363	0.284
	3	$d_{cr,v}$	Pier	0.123	0.791	0.611
	5	$d_y + \frac{d_u - d_y}{2}$	Pier	0.248	1.586	1.423
PL 3	4	V_{fr}	Steel Roller	0.205	1.417	1.194
PL 4	–	–	–	–	–	–

For all DSs for Bridge 2, Cardone's scaling method produced displacements closer to those predicted by the pushover analysis, as can be seen in Table 5.4. As with Bridge 1, the unsmoothed scaling method generally predicted higher PGAs than Cardone's scaling method. Both scaling methods were found to produce generally "Satisfactory" predictions.

Table 5.4: Error indices for Bridge 2

Damage States	Unsmoothed	Cardone
DS 1	0.815	**1.038**
DS 2	0.852	**1.053**
DS 3	0.794	**0.967**
DS 4	0.692	**0.870**
DS 5	0.720	**0.832**

Figure 5.10 presents the two sets of fragility curves constructed for Bridge 2. As with Bridge 1, the lower DS PGAs predicted using Cardone's scaling method leads to lower PGAs at which P $\approx$ 1.0 is achieved for DSs.

Figure 5.11 presents the results of the convolution integral of the fragility curves in Figure 5.10 and the site hazard curve. Cardone's scaling method yielded higher risk indices due to its prediction of achieving DSs at lower PGAs.

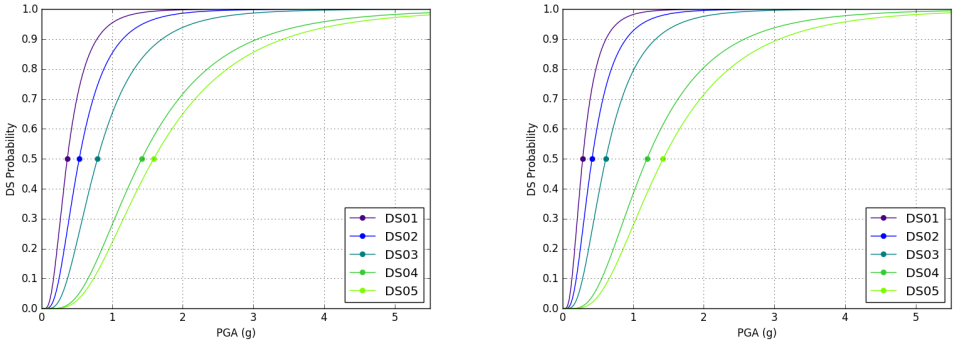

(a) (b)

Figure 5.10: Comparison of fragility curves constructed for Bridge 2, scaling according to (a) the unsmoothed scaling method, and the (b) Cardone's scaling method.

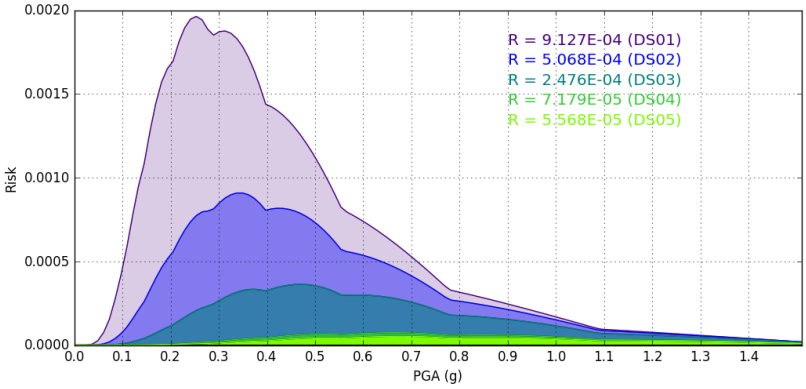

(a)

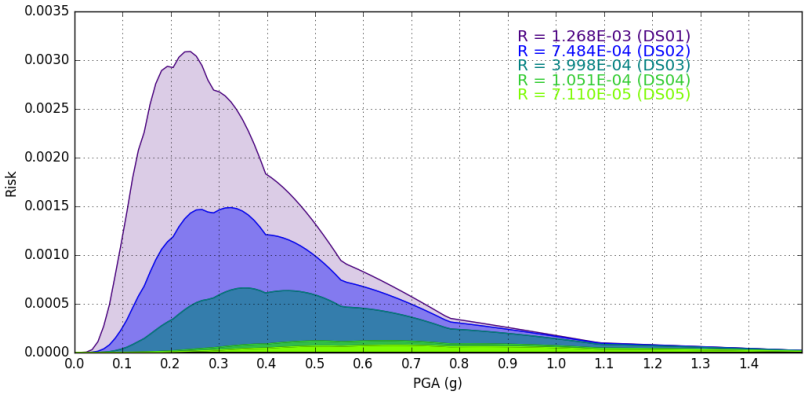

(b)

Figure 5.11: Comparison of risk curves constructed for Bridge 2, scaling according to (a) the unsmoothed scaling method, and the (b) Cardone's scaling method.

5.4 Bridge 3

The DSs of interest initially identified for Bridge 3 concerned the flexure and shear of the spill-through abutment (Pier 1), the free-standing pier (Pier 2), and the shear behavior of the abutment wingwall and elastomeric bearings. Pier 1, which is significantly shorter than Pier 2, reached 1.1 times its shear limit (PL 4) before any other element reached PL 1, as can be seen in Table 5.5. As such, only three DSs were analyzed.

Equivalent damping never exceeded $\xi_e = 26\%$, therefore there was no need to limit the equivalent damping used to scale the ground motions.

Table 5.5: Performance Levels and Damage States for Bridge 3

Performance Level	DS			Deck Displacement (m)	PGA (g)	
					Unsmoothed	Cardone
PL 1	–	–	–	–	–	–
PL 2	1	$d_{cr,v}$	Pier 1	0.0351	0.202	0.161
PL 3	2	d_{vu}	Pier 1	0.0518	0.294	0.228
PL 4	3	$1.1d_{vu}$	Pier 1	0.0557	0.312	0.234

Based on the error indices, both scaling methods were found to produce satisfactory results for all DSs for Bridge 3, as can be seen in Table 5.6.

Table 5.6: Error indices for Bridge 3

Damage States	Unsmoothed	Cardone
DS 1	0.874	**1.046**
DS 2	**0.916**	1.170
DS 3	**0.931**	1.231

Figure 5.12 presents the two sets of fragility curves constructed for Bridge 2. As with Bridges 1 and 2, the lower DS PGAs predicted using Cardone's scaling method leads to lower PGAs at which P $\approx$ 1.0 is achieved for DSs.

Figure 5.13 presents the results of the convolution integral of the fragility curves in Figure

5.12 and the site hazard curve. Cardone's scaling method yielded higher risk indices due to its prediction of achieving DSs at lower PGAs.

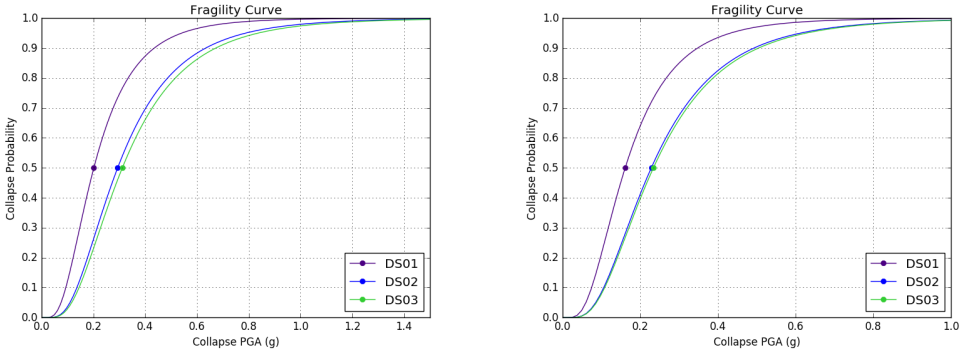

(a) (b)

Figure 5.12: Comparison of fragility curves constructed for Bridge 3, scaling according to (a) the unsmoothed scaling method, and the (b) Cardone's scaling method.

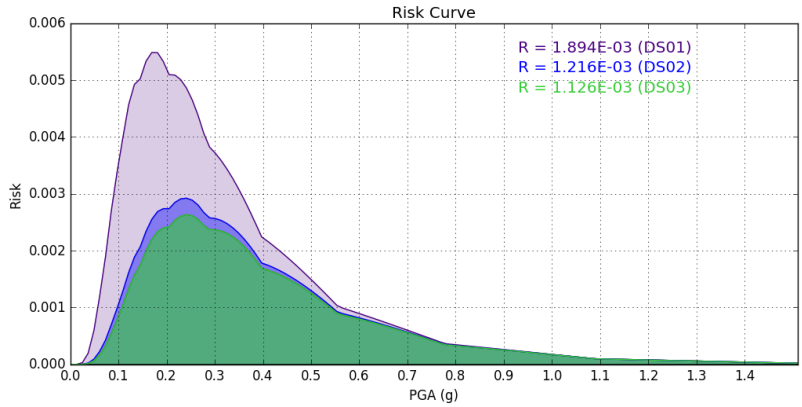

(a)

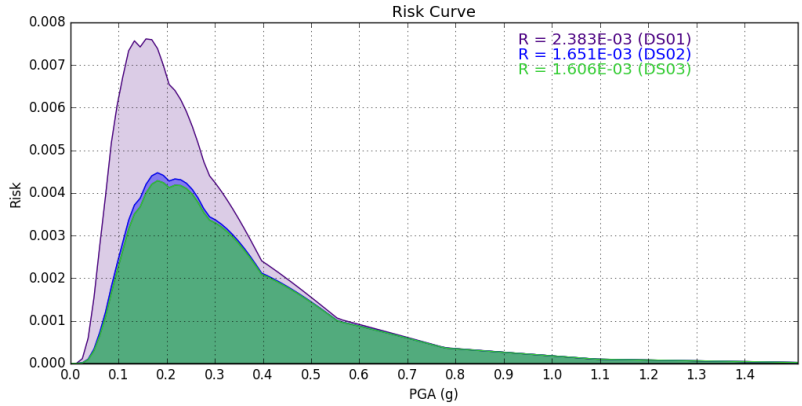

(b)

Figure 5.13: Comparison of risk curves constructed for Bridge 3, scaling according to (a) the unsmoothed scaling method, and the (b) Cardone's scaling method.

5.5 Bridge 4

The DSs of interest for Bridge 4 were the flexure and shear behavior of the pier, as well as the shear behavior of the abutment wingwall and elastomeric bearing. As shown in Table 5.7, though eight DSs were achieved, three occurred simultaneously, leading to the identification of six distinct DSs. Unlike Bridges 1-3, Cardone's scaling method did not consistently predict lower PGAs for DSs. For DSs 1 and 2, Cardone's method does predict lower PGAs, however, for DSs three through six, the unsmoothed scaling method predicts lower PGAs.

The equivalent damping for DSs 4 through 6 exceeded the $\xi_e = 26\%$ limit allowed by Car-

done's scaling method, so the results for the full equivalent damping, as well as the limited damping, were assessed using the unsmoothed method.

No DSs in PL4 were reached before instability occurred in the model during the pushover.

Table 5.7: Performance Levels and Damage States for Bridge 4

Performance Level	DS			Deck Displacement (m)	PGA (g)		
					Unsmoothed	Unsmoothed ($\xi \leq 26\%$)	Cardone
PL 1	2	d_y	Pier Top	0.0979	0.452	0.447	0.534
	3	d_{fr}	Bearing	0.136	0.551	0.551	0.658
	4	d_{roll}	Bearing Rollover	0.196	0.637	0.643	0.749
	5	d_y	Pier Base	0.239	0.680	0.702	0.925
PL 2	6	$d_{fr} + \frac{d_{pad} - dfr}{3}$	Bearing	0.320	0.988	1.137	1.382
	6	$\frac{d_{pad}}{2}$	Bearing	0.320	0.988	1.137	1.382
	6	$d_{cr,v}$	Pier	0.832	0.988	1.137	1.382
PL 3	1	V_{fr}	Wingwall	0.0167	0.098	0.098	0.076
PL 4	–	–	–	–	–	–	–

Ground motions scaled according to Cardone's method better matched the pushover results for all but the DS 1, as shown in Table 5.8. For this bridge, more advanced DSs were associated with poorer prediction accuracy. This is likely due to the inherent difficulty of predicting displacements of elastoplastic elements in the plastic region, such as the elastomeric bearings.

Table 5.8: Error indices for Bridge 4

Damage States	Unsmoothed	Unsmoothed ($\xi \leq 26\%$)	Cardone
DS 1	**0.925**	**0.925**	0.573
DS 2	1.260	1.274	**1.078**
DS 3	1.449	1.333	**1.202**
DS 4	1.804	1.786	**1.470**
DS 5	2.024	1.944	**1.306**
DS 6	4.110	3.327	**2.570**

Figure 5.14 presents the three sets of fragility curves constructed for Bridge 4.

Figure 5.15 presents the results of the convolution integral of the fragility curves in Figure 5.14 and the site hazard curve.

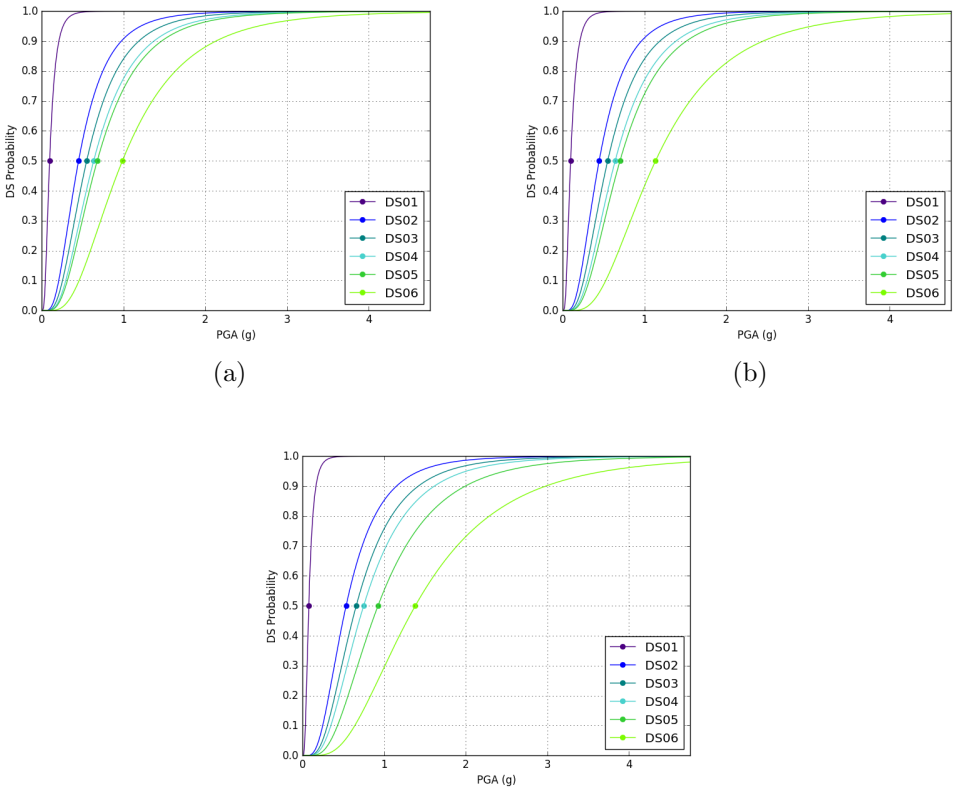

(a)

(b)

(c)

Figure 5.14: Comparison of fragility curves constructed for Bridge 4, scaling according to (a) the unsmoothed scaling method, (b) the unsmoothed scaling method with damping limited to $\xi \leq 26\%$ and the (c) Cardone's scaling method.

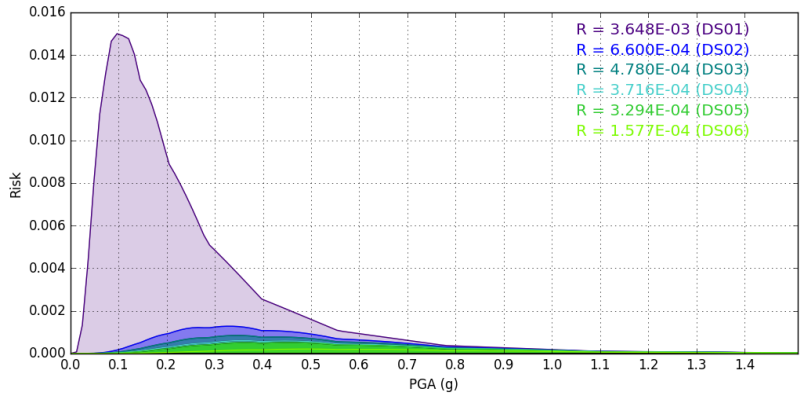

(a)

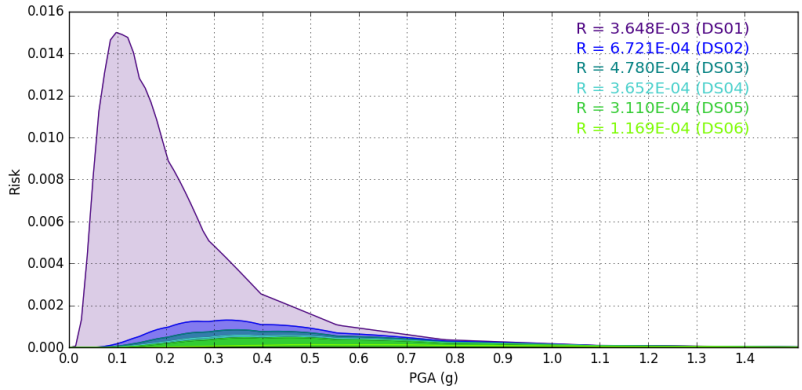

(b)

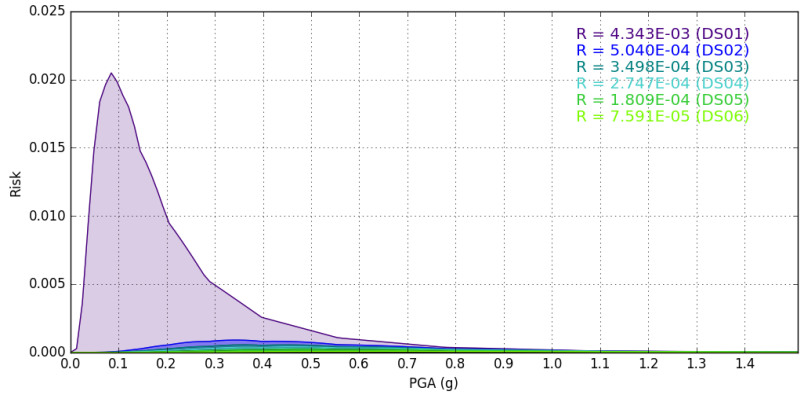

(c)

Figure 5.15: Comparison of risk curves constructed for Bridge 4, scaling according to (a) the unsmoothed scaling method, (b) the unsmoothed scaling method with damping limited to $\xi \leq 26\%$ and the (c) Cardone's scaling method.

5.6 Bridge 5

The DSs of interest for Bridge 5 were associated with the shear and flexural behavior of the spill-through abutment (Pier 1) and the free-standing pier (Pier 2). As outlined in Table 5.9, seven DSs were reached during the pushover analysis, but due to simultaneous occurance, four distinct DSs were investigated. Cardone's method predicted higher DS PGAs than the unsmoothed method for DSs 3 and 4.

Equivalent damping values exceeding the limit of $\xi_e = 26\%$ were not found for any DSs examined.

Table 5.9: Performance Levels and Damage States for Bridge 5

Performance Level	DS			Deck Displacement (m)	PGA (g)	
					Unsmoothed	Cardone
PL 1	1	d_y	Pier 1	0.0208	0.162	0.126
	2	d_y	Pier 2	0.0263	0.215	0.164
PL 2	3	$d_{cr,v}$	Pier 1	0.107	0.477	0.536
	4	$d_{cr,v}$	Pier 2	0.139	0.545	0.626
PL 3	3	d_{vu}	Pier 1	0.107	0.477	0.536
	4	d_{vu}	Pier 2	0.139	0.545	0.626
PL 4	4	$1.1d_{vu}$	Pier 1	0.139	0.545	0.626

As can be seen in Table 5.10, Cardone's method yielded NLTH displacements that more closely matched pushover displacements for DSs 1 and 2. However, for those DSs, neither scaling method produced very accurate results, though the cause is unclear. Both scaling methods proved "Satisfactory," or nearly so, for DSs 3 and 4.

Table 5.10: Error indices for Bridge 5

Damage States	Unsmoothed	Cardone
DS 1	0.463	**0.573**
DS 2	0.432	**0.624**
DS 3	**0.852**	0.774
DS 4	**1.008**	0.734

Figure 5.16 presents the two sets of fragility curves constructed for Bridge 5.

Figure 5.17 presents the results of the convolution integral of the fragility curves in Figure 5.16 and the site hazard curve.

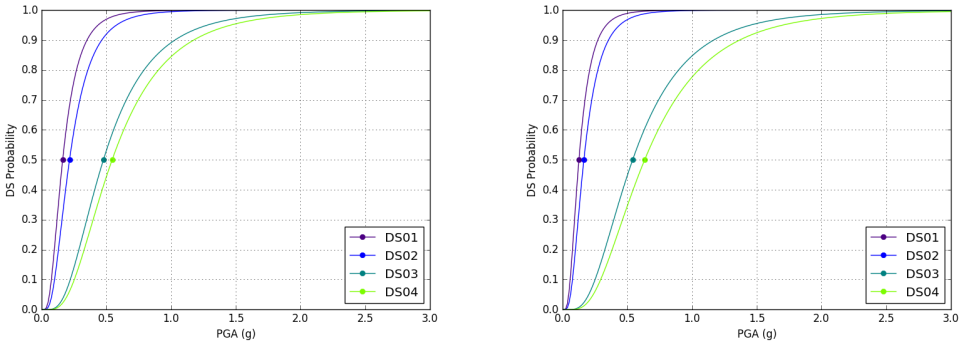

(a) (b)

Figure 5.16: Comparison of fragility curves constructed for Bridge 5, scaling according to (a) the unsmoothed scaling method, and (b) Cardone's scaling method.

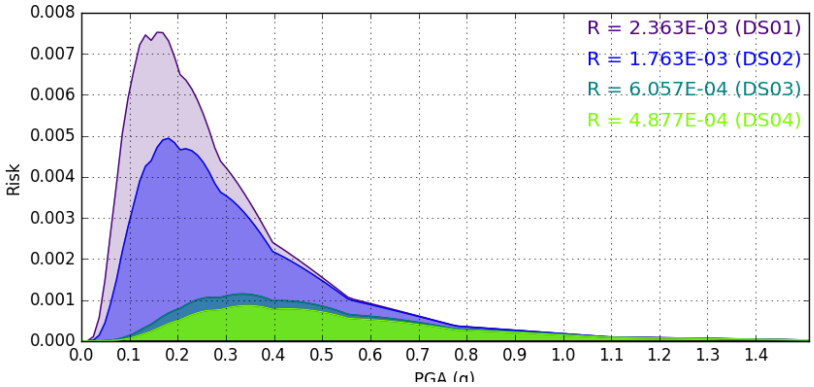

(a)

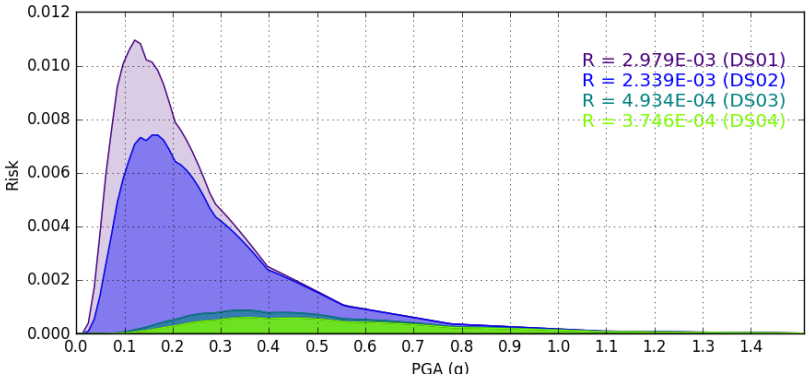

(b)

Figure 5.17: Comparison of risk curves constructed for Bridge 5, scaling according to (a) the unsmoothed scaling method, and (b) Cardone's scaling method.

5.7 Bridge 6

The DSs of interest for Bridge 6 were associated with the flexure and shear behavior of the pier, the shear behavior of the wingwall and pier stop blocks, and the shear behavior of the abutment and pier bearings. As shown in Table 5.11, nine distinct DSs were analyzed.

DSs 4 through 9 exceeded the equivalent damping limit of $\xi = 26\%$, so the unsmoothed scaling method was implemented for both the full calculated damping value and the limited damping for those DSs.

Table 5.11: Performance Levels and Damage States for Bridge 6

Performance Level	DS			Deck Displacement (m)	PGA (g)		
					Unsmoothed	Unsmoothed ($\xi \leq 26\%$)	Cardone
PL 1	1	F_{fr}	Abutment Bearing	0.0399	0.196	0.196	0.287
	2	d_{gap}	Pier	0.0418	0.208	0.208	0.284
	5	d_{gap}	Abutment	0.0508	1.501	1.441	1.697
	7	F_{fr}	Pier Bearing	0.0716	2.238	2.065	2.437
PL 2	3	$d_{cr,v}$	Pier	0.0465	0.830	0.830	0.818
	8	$d_{fr} + \frac{d_{pad} - d_{fr}}{3}$	All Bearings	0.196	2.990	2.676	2.533
PL 3	4	V_{fr}	Pier Stop Block	0.0496	1.503	1.431	1.689
	6	V_{fr}	Wingwall	0.0510	1.745	1.573	1.873
PL 4	9	d_{uns}	Pier Bearing	1.558	5.087	5.238	6.645

Displacement of the piers (Table 5.12) showed good agreement between the predicted and actual NLTH results. However, examination of the deck displacement was not as satisfactory overall (Table 5.13). This was likely due to the elastoplastic behavior of the elastomeric bearings, allowing for large displacements to occur in the bearing relative to the pier with little added force. As such, a force-based error index, calculated in a similar manner to the displacement error index (Table 5.14) was utilized as an alternative way to examine how well the NLTH results agreed with predictions.

Table 5.12: Top of pier displacement error indices for Bridge 6

Damage States	Unsmoothed	Unsmoothed ($\xi \leq 26\%$)	Cardone
DS 1	**0.974**	**0.974**	0.690
DS 2	**0.929**	**0.929**	0.726
DS 3	0.910	0.910	**0.913**
DS 4	1.109	1.109	**1.090**
DS 5	1.111	1.113	**1.092**
DS 6	**1.114**	1.134	1.116
DS 7	1.467	1.483	**1.439**
DS 8	**1.426**	1.427	1.447
DS 9	1.255	1.267	**1.197**

Table 5.13: Deck displacement error indices for Bridge 6

Damage States	Unsmoothed	Unsmoothed ($\xi \leq 26\%$)	Cardone
DS 1	**1.082**	**1.082**	0.854
DS 2	**1.089**	**1.089**	0.900
DS 3	0.443	0.443	**0.448**
DS 4	0.232	**0.248**	0.199
DS 5	0.2378	**0.252**	0.203
DS 6	0.195	**0.227**	0.177
DS 7	0.196	**0.218**	0.176
DS 8	0.361	0.423	0.453
DS 9	1.294	1.242	**0.912**

Table 5.14: Bearing force error indices for Bridge 6

Damage States	Unsmoothed	Unsmoothed ($\xi \leq 26\%$)	Cardone
DS 1	**1.078**	**1.078**	0.882
DS 2	1.090	1.090	**0.900**
DS 3	**0.683**	**0.683**	0.650
DS 4	**0.6511**	0.651	0.650
DS 5	**0.672**	0.672	0.671
DS 6	**0.670**	**0.670**	**0.670**
DS 7	**0.954**	**0.954**	**0.954**
DS 8	**1.000**	**1.000**	**1.000**
DS 9	**1.000**	**1.000**	**1.000**

Figure 5.18 presents the three sets of fragility curves constructed for Bridge 6.

Figure 5.19 presents the results of the convolution integral of the fragility curves in Figure 5.18 and the site hazard curve.

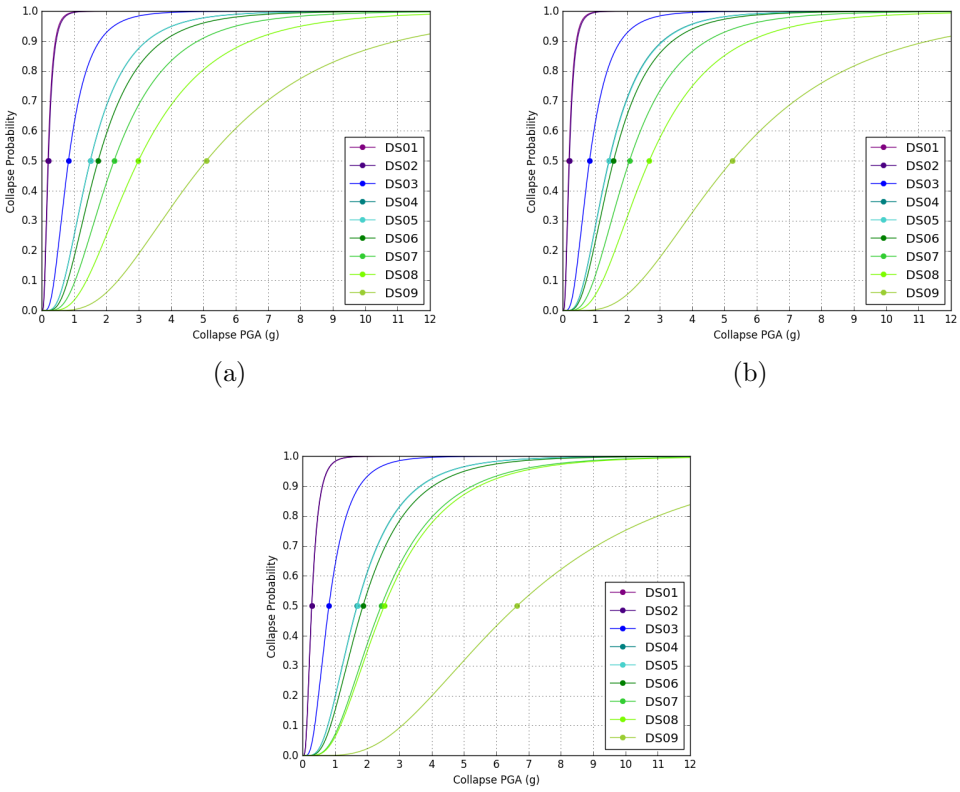

(a)

(b)

(c)

Figure 5.18: Comparison of fragility curves constructed for Bridge 6, scaling according to (a) the unsmoothed scaling method, (b) the unsmoothed scaling method with damping limited to $\xi \leq 26\%$ and the (c) Cardone's scaling method.

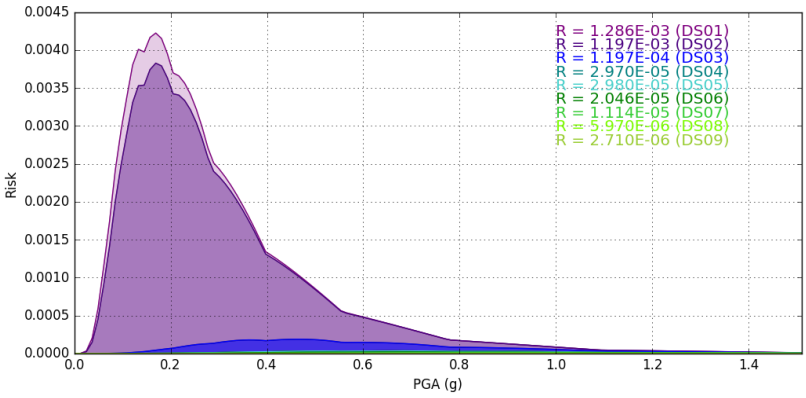

(a)

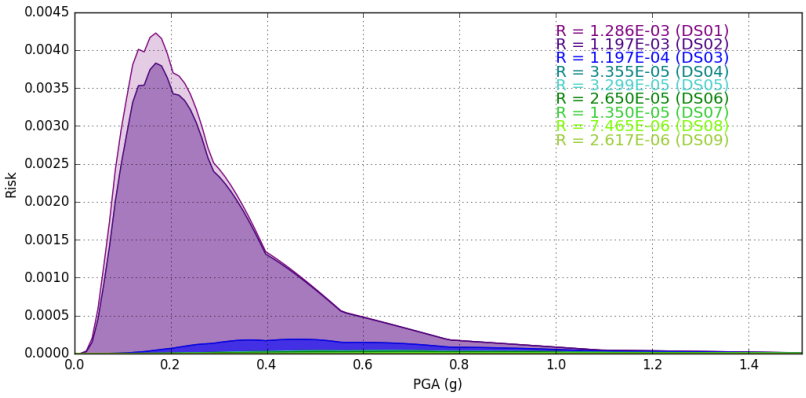

(b)

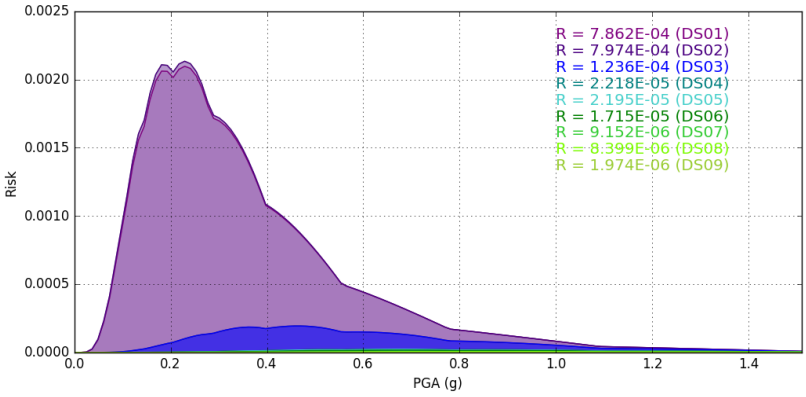

(c)

Figure 5.19: Comparison of risk curves constructed for Bridge 6, scaling according to (a) the unsmoothed scaling method, (b) the unsmoothed scaling method with damping limited to $\xi \leq 26\%$ and the (c) Cardone's scaling method.

5.8 Bridge 7

The DSs under consideration for Bridge 7 include flexure and shear of the pier as well as the resistance of the soil mass supporting the abutment. A total of three DSs were reached during analysis, as shown in Table 5.15. Cardone's scaling method predicted lower PGAs than the unsmoothed method for all DSs.

Equivalent damping values exceeding the limit of $\xi_e = 26\%$ were not found for any DSs examined.

Table 5.15: Performance Levels and Damage States for Bridge 7

Performance Level	DS			Deck Displacement (m)	PGA (g)	
					Unsmoothed	Cardone
PL 1	2	d_y	Pier	0.0534	0.404	0.327
PL 2	–	–	–	–	–	–
PL 3	1	d_u	Soil	0.0103	0.117	0.111
PL 4	3	d_u	Abutment	0.0610	0.629	0.596

Cardone's method produced more accurately scaled ground motions for all three DSs. However, neither scaling method yielded "Satisfactory" results for DSs 2 and 3, as seen in Table 5.16.

Table 5.16: Error indices for Bridge 7

Damage States	Unsmoothed	Cardone
DS 1	0.802	**0.926**
DS 2	1.976	**1.777**
DS 3	2.035	**1.597**

Figure 5.20 presents the three sets of fragility curves constructed for Bridge 7.

Figure 5.21 presents the results of the convolution integral of the fragility curves in Figure 5.20 and the site hazard curve.

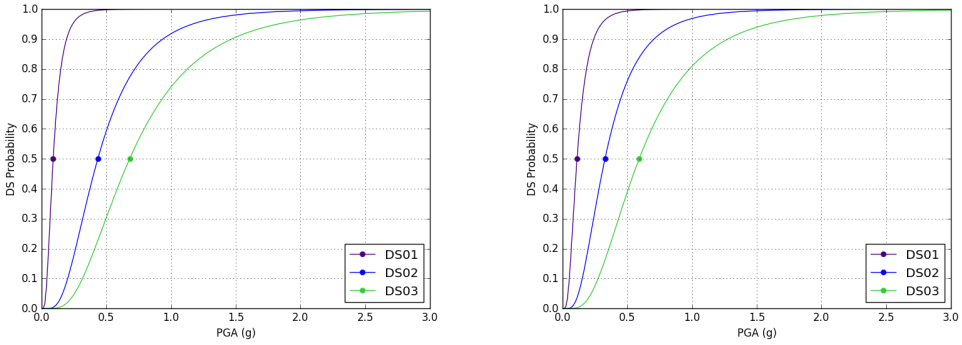

(a) (b)

Figure 5.20: Comparison of fragility curves constructed for Bridge 7, scaling according to (a) the unsmoothed scaling method, and (b) Cardone's scaling method.

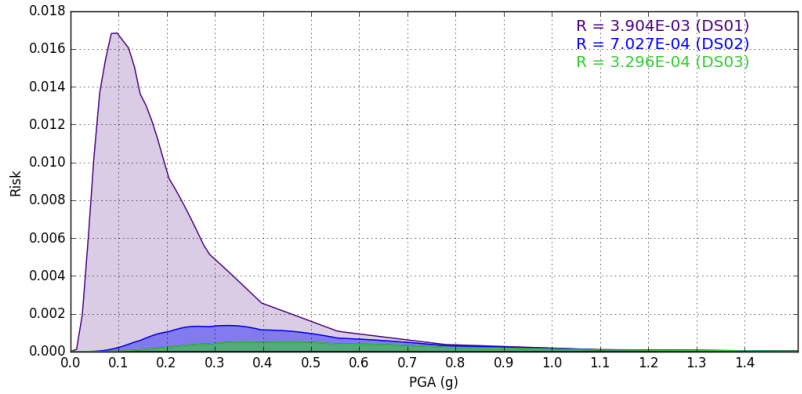

(a)

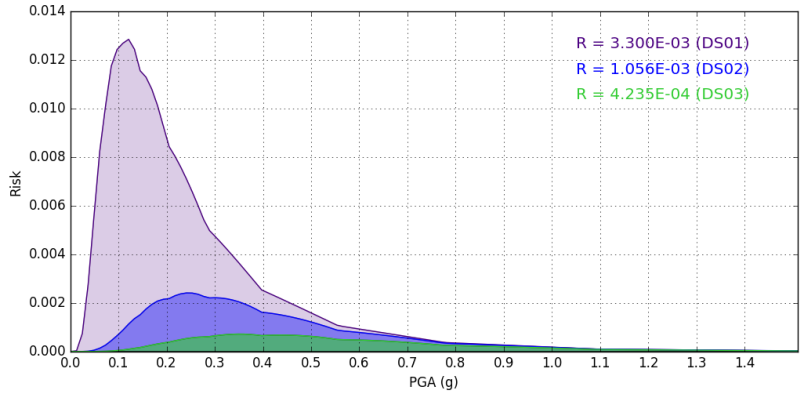

(b)

Figure 5.21: Comparison of risk curves constructed for Bridge 7, scaling according to (a) the unsmoothed scaling method, and (b) Cardone's scaling method.

5.9 Risk Ranking

In order to contextualize the results for individual bridges, they have been ranked according to their likelihood of reaching a given PL. Those bridges that did not reach a DS consistent with a given PL were exempted from ranking for that DS. Bridges are listed from most vulnerable to least vulnerable.

The different scaling methods produced generally consistent rankings between them. Due to some bridges reaching PLs out of order, it is unsurprising that no one bridge consistently placed as highly vulnerable or invulnerable across all four PLs.

Table 5.17: Risk Rankings

Performance Levels	Unsmoothed	Unsmoothed ($\xi \leq 26\%$)	Cardone
PL1	5	5	5
	6	6	7
	1	1	1
	7	7	6
	4	4	2
	2	2	4
PL2	3	3	3
	2	2	2
	5	5	5
	4	6	1
	6	4	6
	1	1	4
PL3	7	7	4
	4	4	7
	3	3	3
	5	5	5
	2	2	2
	1	1	1
	6	6	6
PL4	3	3	3
	5	5	7
	7	7	5
	1	1	1
	6	6	6

Chapter 6

CONCLUSIONS

The primary objectives of this project were to verify the reliability of using Cardone's analysis framework to predict dynamic response of reinforced concrete bridges and to use the results of that analysis to quantify seismic vulnerability. An established PGA prediction method using a smoothed site target spectrum, presented by Cardone ([14], [15]), was compared against a scaling method using the average of a suite of unsmoothed ground motion spectra. Ultimately, the results were combined with a site hazard curve to calculate a Risk Index.

6.1 Accuracy of Predictions

6.1.1 Comparing Predictions

The most obvious measure of utility of a scaling method is accuracy of predictions. As can be seen in Figure 6.1, the majority of PGA predictions (62% for each scaling method) were considered "Satisfactory" (definitions of qualification of error are presented in Chapter 4). Cardone's scaling method produced the lowest number of "Poor" predictions (2.7%). All scaling methods produced either "Satisfactory" or "Moderate" results for more than 85% of DSs.

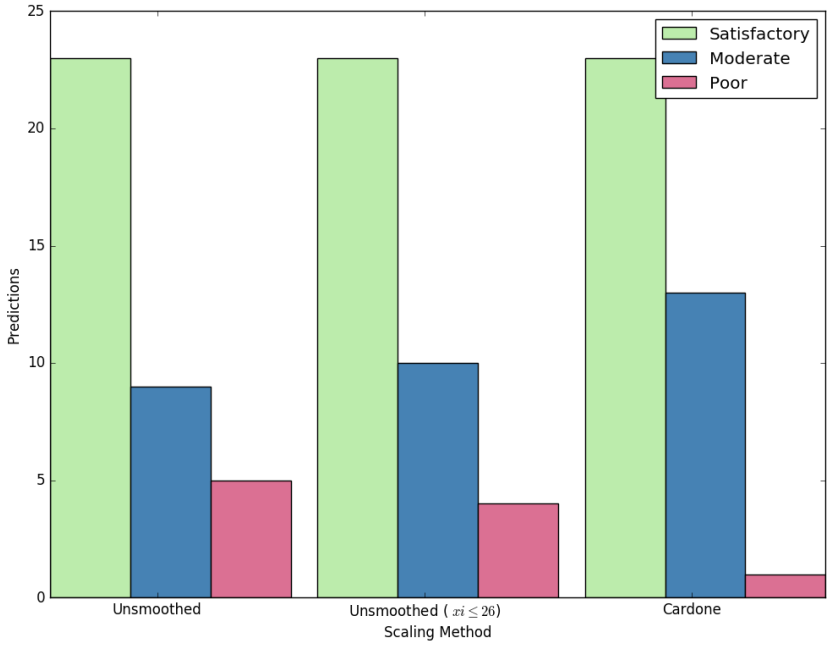

Figure 6.1: Breakdown of share of good, moderate and poor predictions

Accuracy is not the only measure of usability of the prediction methods. If predictions are "Satisfactory," but predict attainment of a DS at a higher PGA than reality, there's risk of underestimating the vulnerability of a bridge. As such, examining the frequency with which the scaling methods yielded conservative and non-conservative predictions is also useful. Figure 6.2 shows that while both unsmoothed scaling methods produced "Conservative" predictions for nearly half of the DSs (43%), Cardone's scaling method yielded conservative predictions for more than half of DSs (60%).

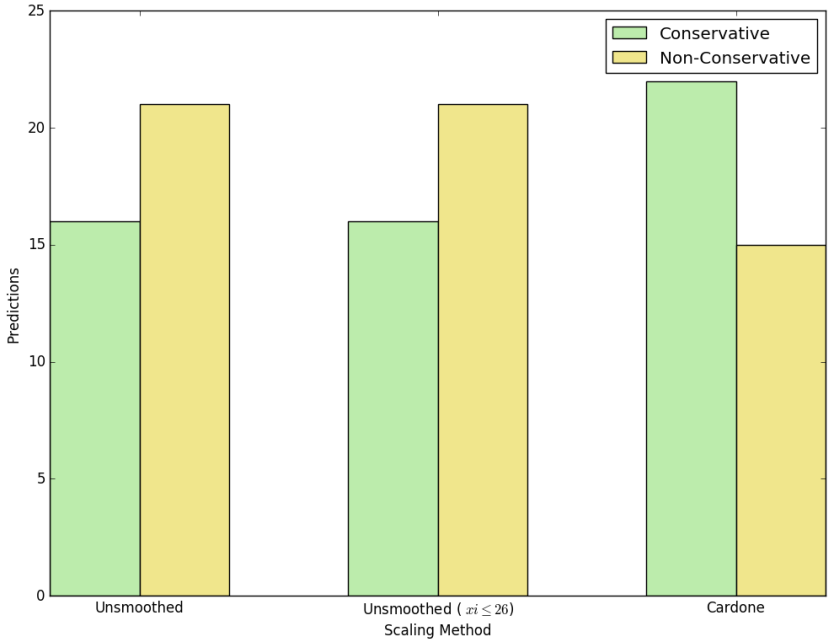

Figure 6.2: Breakdown of share of conservative and non-conservative predictions

Determining if there is a systematic cause of inaccurate predictions is instructive as well. Examining which bridges were more prone to inaccurate predictions, as seen in Figures 6.3 and 6.4, we see that Bridges 4 and 6 accounted for the greatest number of "Poor" predictions. This is most likely due to the behavior of the elastomeric bearings in those two bridges.

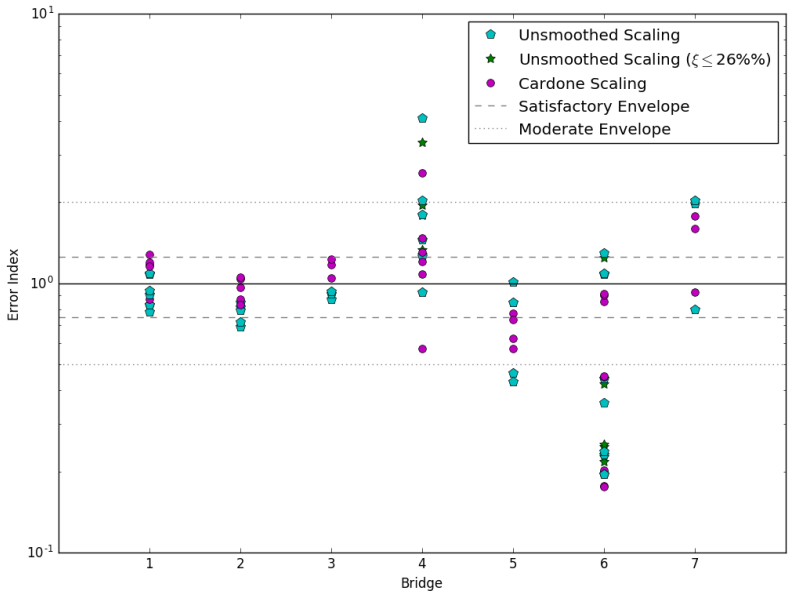

Figure 6.3: Distribution of err_i values for deck displacement for all DSs, broken down by bridge.

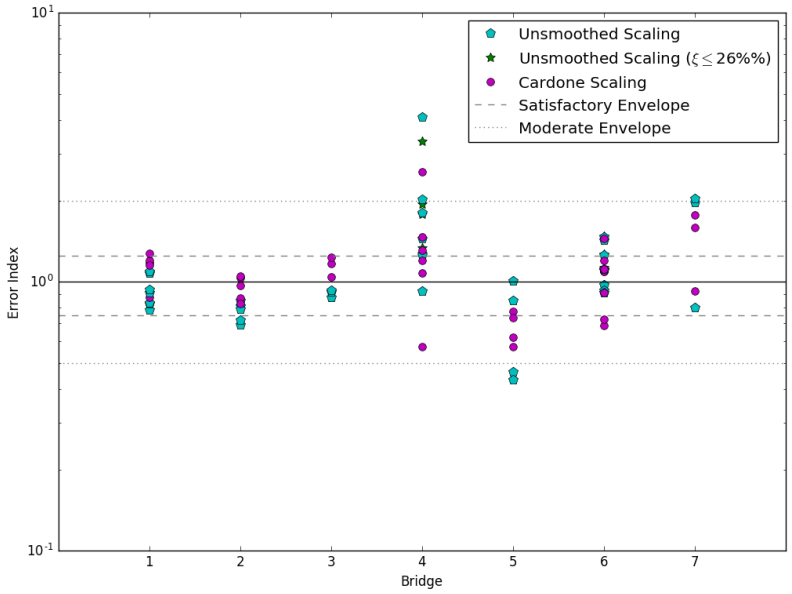

Figure 6.4: Distribution of err_i values for top of pier displacement for all DSs, broken down by bridge. Bridge 6 is the only bridge for which deck displacement was not synonymous with top of pier displacement.

However, when considering only the prediction for first reaching a given Performance Level, it is shown in Figure 6.5 that a large share (71%) of all predictions are "Satisfactory" or "Moderate." The most notable exceptions are in PL2, which correspond to the "Poor" prediction for Bridge 4 reaching DS6. Predictions of when a bridge would reach PL3 were particularly accurate, which is important due to the fact PL3 is the most extreme performance level considered when determining design objectives.

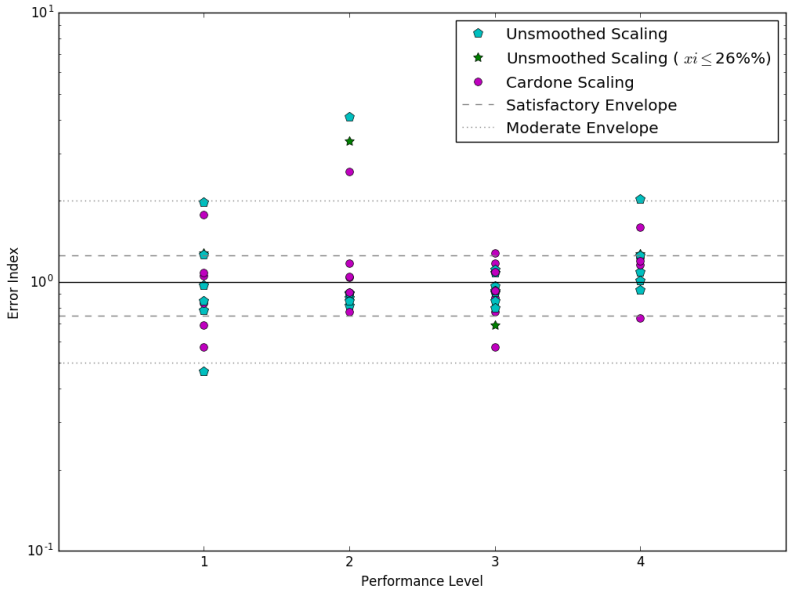

Figure 6.5: Distribution of err_i values for top of pier displacement for DSs corresponding to a bridge reaching a PL for the first time.

Taking all comparisons into consideration, it is clear that the prediction methods yielded overall reasonable results. Cardone's method was most reliably accurate and conservative in its predictions. An additional advantage of Cardone's method is that it does not require the user to curate a collection of ground motions in order to predict the PGAs. For these reasons, it is recommended that Cardone's method be utilized as originally conceived.

6.1.2 Utility of the Analysis Method

Overall, the analysis method used in this project proved to be reasonably accurate in predicting the PGAs at which DSs would be reached by the study bridges. Construction of fragility curves and convolution with the site hazard curve proved to be a straightforward method of quantifying risk, providing a convenient way to rank vulnerability of bridges with respect to one another.

6.2 Limitations of Work

As this work is the first step in a larger project, there are obvious limitations to the conclusions drawn.

The first is the small sample size. While efforts were taken to select "Representative" bridges, it is difficult to distill thousands of distinct structures into a handful of samples. Though results were encouraging for the most part, more samples will be needed to draw definitive conclusions.

Perhaps the biggest limitation is in the simplification of the models. All properties were drawn directly from real bridges and utilized as realistically as possible in a few elements as possible while making some assumptions, discussed in Chapter 3. However, direct comparison with results from more comprehensive models was not conducted. That said, predictions of DS PGAs seem reasonable when compared to Cardone's work [14, 15]

Looking at the bridges with the highest number of "Poor" predictions, one can see that they are the bridges with elastomeric bearings. A number of theories exist of how elastomeric bearings should be modeled, and the model chosen for this project is highly simplistic. Use of a more realistic model may produce better results for bridges that include elastomeric bearings.

6.3 Further Work

This project is intended as the first phase in developing software to perform the analysis verified in this project. Prior to full development of the software, intermediate steps are recommended. The first is testing of a larger sample set of bridges, with focus on including bridges with less "typical" properties. Demonstrating the wide-ranging applicability of the analysis method may be beneficial to acceptance as a tool. A second recommended intermediate step is the development of a bridge database framework for collecting structural properties. Many bridge plans are vague in presenting specified structural properties, such as concrete and rebar strengths, and having a database including bridges of similar design and vintage would allow users of the software to draw from those similar bridges in order to fill in the blanks.

The groundwork for software has already been laid in the course of this phase of the project. The basics of a sectional analysis program similar to CUMBIA have been written using the Python programming language. The Python scripts used to illustrate structure displaced shapes, create fragility curves, and calculate the convolution of the fragility curves with the hazard curve can easily be adapted to work together as part of a larger piece of software. The most significant developments required for creation of the final software package are the integration of pushover analysis and the determination of how the balance between human judgment and automation might be struck in the determination of DSs and equivalent SDOF properties, then implementation of that balance.

Creation of a software package that can aid in determination and ranking of bridge vulnerability could improve asset management. Pursuing this goal is important in developing new seismic design philosophy in a proactive, rather than reactive, way.

BIBLIOGRAPHY

[1] John Adams. Paleoseismology: A Search for Ancient Earthquakes in Puget Sound. *Science*, 258(5088):1592–1593.

[2] American Association of State Highway and Transportation Officials, Washington, D.C. *AASHTO LRFD Bridge Design Specifications*, 6 edition, 2012.

[3] T. D. Ancheta, R. B. Darragh, J. P. Stewart, E. Seyhan, W. J. Silva, B. S. J. Chiou, K.E. Woodell, R.W. Graves, A.R. Kottke, Boore D.M., T Kishida, and J. L. Donahue. NGA-West2 Database. *Earthquake Spectra*, 30(3):989–1005, Aug 2014.

[4] S. Antoniou and R. Pinho. Development and Verification of a Displacement-Based Adaptive Pushover Procedure. *Journal of Earthquake Engineering*, 2004.

[5] Mark A. Aschheim. Northridge Collection, 1994.

[6] Brian F Atwater. Evidence for Great Holocene Earthquakes along the Outer Coast of Washington State. *Science*, 236(4804):942–944, 1987.

[7] Brian F. Atwater, Satoko Musumi-Rokkaku, Kenji Satake, Yoshinobu Tsuji, Kazue Ueda, and David K. Yamaguchi. The Orphan Tsunami of 1700: Japanese Clues to a Parent Earthquake in North America. Technical report, 2005.

[8] Khossrow Babaei and Neil M. Hawking. Bridge Seismic Retrofit Planning Program. Technical report, Washington State Department of Transportation, Olympia, 1991.

[9] D Ballantyne, M Pierepiekarz, and S Chang. Seismic Vulnerability Assessment of the Seattle-Tacoma Highway Corridor Using HAZUS. In *Proceedings of the Third National Seismic Conference & Workshop on Bridges & Highways*, pages 237–248, Federal Way, 2002.

[10] Martin Bimschas. *Displacement Based Seismic Assessment of Existing Bridges in Regions of Moderate Seismicity*. Swiss Federal Institute of Technology, Zurich, 2010.

[11] Michel Bruneau, Myrto Anagnostopoulou, and Alessandro Palermo. Preliminary Report on Bridge Damage from the Darfield (New Zealand) M7.1 earthquake of September 4, 2010. Technical report, Earthquake Engineering Research Institute, Christchurch, 2010.

[12] BS EN 1998-1. *Eurocode 8: Design of structures for earthquake resistance - Part 1 : General rules, seismic actions and rules for buildings*. 2004.

[13] Caltrans Seismic Advisory Board. The Race to Seismic Safety. Technical report, California Department of Transportation, 2003.

[14] D Cardone, V Capone, G Perrone, and L Petrini. Direct Displacement-Based Seismic Assessment of Multi-Span Simply Supported Deck Bridges. In M. Papadrakakis, M. Fragiadakis, and V. Plevris, editors, *ECCOMAS Thematic Conference on Computational Methods in Structural Dynamics and Earthquake Engineering*, Corfu, 2011. European Congress on Computational Methods in Applied Sciences and Engineering.

[15] Donatello Cardone. Displacement Limits and Performance Displacement Profiles in Support of Direct Displacement-Based Seismic Assessment of Bridges. *Earthquake Engineering & Structural Dynamics*, 43(8):1239–1263, jul 2014.

[16] Donatello Cardone, Giuseppe Perrone, and Salvatore Sofia. A performance-based adaptive methodology for the seismic evaluation of multi-span simply supported deck bridges. *Bulletin of Earthquake Engineering*, 2011.

[17] Athol J. Carr. *Ruaumoko*. University of Canterbury Department of Civil Engineering, Christchurch, 2004.

[18] M. Celebi. January 17, 1994 Northridge USA Earthquake, 1994.

[19] Wai-Fah Chen and Lian Duan. *Bridge engineering handbook. Seismic design*. Taylor & Francis Group, LLC, Boca Raton, 2nd edition, 2014.

[20] K Emori and WC Schnobrich. Analysis of reinforced concrete frame-wall structures for strong motion earthquakes, Structural Research Series No. 434. *Civil Engineering Studies, University of Illinois at Urbana-Champaign*, 1978.

[21] Federal Highway Administration. Recording and Coding Guide for the Structure Inventory and Appraisal of the Nation's Bridges. Technical report, US Department of Transportation, Washington, D.C., 1995.

[22] Federal Highway Administration. LRFD Seismic Analysis and Design of Bridges Reference Manual. Technical report, US Department of Transportation, Washington, D.C., 2014.

[23] Federal Highway Administration. National Bridge Inventory, 2016. data retrieved from Federal Highway Administration.

[24] L.S. Gee and W.S. Leith. The Global Seismographic Network, 2013.

[25] Melbourne F. Giberson. Two Nonlinear Beams with Definitions of Ductility. *Journal of the Structural Division*, 95(2):137 – 157, Feb 1969.

[26] David J Harding and Gregory S Berghoff. Fault Scarp Detection Beneath Dense Vegetation Cover: Airborne LiDAR Mapping of the Seattle Fault Zone, Bainbridge Island, Washington State. In *Proceedings of the American Society of Photogrammetry and Remote Sensing Annual Conference*, Washington, D.C., 2000. American Society of Photogrammetry and Remote Sensing.

[27] Lydik Jacobsen. Steady Forced Vibrations as Influenced by Damping. *Transactions of the American Society of Mechanical Engineers*, 1930.

[28] Constatine Karantzikis, Michael an Spyrakos. Seismic Analysis of Bridges Including Soil-Abutment Interaction. In *12th World Conference on Earthquake Engineering*, Aukland, 2000. New Zealand Society for Earthquake Engineering.

[29] Mervyn J. Kowalsky. A Displacement-Based Approach for the Seismic Sesign of Continuous Concrete Bridges. *Earthquake Engineering and Structural Dynamics*, 31(3):719–747, 2002.

[30] David J. Lee. *Bridge Bearings and Expansion Joints.* E & FN Spon, London, 2nd edition, 1994.

[31] Abraham C. Lynn. Northridge Collection, 1994.

[32] J B Mander, M J N Priestley, and R Park. Theoretical Stree-Strain Model for Confined Concrete. *Journal of Structural Engineering*, 114(8):1804–1826, 1988.

[33] John Mander. Fragility Curve Development for Assessing the Seismic Vulnerability of Highway Bridges. Technical report, Multidisciplinary Center for Earthquake Engineering Research, Buffalo, 1999.

[34] El-Sayed Mashaly, Mohamed El-Heweity, Hamdy Abou-Elfath, and Mostafa Ramadan. A new beam-column model for seismic analysis of RC frames Part I: Model derivation. *Alexandria Engineering Journal*, 50(4):313–320, 2011.

[35] Sami Hanna Megally, Silva F. Perdo, and Frieder Seible. Structural Systems Research Project Seismic Response of Sacrificial Shear Keys in Bridge Abutments. Technical report, California Department of Transportation, Sacramento, 2002.

[36] Denis Mitchell, Michel Bruneau, Murat Saatcioglu, Martin Williams, Donald Anderson, and Robert Sexsmith. Performance of Bridges in the 1994 Northridge Earthquake. *Canadian Journal of Civil Engineering*, 22(2):415–427, apr 1995.

[37] Richard Monastersky. Large Prehistoric Earthquake Ripped Seattle. *Science News*, pages 388–389, 1992.

[38] Luis A. Montejo and Mervyn J. Kowalsky. CUMBIA. Technical report, North Caronlina State University Department of Civil, Construction, and Environmental Engineering, Raleigh, 2007.

[39] Washington Office of Financial Management. Population Density by Census Block: 2010.

[40] Shunsuke Otani. SAKE: A Computer Program for Inelastic Response of R/C Frames to Earthquakes. Technical report, The National Science Foundation, 1974.

[41] Pacific Northwest Seismic Network. Crustal Faults.

[42] Pacific Northwest Seismic Network. Deep Earthquakes.

[43] D Pennucci, G M Calvi, and T J Sullivan. Displacement-Based Design of Precast Walls with Additional Dampers. *Journal of Earthquake Engineering*, 2009.

[44] W F Pond. Performance of Bridges During San Fernando Earthquake. *PCI Journal*, (July-August):65–75, 1972.

[45] Keith Porter. A Beginner's Guide to Fragility, Vulnerability, and Risk. Technical report, University of Colorado Boulder, Boulder, 2016.

[46] M.J.N Priestley, F. Seible, and G.M. Calvi. *Seismic Design and Retrofit of Bridges*. John Wiley & Sons, Inc., New York, 1996.

[47] Nigel Priestley, Frieder Seible, Yan Xiao, and Ravindra Verma. Steel Jacket Retrofitting of Reinforced Concrete Bridge Columns for Enhanced Shear Strength – Part 1: Theoretical Considerations and Test Design. *Journal of Structural Engineering*, 91(4):394 – 405, Jul 1994.

[48] Dan J. Raynor, Dawn E. Lehman, and John F. Stanton. Bond-Slip Response of Reinforcing Bars Grouted in Ducts. *ACI Structural Journal*, 99(5), 2002.

[49] Sandra S. Schulz and Robert E. Wallace. The San Andreas Fault, 2016.

[50] Kathryn Shulz. The Really Big One. *The New Yorker*, July 2015.

[51] Eleni Smyrou, M. J Nigel Priestley, and Athol J. Carr. Modelling of elastic damping in nonlinear time-history analyses of cantilever RC walls. *Bulletin of Earthquake Engineering*, 2011.

[52] C.W. Stover and J.L. Coffman. Seismiscity of the United States, 1568-1989. Technical report, US Geological Survey, Washington, D.C., 1993.

[53] US Geological Survey. Washington.

[54] US Geological Survey. 1964 Great Alaska Earthquake Damage Photos, 2016.

[55] Christopher R. Thewalt. Kobe Bridge Collection, 1995.

[56] Diana Todd, Nicolas J. Carino, Riley M. Chung, Hai S. Lew, Andrew W. Taylor, William D. Walton, James D. Cooper, and Roland Nimis. 1994 Northridge Earthquake: Performance of Structures, Lifelines and Fire Protection Systems (NIST SP 862). Technical report, National Institute of Standards and Technology, Washington, D.C., 1994.

[57] US Geological Survey. Understanding Plate Motions, 2014.

[58] US Geological Survey. Earthquake Facts and Earthquake Fantasy, 2016.

[59] US Geological Survey. Earthquake Glossary, 2016.

[60] Washington State Department of Transportation. Seismic Lifeline Routes. Technical report, Washington State Department of Transportation, Olympia, 2015.

[61] Washington State Department of Transportation. Bridges – By the Numbers, 2016.

[62] Washington State DNR. Earthquakes and Faults, 2016.

[63] Wisconsin Department of Transportation, Madison. *WisDOT Bridge Manual*, 2017.

[64] T.L. Youd, K.M. Rollins, A.F. Salazar, and R.M. Wallace. Bridge Damage Caused by Liquefaction During the 22 April 1991 Costa Rica Earthquake. In *Proceedings of the 10th World Conference on Earthquake Engineering*, pages 153–158, Madrid, 1992. International Association of Earthquake Engineering.

Appendix A

DISPLACEMENT PLOTS FOR BRIDGES 2-7

A.1 Bridge 2

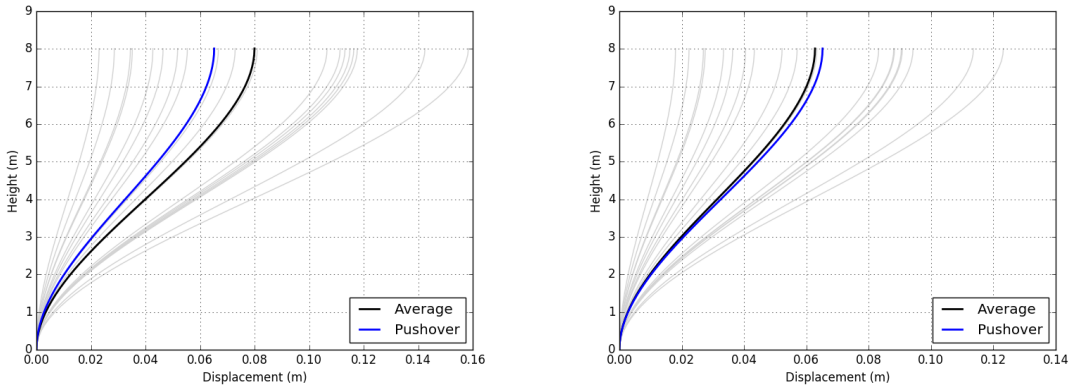

(a) (b)

Figure A.1: Comparison of results for DS1, scaling according to (a) the unsmoothed scaling method, and the (b) Cardone's scaling method.

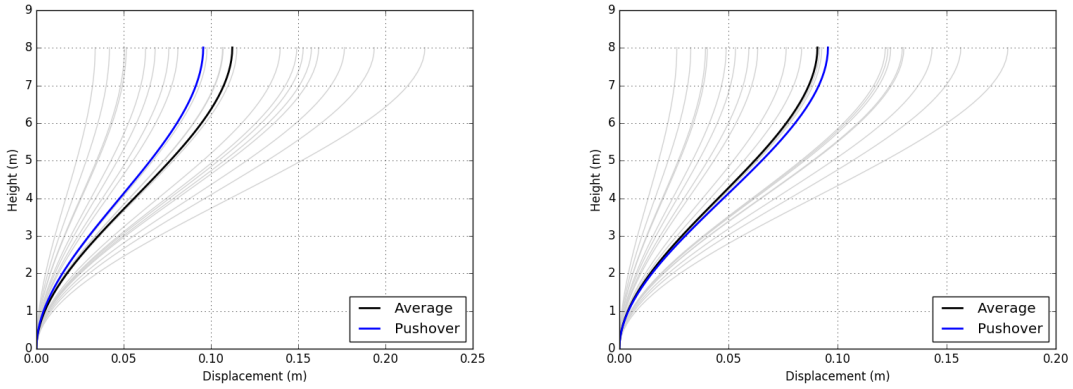

(a) (b)

Figure A.2: Comparison of results for DS2, scaling according to (a) the unsmoothed scaling method, and the (b) Cardone's scaling method.

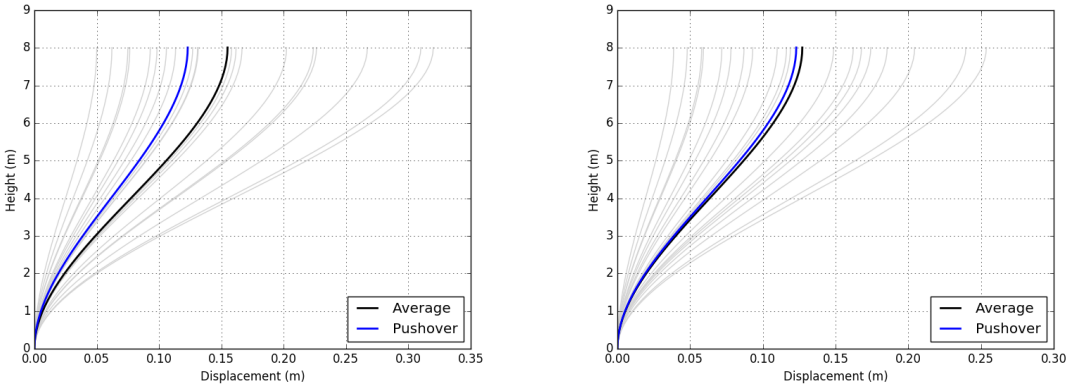

(a) (b)

Figure A.3: Comparison of results for DS3, scaling according to (a) the unsmoothed scaling method, and the (b) Cardone's scaling method.

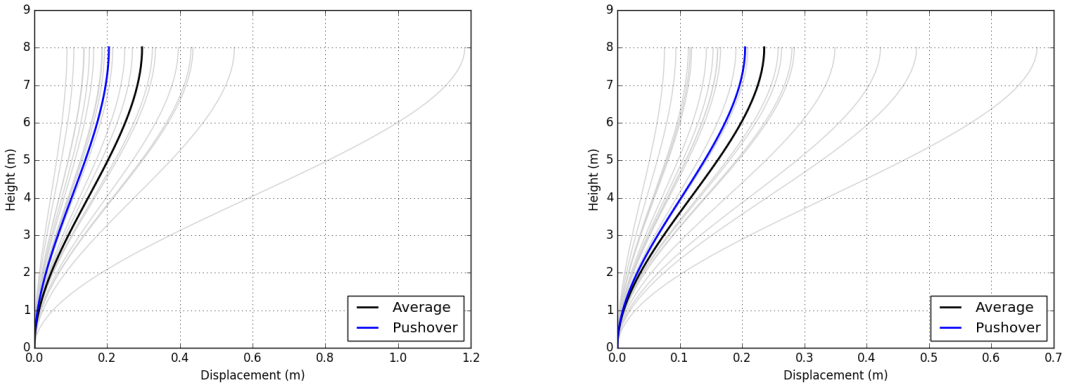

(a) (b)

Figure A.4: Comparison of results for DS4, scaling according to (a) the unsmoothed scaling method, and the (b) Cardone's scaling method.

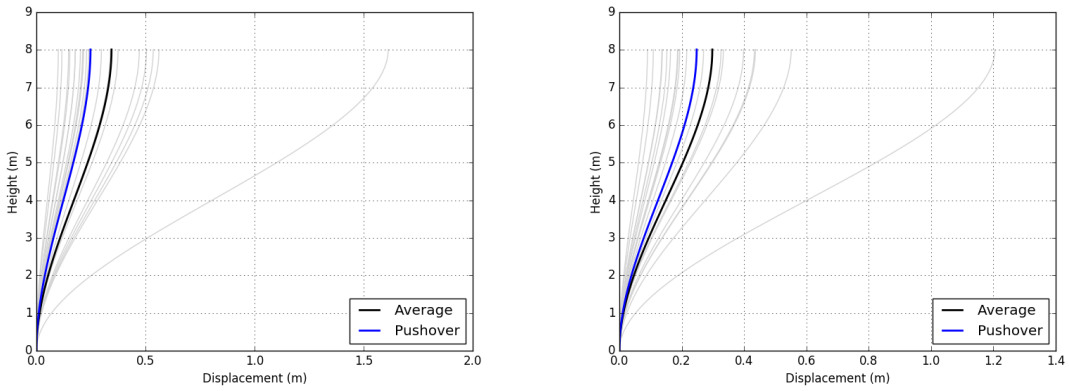

(a) (b)

Figure A.5: Comparison of results for DS5, scaling according to (a) the unsmoothed scaling method, and the (b) Cardone's scaling method.

A.2 Bridge 3

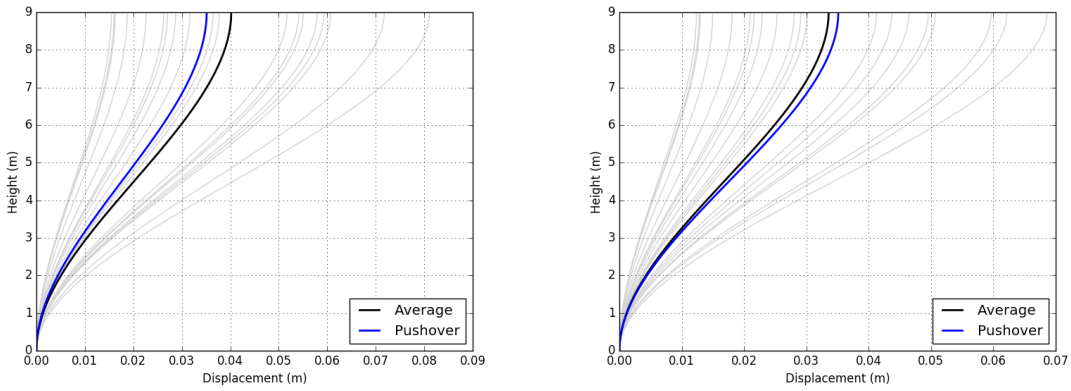

(a) (b)

Figure A.6: Comparison of results for DS1, scaling according to (a) the unsmoothed scaling method, and the (b) Cardone's scaling method.

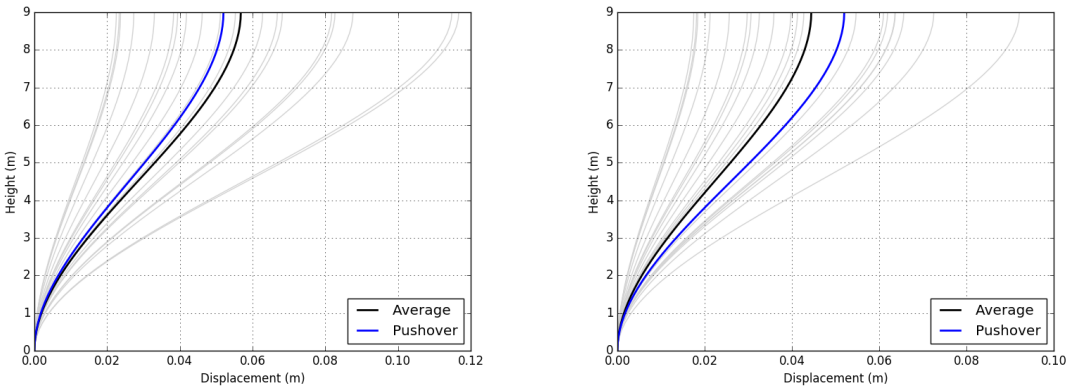

(a) (b)

Figure A.7: Comparison of results for DS2, scaling according to (a) the unsmoothed scaling method, and the (b) Cardone's scaling method.

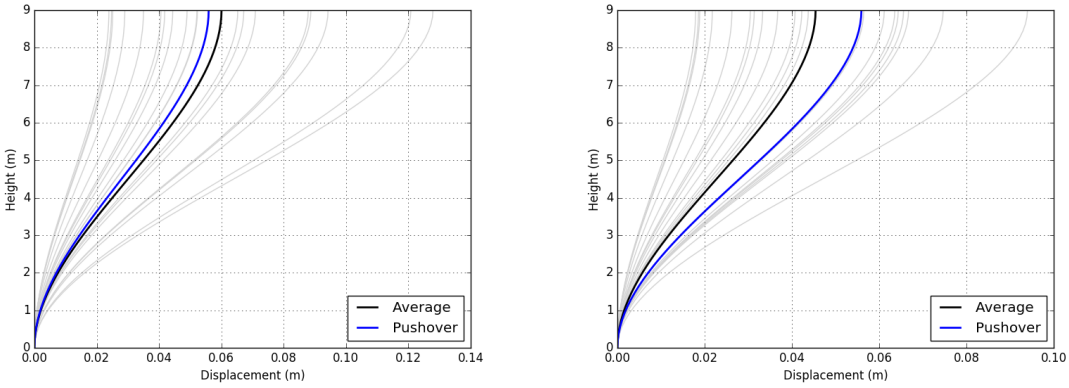

(a) (b)

Figure A.8: Comparison of results for DS3, scaling according to (a) the unsmoothed scaling method, and the (b) Cardone's scaling method.

A.3 Bridge 4

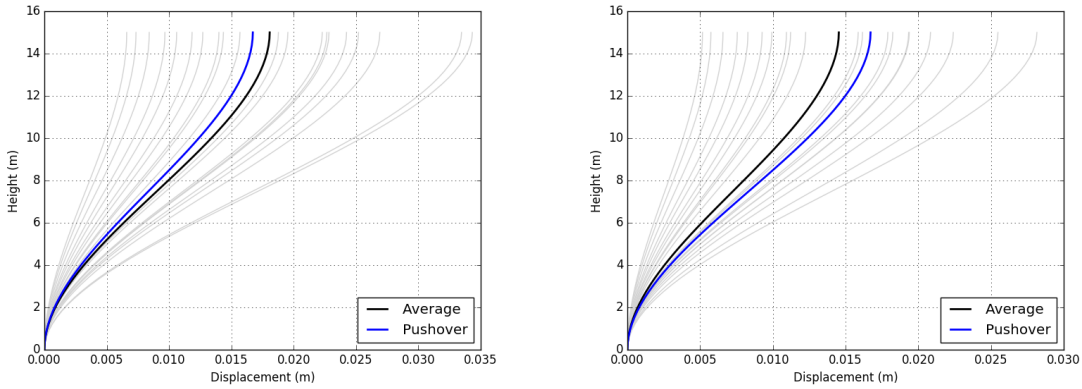

(a) (b)

Figure A.9: Comparison of results for DS1, scaling according to (a) the unsmoothed scaling method, and the (b) Cardone's scaling method.

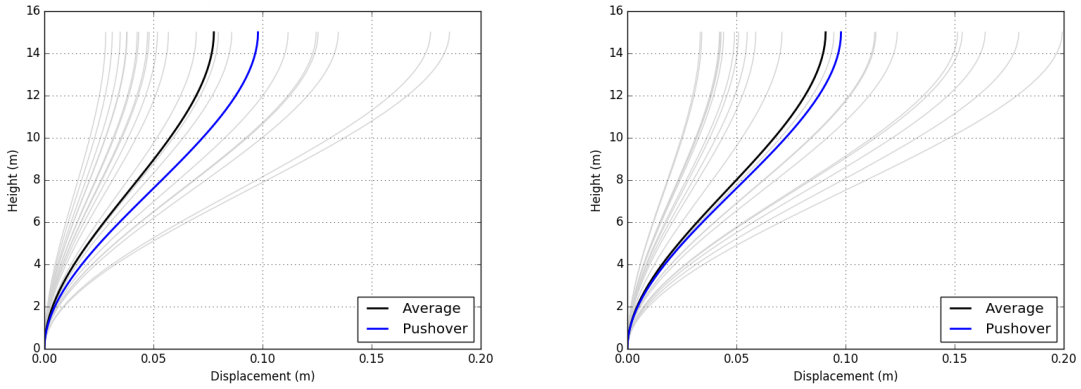

(a) (b)

Figure A.10: Comparison of results for DS2, scaling according to (a) the unsmoothed scaling method, and the (b) Cardone's scaling method.

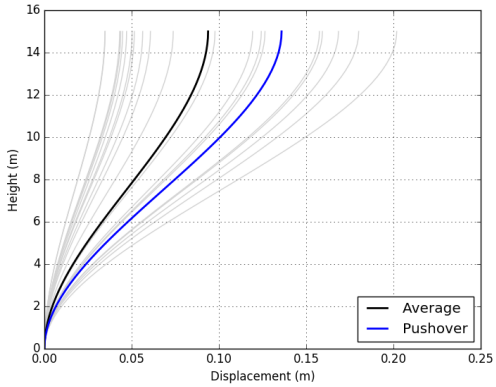

(a)

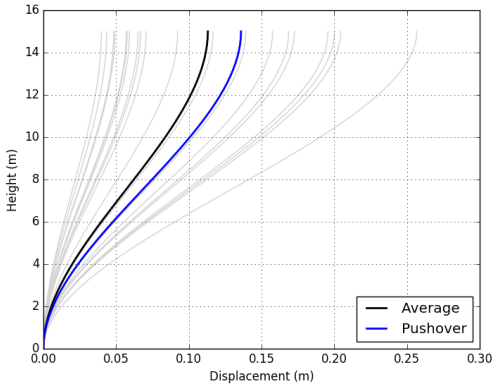

(b)

Figure A.11: Comparison of results for DS3, scaling according to (a) the unsmoothed scaling method, and the (b) Cardone's scaling method.

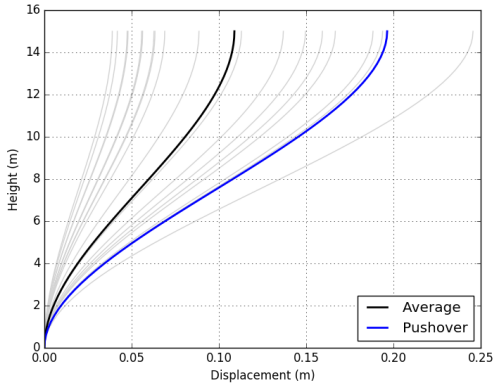

(a)

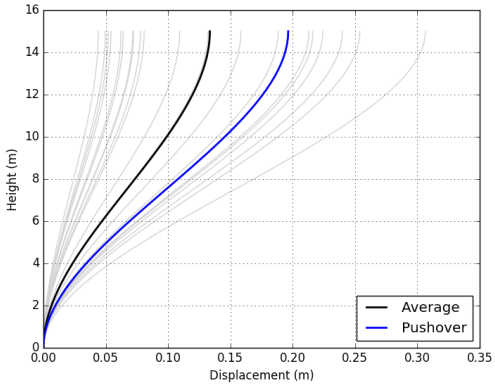

(b)

Figure A.12: Comparison of results for DS4, scaling according to (a) the unsmoothed scaling method, and the (b) Cardone's scaling method.

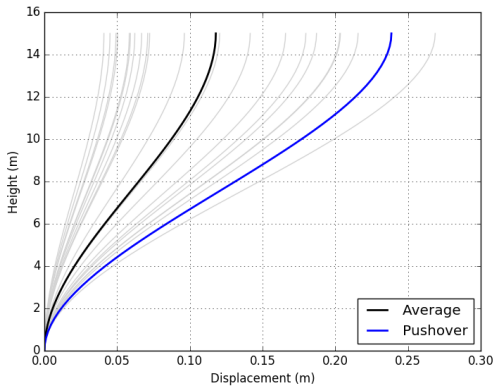

(a)

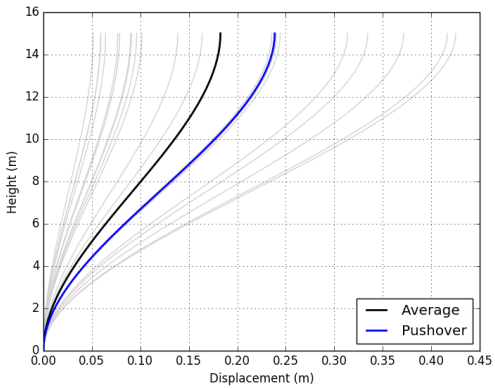

(b)

Figure A.13: Comparison of results for DS5, scaling according to (a) the unsmoothed scaling method, and the (b) Cardone's scaling method.

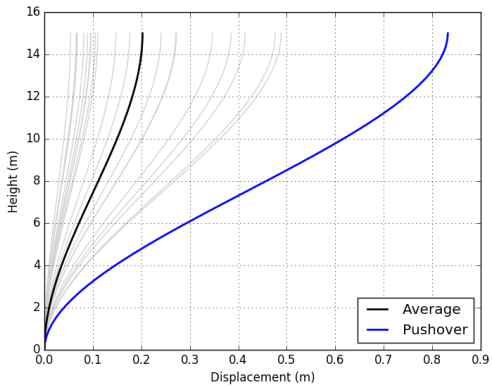

(a)

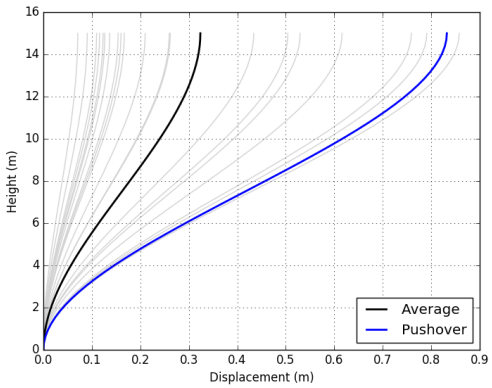

(b)

Figure A.14: Comparison of results for DS6, scaling according to (a) the unsmoothed scaling method, and the (b) Cardone's scaling method.

A.4 Bridge 5

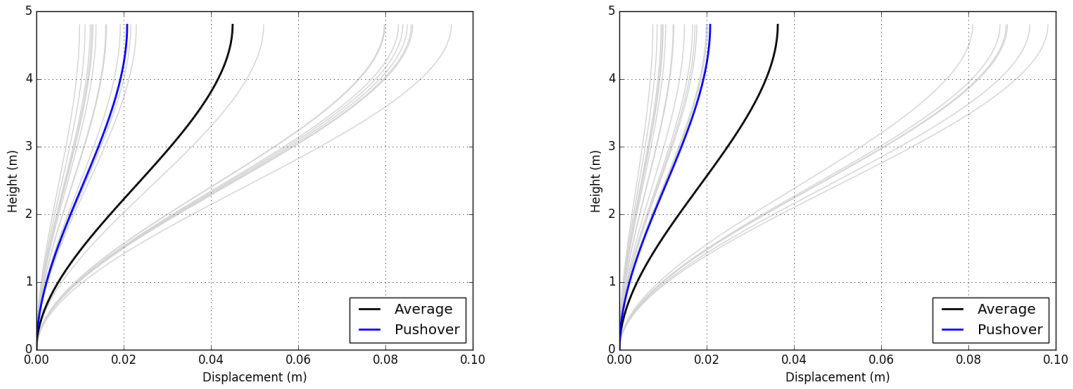

(a) (b)

Figure A.15: Comparison of results for DS1, scaling according to (a) the unsmoothed scaling method, and the (b) Cardone's scaling method.

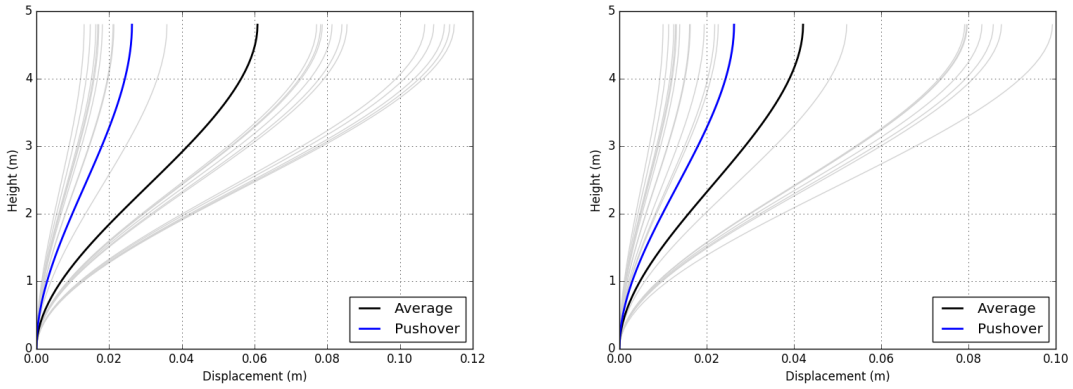

(a) (b)

Figure A.16: Comparison of results for DS2, scaling according to (a) the unsmoothed scaling method, and the (b) Cardone's scaling method.

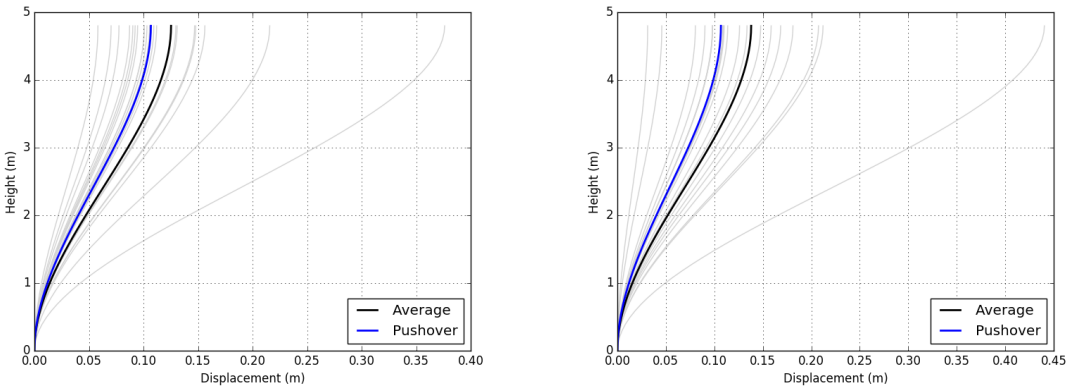

(a) (b)

Figure A.17: Comparison of results for DS3, scaling according to (a) the unsmoothed scaling method, and the (b) Cardone's scaling method.

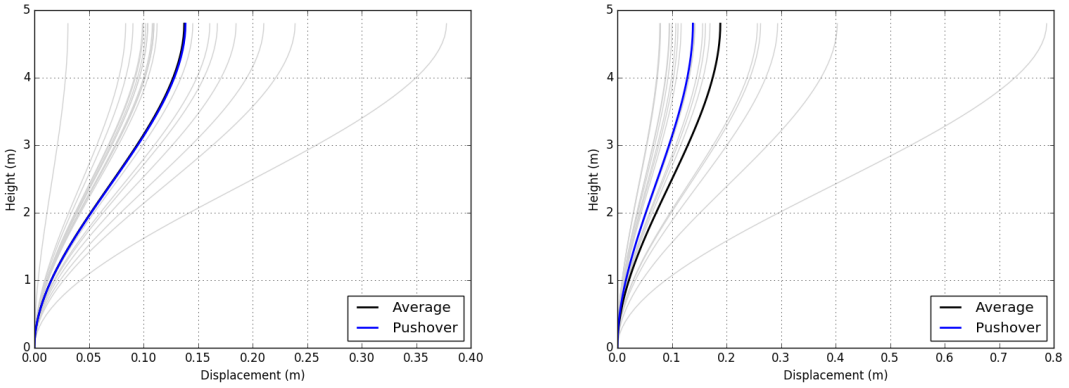

(a) (b)

Figure A.18: Comparison of results for DS4, scaling according to (a) the unsmoothed scaling method, and the (b) Cardone's scaling method.

A.5 Bridge 6

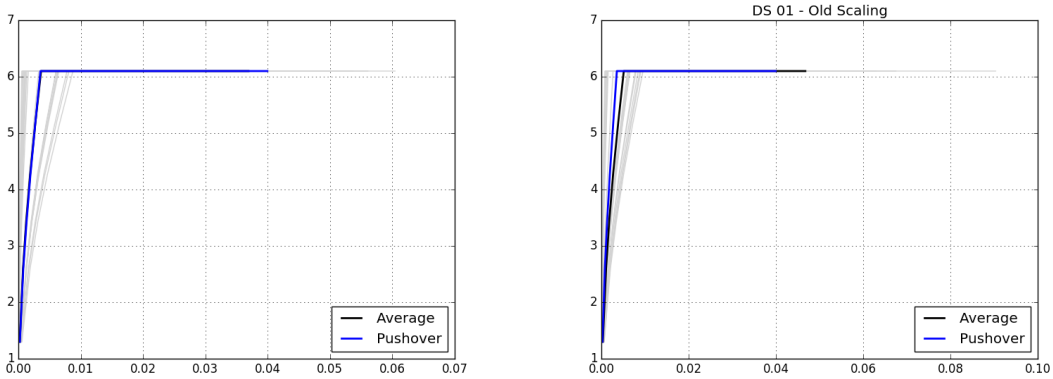

(a) (b)

Figure A.19: Comparison of results for DS1, scaling according to (a) the unsmoothed scaling method, and the (b) Cardone's scaling method.

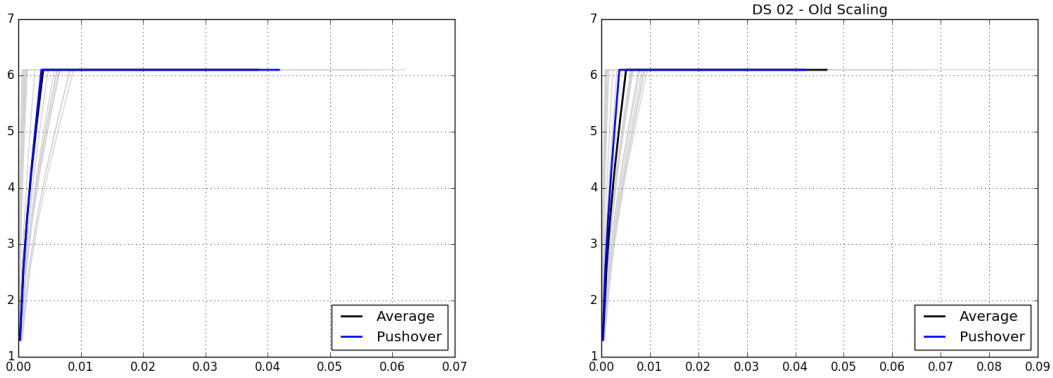

(a) (b)

Figure A.20: Comparison of results for DS2, scaling according to (a) the unsmoothed scaling method, and the (b) Cardone's scaling method.

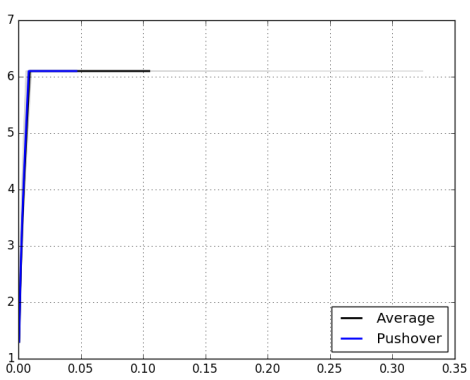

(a)

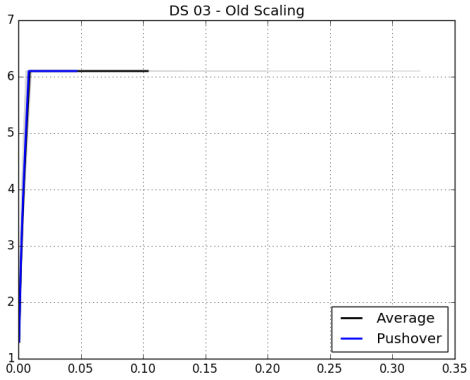

(b)

Figure A.21: Comparison of results for DS3, scaling according to (a) the unsmoothed scaling method, and the (b) Cardone's scaling method.

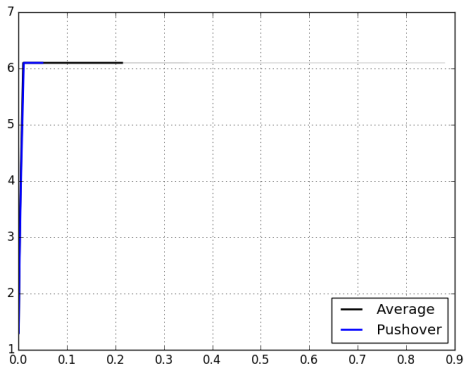

(a)

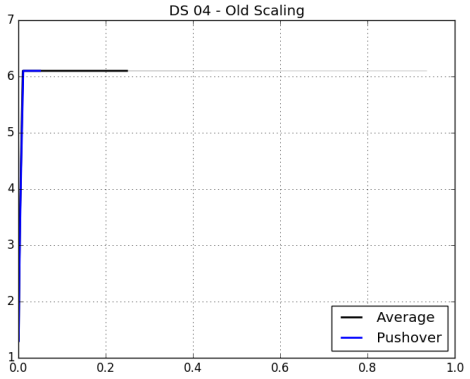

(b)

Figure A.22: Comparison of results for DS4, scaling according to (a) the unsmoothed scaling method, and the (b) Cardone's scaling method.

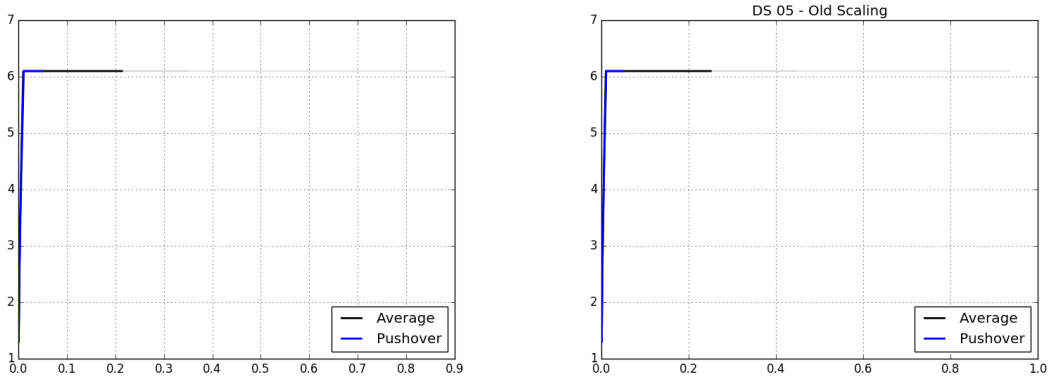

(a) (b)

Figure A.23: Comparison of results for DS5, scaling according to (a) the unsmoothed scaling method, and the (b) Cardone's scaling method.

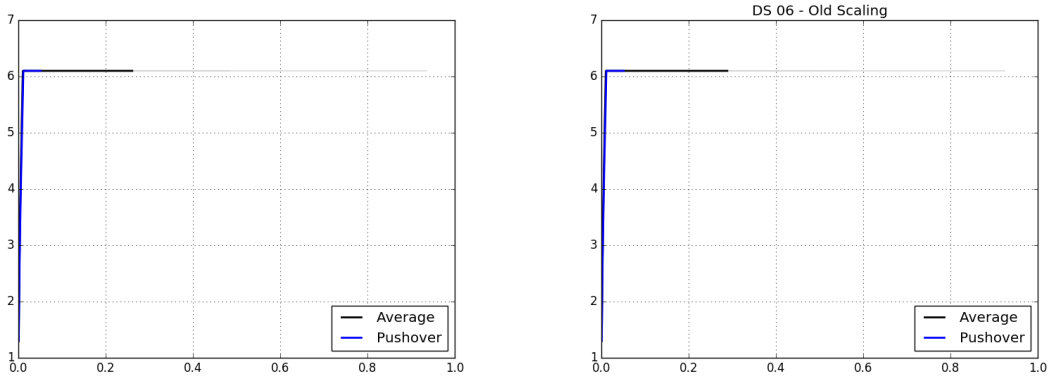

(a) (b)

Figure A.24: Comparison of results for DS6, scaling according to (a) the unsmoothed scaling method, and the (b) Cardone's scaling method.

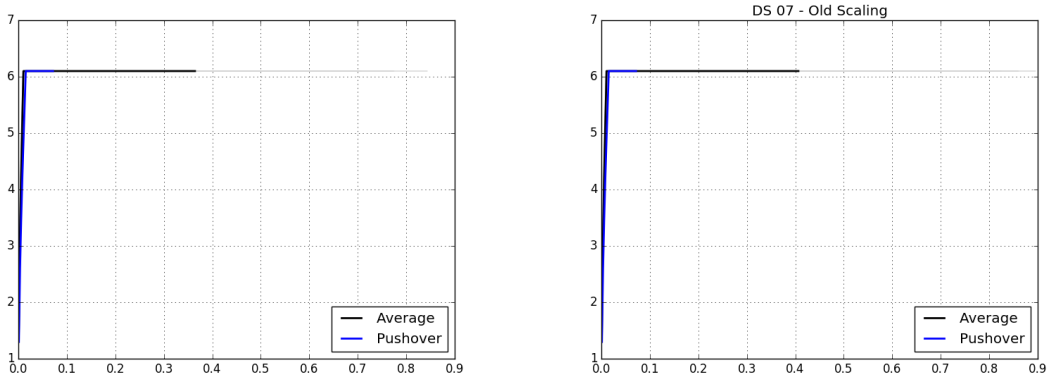

(a) (b)

Figure A.25: Comparison of results for DS7, scaling according to (a) the unsmoothed scaling method, and the (b) Cardone's scaling method.

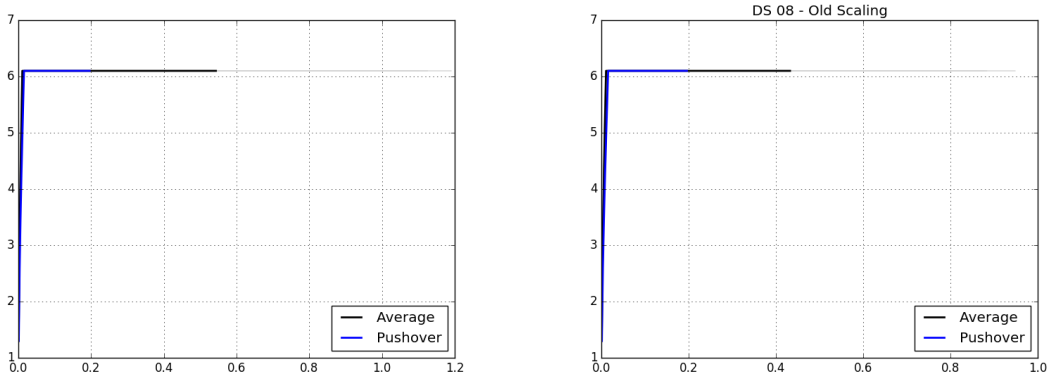

(a) (b)

Figure A.26: Comparison of results for DS6, scaling according to (a) the unsmoothed scaling method, and the (b) Cardone's scaling method.

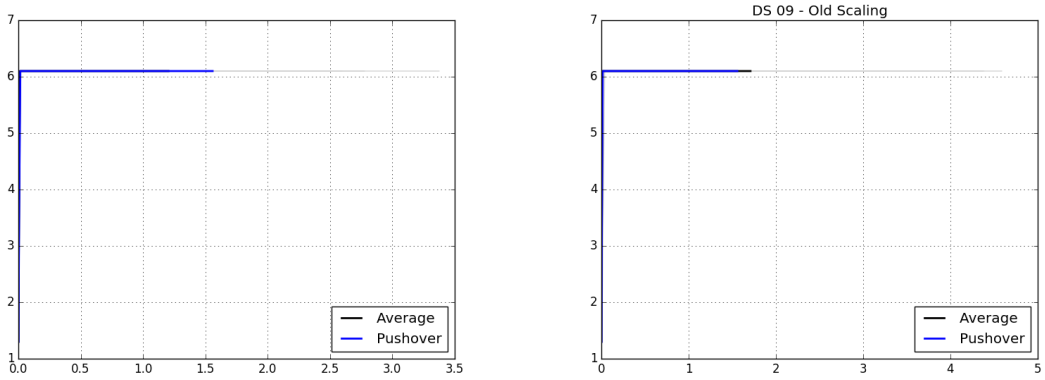

(a) (b)

Figure A.27: Comparison of results for DS6, scaling according to (a) the unsmoothed scaling method, and the (b) Cardone's scaling method.

A.6 Bridge 7

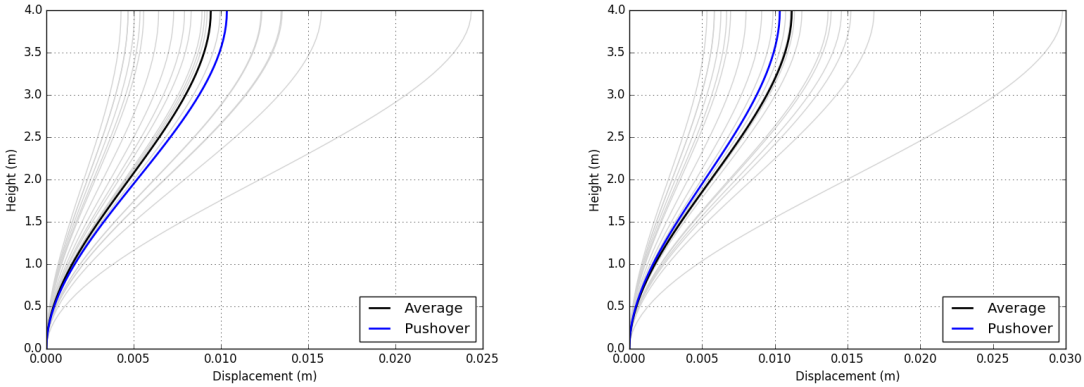

(a) (b)

Figure A.28: Comparison of results for DS1, scaling according to (a) the unsmoothed scaling method, and the (b) Cardone's scaling method.

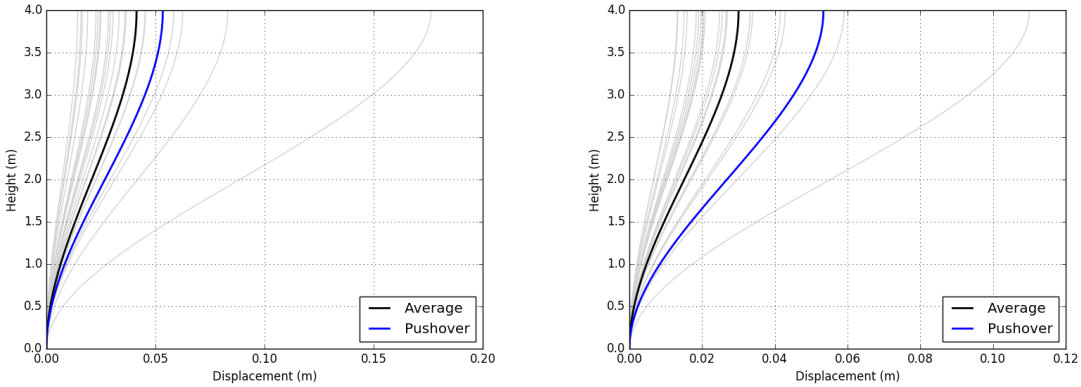

(a) (b)

Figure A.29: Comparison of results for DS2, scaling according to (a) the unsmoothed scaling method, and the (b) Cardone's scaling method.

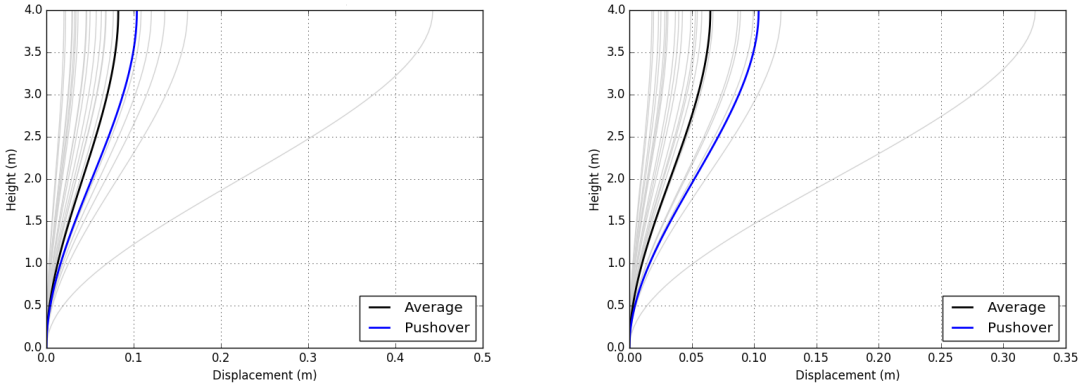

(a) (b)

Figure A.30: Comparison of results for DS3, scaling according to (a) the unsmoothed scaling method, and the (b) Cardone's scaling method.